Queen Mary
University of London

Rate-dependent Mechanical Properties of the Interfaces in Biological Composites

THESIS SUBMITTED TO THE UNIVERSITY OF LONDON

FOR THE DEGREE OF DOCTOR OF PHILOSOPHY

NOVEMBER 2015

BY

YIRAN AN

SCHOOL OF ENGINEERING AND MATERIALS SCIENCE

QUEN MARY, UNIVERSITY OF LONDON

MILE END ROAD, LONDON, E1 4NS

Declaration

I declare that the work performed is entirely by myself during the course of my PhD studies at the Queen Mary, University of London and has not been submitted for a degree at this or any other university.

Yiran An

Abstract

Biology produces a range of composite structures that evolve to resist a wide range of loading conditions from their environments. The mechanical function of these biological composites is expected to be governed by the properties of the interfaces between distinct hard and soft constituents at different length scales. However, difficulties exist in applying composite theories to biological structures since the interfaces present between the nanoscale biological constituents are typically below standard measurement length scales. Hierarchical biological composites found in nacre and arthropod exoskeleton are distinct examples of structures potentially optimized to resist dynamic loading conditions. Understanding the deformation and failure of such biological composites thus require evaluations beyond quasi-static conditions. Knowing the dynamic mechanical properties of the biological interfaces at small scales would make a better understanding how nature designs different biological structures to serve their specific mechanical functions and potentially provide better guidance for synthesizing bio-inspired composites.

Therefore, the aim of this PhD project is to examine the rate-dependent mechanical properties of the interfaces in different biological composites using a novel mechanical testing technique incorporating scanning electron microscopy (SEM),

focused ion beam (FIB) microscopy and atomic force microscopy (AFM) to understand their interfacial mechanical behaviour under different loading conditions and establish a relationship between their interfacial mechanics and their physiological loading conditions.

As most biological composites are physiologically in hydrated condition, it is therefore critical to justify the applied experimental methodology capable of mechanically testing biological samples in hydrated condition effectively. Elastic modulus of nacre fabricated using FIB at the microscale were shown to be similar for both dry and hydrated samples under SEM vacuum and ambient air conditions, validating our methodology of mechanically testing hydrated biological samples under SEM vacuum condition at the sub-microscale. Nacre was then studied by performing the AFM nanoscale interfacial shear test under loading rates with the range of two orders of magnitude and a shear strength decrease of around 10% was found. General interfacial mechanical behaviour within biological composites was further explored by comparing interfacial mechanical behaviour from nacre and arthropod exoskeleton to the interfacial shear behaviour of the NCP-MCF interface in antler bone. All the three biological composites exhibited a weakened interface with increasing loading rates, but the biological interface with less confinement showed a shear strength more sensitive to varying loading rates and appeared to adapt to less dynamic physiological loading conditions. Finally, this work evaluated mechanically graded tendon-to-bone interfaces, highlighting the flexibility of the experimental approach used. Microscale beams of tendon-to-bone attachment fabricated using FIB were successfully tensile tested using in situ AFM. An analytical

model based on a simple rule of mixtures was used to predict the elastic moduli of the tendon-to-bone beams by consideration the spatial compositional variations within the larger interfacial regions, again providing a more complex-structure function relationship in a biological composite. Therefore, this PhD work highlights the use of mechanical testing using AFM and SEM to investigate the rate-dependent mechanical behaviour of small scale interfaces in a variety of structural biological composites.

Acknowledgements

This thesis is a complete review of my four-year PhD study, which has been supported and contributed by many people. First and foremost, I would like to express my sincere gratitude to my supervisor Professor Asa Barber for his continuous support, guidance and encouragement throughout my PhD study but also daily jokes, smiles on his face, life suggestions and everything. I feel so lucky to be his student and would be grateful all my life. I would also like to thank my second supervisor Dr. Himadri Gupta for his inspiring suggestions and ideas. His enthusiasm at research and science set a great example for me in my future life.

All the other researchers and technicians who supported me are gratefully acknowledged. Particularly, I would like to thank Dr. Zofia Luklinska and Dr. Russell Bailey at the NanoVision Centre for the experiment assistance in electron microscopy facilities. I would also like to thank Dr. Ettore Barbieli and Dr. Simone Falco for their great help in modelling analysis. Special thanks are also given to Dr. Alix Deymier-Black for her great efforts in tendon-to-bone sample preparation.

The work in this PhD thesis is also supported and encouraged by our group members. Special thanks to Dr. Congwei Wang for his help in training FIB fabrication and

Attocube AFM system and Dr. Ines Jimenez-Palomar for her help in AFM data analysis. I would also like to thank Dr. Russell Bailey for his valuable suggestions and help on daily experiments. Thanks are given to the other current and former members of Barber‘ research group: Dr. Urszula Stachewicz, Dr. Lun Lv, Dr. Fei Hang, Bea Cortés Ballesteros, Filipe Almeida, Neelam Siyab, Alexander Kao, Hao Zhang, Fengfeng Zhang, Wenjun Sun and Gannian Zhang.

Outside of the research, I am very grateful for the help and encouragement of my friends in my difficult times and also all the happy hours we have spent together: Dr. Jian Yao, Dr. Xin Bai, Kan Chen, Xingyu Han, Zheng Li, Tianyi Zhang, Wei He, Yang Wang, Jingwen Bai, Menglong Huang, William Megone, Hong Liu and Nan Wang.

Special acknowledgement to my dearest parents and my dearest love Jingyi to whom this work is dedicated. I cannot achieve anything without all your support and love.

Thanks,

Yiran

Table of Contents

List of Figures

List of Tables

List of Constants

ρ	density
E	Young's modulus
σ	tensile stress
K_c	fracture toughness
c	volume fraction
ν	Poisson's ratio
ε	tensile strain
G	shear modulus
K	bulk modulus
Δ	volume change
a	flaw size
$\Delta G^{\#}$	free energy
S	entropy
t	time
W	number of possible configurations
k	Boltzmann constant
Φ	volume concentration
γ	surface energy
α	proportionality constant
h	thickness
k	spring constant
w	width
L	length
Q	quality factor of the cantilever

f_0	resonance frequency of the cantilever
Γ	imaginary component of the hydrodynamic function
R_e	Reynolds number
η_f	viscosity of the fluid
A_{white}	white noise fit baseline
A_0	zero frequency amplitude
F	force
d	deflection of the AFM cantilever
A_1 and A_2	wave amplitudes
I	laser intensity
A	cross-sectional area
X	retraction distance of piezo scanner
ΔL	elongation of the sample
λ	wavelength of the laser
D	initial cantilever-fibre optic distance
δ	deflection of the free end of the beam
I	moment of inertia
γ	shear strain
S	distance between the point of applied force and the shear plane
τ	shear stress
A_D	damage area
J_0	interfacial toughness
W	toughness
D	fibril diameter
l_e	length of fibril embedded within the bone
γ	interfacial fracture energy
V_M, V_U, and V_G	fractions of mineralized, unmineralized, and graded tissue
v_1 and v_2	horizontal and vertical displacement
Δ	total displacement of the beam

Publications

1. **Yiran An**, Simone Falco, Nicola M. Pugno, Himadri S. Gupta, Ettore Barbieri and Asa H. Barber (2015). *On the nanoscale origin of rate-dependent toughness in nacre*. Submitted.
2. **Yiran An**, Fei Hang, Himadri S. Gupta and Asa H. Barber. *Rate-dependent interfacial nanomechanical trends in biological composites*. In preparation.
3. **Yiran An**, Alix C Deymier-Black, Andrea G. Schwartz, Guy M. Genin, Stavros Thomopoulos and Asa H. Barber. *Micromechanical tensile properties of tendon-to-bone attachment*. In preparation.
4. **Yiran An** and Asa H. Barber. *Influence of SEM vacuum on the mechanical properties of nacre*. In preparation.
5. **Yiran An** and Asa H. Barber (2013). *Rate-dependent behaviour of mineral-protein nano-Interfaces in nacre*. ICMOBT (5th International Conference on Mechanics of Biomaterials and Tissues). Oral presentation.
6. **Yiran An** and Asa H. Barber (2015). *Rate-dependent nanomechanical properties of tough biological composite structures*. ESMC (9th European Solid Mechanics Conference). Oral presentation.

Chapter 1 - Introduction

1.1 Background

Composites are a common class of materials where two or more distinct constituent phases are identifiable within the material structure (1). Composites are often used in structural applications and have synergistic improvements over their separate constituents, as well as potential weight savings. These structural composites are found widely in engineered structures such as aerospace and automotive industries due to their high specific mechanical properties. However, a considerable range of materials found in structural applications within biological organisms can also be clearly identified as having composite structures, most notably in mineralized tissues.

The mechanical properties required from a composite ranges from strength and stiffness to toughness. It is common that composites achieve far better mechanical properties over their individual constituents. Therefore, understanding the mechanical behaviour of the composite constituents and more importantly, the interaction between the composite constituents is therefore critical in evaluating composite structures or providing design improvements. To this end, composite

constituents are widely defined as bi-components in terms of the properties of the reinforcing phase and the second binding phase, known as the matrix. Due to the extensive existence between composite constituents, the interfaces in composites have been widely regarded as being critical in defining overall mechanical response of composites. Generations of composite researchers have investigated interfacial behaviour and attempted modifications in order to optimize the interface according to the desired function. Mechanically, two interfacial conditions have been noted: 1) weak adhesion between reinforcement and binding matrix promotes reinforcement pullout for increased composite toughness whereas 2) strong interfacial adhesion allows efficient stress transfer from matrix to reinforcement for strong composites (1).

The state-of-the-art in high performance composites has extended these design strategies to their potential pinnacle through the use of reinforcements such as nanotubes (2) and nanoclays (3). For example, significant activity has focused on high strength composites (2) produced from carbon nanotubes modified to chemically bond with the polymer matrix, following classic work on silane treated glass- or oxidized graphite- fibres bonding to polymer matrices (1). Biomimetic nanocomposites, based on designs found in nature, have recently received much attention as tough materials that evolve a large fracture area upon failure (3-5). However, the majority of these studies on interfacial mechanical optimization are critically based on evaluation and design for quasi-static loading events. A significant number of biological composites found in nature are subjected to a wide range of loading conditions for which quasi-static test is simply not suitable in recreating the

service-life loading conditions. Such loading conditions include impact of high loads and rates, smaller repetitive dynamic loading in vibration absorption, damping and fatigue. The rate-dependence of the mechanics of these biological materials is expected to be localized in the flexible molecules in the narrow interfaces between reinforcements, which are themselves rate dependent mechanically. A number of questions are therefore raised when considering biological composite structures. What are the structural mechanisms in the confined interfacial polymers activated in response to dynamic loading conditions? How do these mechanisms change as the interfacial structure or loading rate varies?

To address these questions, it has been found by composites researchers that the consideration of design strategies used by natural biological composites is persuasive. Numerous structural biological composites are mechanically robust across a wide range of loading rates. Examples include the slow actuation of plant organs through water movement, periodic fatigue-type loading in tendon, the fast loading rates found in the impact of deer antler and the shell breaking appendages of mantis shrimp (6-10). Such biological composite systems exhibit common structural features at the nanoscale including a stiff majority reinforcement or scaffold surrounded by an amorphous interfacial region with a relatively small volume. Small changes to these interfacial regions are expected to have a significant effect on dynamic mechanical response of the material. The examination of the rate-dependent interfacial deformation mechanisms at the nanoscale requires an experimental technique that both records the mechanical response from a rapidly deforming material and acquires structural information at small length scales

during this deformation. Focused ion beam (FIB) technique has been shown to have the ability to fabricate biological samples into discrete volumes of small length scales (11) while atomic force microscopy (AFM) has been widely employed for mechanical testing at small length scales for biological composites (12, 13). In this PhD project, a novel custom built AFM combining scanning electron microscopy (SEM) and FIB is developed for a wide range of nanomechanical testing, as shown in Figure 1.1.

Figure 1.1 Photographs highlighting the experimental setup used to combine SEM, FIB and AFM techniques within a single instrument. The left image shows a standard SEM-FIB dual-beam system (Quanta 3D FEG, FEI, USA/EU) whereas the right image indicates a custom built AFM that sits inside the SEM vacuum chamber and therefore allows in situ mechanical testing of small volumes of a wide range of biological samples.

1.2 Project Aims

The main aim of this PhD project is to develop a novel mechanical testing methodology to investigate dynamic interfacial mechanical properties of different biological composites at small length scale. In order to achieve the overall aims, the objectives are outlined as follows:

1. Develop a mechanical testing methodology suitable for evaluation of biological composites at small length scales. A custom built AFM integrated in SEM will provide both force spectroscopy for the measurement of mechanical properties as well as in situ observation of the failure behaviour using SEM imaging.

2. Isolate discrete volumes suitable for AFM nanomechanical testing from the parent biological samples using FIB. Specially, the nanoscale interfaces in nacre and arthropod exoskeleton will be isolated from the bulk and directly tested mechanically.

3. Validate this mechanical testing methodology of examining hydrated biological samples under SEM vacuum environment.

4. Evaluate the rate-dependent mechanical behaviour of the discrete biological interfaces in nacre and arthropod exoskeleton and understand the role of the interfacial mechanics in controlling the overall mechanical properties.

5. Extend mechanical evaluation of interfaces by examining a graded interface structure as found in tendon-to-bone attachment.

1.3 Thesis Outline

The thesis is presented in eight chapters. A brief synopsis of each chapter is given as follows:

The first chapter briefly introduces the background of this PhD project and the significance this work might bring to the composite material society. Then the main aim of this PhD project is illustrated followed by detailed objectives to achieve. After that, a thesis outline is given to present the structure of this PhD thesis.

Chapter 2 reviews the basic background and knowledge related to the mechanical, structural, and formational properties of biological composites. Existing works are further reviewed to present a broad picture of the hierarchical structures and mechanical properties of three well-studied biological composites, including nacre, arthropod exoskeleton and tendon-to-bone attachment. These biological composites form the main applications of small scale mechanical testing of interfaces in this PhD thesis.

To resolve the issue of mechanically testing biological composites at small length scales, a novel in situ nanomechanical testing methodology combining SEM, FIB and AFM is developed and described in detail in Chapter 3. FIB is used to fabricate

biological samples into dimensions suitable for nanomechanical testing, while mechanical properties are obtained from the custom built AFM system combined within the SEM-FIB dual-beam system.

An obvious potential disadvantage of this combined mechanical testing technique is the exposure of biological samples to the SEM vacuum conditions, which might dry biological samples and affect their mechanical performance. Therefore in Chapter 4, elastic modulus of FIB-fabricated biological samples is mechanical tested and shown similar for both dry and hydrated samples under SEM vacuum and ambient air conditions, validating our methodology of mechanically test hydrated biological samples under SEM vacuum condition at the sub-microscale.

After validation of the experimental methodology, nacre from abalone shell is studied by performing the nanoscale interfacial shear test under a range of loading rates in Chapter 5. Failure of the interface between nacre mineral tablets indicates a reduction in interfacial strength but an enhanced overall toughness with increasing loading rate, with two interfacial mechanisms proposed to explain this interfacial weakening behaviour under high loading conditions.

In Chapter 6, the interface between arthropod exoskeleton layers is studied following similar experimental protocol in Chapter 5 and similar trend of the rate-dependent interfacial behaviour is observed. Further investigations are performed to study the relationship between the rate-dependent mechanical behaviour of three biological composites (nacre, arthropod exoskeleton and antler bone) and their

physiological loading conditions. A mechanism is proposed based on these observations and simulations that considers the requirement of enhancing damage volume while minimizing the work of interfacial failure to maximize structural toughness under dynamic loading conditions.

Chapter 7 extends this nanomechanical testing technique to larger length scale graded tendon-to-bone interfaces highlighting the flexibility of the experimental approach. These design strategies are potentially important in future applications when incorporated into engineered composites that operate under rapid loading conditions.

Finally, the eighth chapter summarizes the main contributions of thesis. Additional studies beyond the thesis and future work are also examined.

Chapter 2 - Literature Review

2.1 Introduction

This chapter first reviews general terms of composite materials and the importance of various interfaces in composites at different length scales. Structural biological composites have a range of hierarchical architectures formed from complex biological processes that are notably more complex than typical engineering composites. The formation of structural biological composites is therefore reviewed subsequently and applied to describe the resultant structures of the three main subjects studied in this thesis: nacre of abalone shell, exoskeleton of mantis shrimp and the tendon-to-bone attachment from the humeral head of a mouse. Afterwards, existing literatures related to structures and mechanical properties of these structural biological composites are discussed in detail respectively. The literature review is of particular importance for justifying the experimental work of exploring mechanical properties of these structural biological composites at the sub-micron length scale.

2.2 Composites

Composites are materials made from two or more constituent materials with significantly different physical or chemical properties, that when combined, produce a material with characteristics that differ from the individual components. In many cases, a strong and stiff component is present, often in elongated anisotropic form, embedded in a softer constituent forming the matrix. Normally, composites show marked overall anisotropy; that is to say, their properties vary significantly when measured in different directions. This usually arises because the harder constituent is in fibrous form with the fibre axes preferentially aligned in particular directions. In addition, one or more of the constituents may exhibit inherent anisotropy as a result of their crystal structure.

In considering the formulation of a composite material for a particular type of application, it is important to consider the properties exhibited by the potential constituents. The properties of particular interest are the stiffness (Young's modulus), strength and toughness. Density is of great significance in many applications, since the mass of the component may be of critical importance. Representative property data are shown in Table 2.1 for various types of matrix and reinforcement, comparison with some typical engineering materials and composites. Inspection of Table 2.1 indicates that outstanding property combinations can be obtained from these composites. For example, wood has a relatively high specific

strength due to low density, whereas polymer matrix composites (PMCs) have a higher specific fracture toughness than most metals.

Table 2.1 Overview of different mechanical properties exhibited by different classes of materials (1).

Type of material (example)	Density ρ (g·cm^{-3})	Young's modulus E (GPa)	Strength σ (MPa)	Fracture toughness K_c (MPa √m)	Specific fracture toughness (N·m$^{4.5}$·g^{-1})
Thermosetting resin (epoxy)	1.25	3.5	50	0.5	0.4
Engineering thermoplastic (nylon)	1.1	2.5	80	4	3.63
Rubber (polyurethane)	1.2	0.01	20	0.1	0.083
Metal (mild steel)	7.8	208	400	140	17.95
Construction ceramic (concrete)	2.4	40	20	0.2	0.083
Engineering ceramic (alumina)	3.9	380	500	4	1.03
Wood (Load∥grain)	0.6	16	80	6	10
(spruce) (Load⊥ grain)	0.6	1	2	0.5	0.83
General PMC (in-plane) (chopped strand mat)	1.8	20	300	40	22.22
Adv. PMC (load∥fibres)	1.6	200	1500	40	25
(APC-2) (Load⊥fibres)	1.6	3	50	5	3.13
MMC (Al-20%SiC)	2.8	90	500	15	5.36

Central to an understanding of the mechanical behaviour of a composite is the concept of load sharing between the matrix and the reinforcing phase. The stress may vary sharply from point to point (particularly with short fibres or particles as reinforcement), but the proportion of the external load borne by each of the individual constituents can be gauged by volume-averaging the load within them. Of course, at equilibrium, the external load must equal the sum of the volume-averaged loads borne by the constituents (for example the matrix and the fibre). This gives rise to the condition

$$c_f \sigma_m + (1 - c_f)\sigma_f = \sigma_A \qquad \text{Equation 2.1}$$

governing the volume-averaged matrix and fibre stresses (σ_m, σ_f) in a composite under an external applied stress σ_A, containing a volume fraction c_f of reinforcement. Thus, for a simple two-constituent composite under a given applied load, a certain proportion of that load will be carried by the fibre and the remainder by the matrix. Provided the response of the composite remains elastic, this proportion of load carried by the reinforcement will be independent of the applied load. The mechanical behaviour of the composites depends on the volume fraction, shape and orientation of the reinforcement and on the elastic properties of both constituents. The reinforcement may be regarded as acting efficiently if it carries a relatively high proportion of the externally applied load. This can result in higher strength, as well as greater stiffness, because the reinforcement is usually stronger, as well as stiffer, than the matrix. Analysis of the load sharing which occurs in a composite is central to an understanding of the mechanical behaviour of composites.

Fibre architecture, describing the arrangement of commonly found reinforcements in composites, is an additional important parameter in defining the mechanical properties of composites. A number of fibre arrangements can be defined for the cylindrical geometries of fibres bound together in a surrounding matrix. For the simplest system of fibres aligned uniaxially in the composite, a lattice packing arrangement can be classified into two different types: hexagonal or square. Hexagonal packing is geometrically more efficient than square packing and, in theory, produces higher volume fractions of reinforcement in a composite. In practice, synthetic composites are rarely within a hexagonal or square packing organization throughout the composite but can occur over small, localized regions. However, fibres aligned parallel to each other form an important composite classification known as unidirectional lamina (1).

Fibres arranged in pre-determined lamina layers of stacked fibres may be continuous or short and can be aligned in one direction or randomly. In order to simplify the study of laminates, each lamina is regarded as homogenous, meaning that the fibre arrangement and volume fraction are uniform throughout the layer. For definition purposes a ply is a unidirectional lamina and laminate is a stack of lamina. Two commonly found stacking sequences are the cross-ply laminate and the angle-ply laminate. The cross-ply describes a laminate with alternating piles; each ply having fibres orientated 90° to each other. The second angle-ply describes a laminate stacking arrangement where each ply has fibres that orientated 60° of each other (1).

The axial elastic behaviour of a fibre reinforced composites can be simplified by treating the materials as two components bonded together, with thickness relative to the volume fraction of the matrix and fibre. The two slabs of material are constrained to have the same lengths parallel to the bonded interface and hence, if a stress is applied along the fibre alignment, both components exhibit the same strain along the loading direction. This configuration is called the 'equal strain' condition and valid for loading along the fibre axis providing there is no interfacial sliding between the fibre and matrix. Such a simplification allows the elastic modulus of the composite to be derived and can be summarized using the 'rule of mixtures' shown in Equation 2.2 where the stiffness of the composite is a volume mean between the moduli of the two components.

$$E = E_f c_f + E_m c_m \qquad \text{Equation 2.2}$$

Where E is the overall elastic modulus of the composite, E_f is the elastic modulus of the fibre, E_m is the elastic modulus of the matrix, c_f is the volume fraction of the fibres and c_m is the volume fraction of the matrix. The 'rule of mixtures' is considered to have a high degree of precision as long as the fibres are long enough for the 'equal strain' assumption to apply. The equal strain treatment is often described as the 'Voigt model' (1) as shown in Figure 2.1c. Even though the 'rule of mixtures' equation has been shown to work for many composites with continuous fibres, minor deviations due to stresses that arise when the Poisson's ratios of the two components are not equal are expected as will be explained later and shown in Figure 2.2.

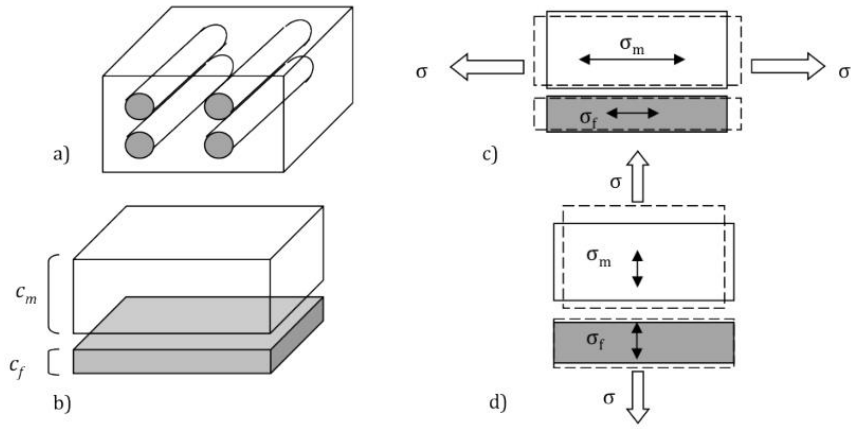

Figure 2.1 Schematic diagrams of (a) a fibre composite, (b) the 'slab model' used to represent composite materials in terms of volume fraction where c_f describes the volume fraction of the fibres and c_m describes the volume fraction of the matrix, (c) schematic of the Voigt model and (d) the Reuss model. The white arrows represent the stresses, σ, applied to the composite and the black arrows represent the stresses transferred to each of the components. The dotted lines represent the deformation experienced by each component (1).

The Voigt model is sufficient to describe a continuous reinforcement aligned in the direction of the applied load and can be considered as an upper limit when describing the elastic modulus of the composite material using Equation 2.2. Consequently, a lower limit on the elastic modulus of a composite can be determined from transverse stiffness. The simplest approach to define a lower limit for elastic behaviour is to represent the two components of reinforcement and matrix in the composite by the 'slab model' explained previously and shown in Figure 2.1a. A load applied orthogonally to the plane of the slabs will now produce variations in reinforcement and matrix phase strains, while each of these phases will be under an equal stress. This 'equal stress' model is often called a 'Reuss model' and can be used to calculate the elastic modulus of a composite using:

$$\frac{1}{E} = \frac{c_f}{E_f} + \frac{c_m}{E_m} \qquad \text{Equation 2.3}$$

The strain and stress produced when loading the fibres transversely is distributed inhomogenously within the matrix as opposed to when the fibres are loaded axially as shown in Figure 2.1d. The inhomogeneity causes sharp concentrations of stress in specific regions around the reinforcing fibres that could lead to interfacial debonding, matrix plastic deformation and micro-cracking. This non-uniform distribution of stress and strain in transverse loading means that the equal stress model is often inadequate, giving an underestimate of the elastic modulus and can be treated as a lower boundary condition when calculating elastic properties of composites.

The limits of the accuracy of the Voigt and Reuss models are due to the effect of the Poisson's ratio as the composite is loaded. The Poisson's ratio contraction effect is described by the matrix strain in the transverse direction caused by an axial stress. An aligned fibre composite has three different Poisson's ratios as shown in Figure 2.2. The first Poisson's ratio shown in Figure 2.2a describes how applying a load along the principal fibre axis leads to equal applied strains but to unequal Poisson strains. The second Poisson's ratio condition in Figure 2.2b describes how applying a load across of the fibres leads to unequal applied strains but equal Poisson strains and the third condition describes how applying a load transverse of the fibres as shown in Figure 2.2c leads to unequal applied strains and unequal Poisson strains.

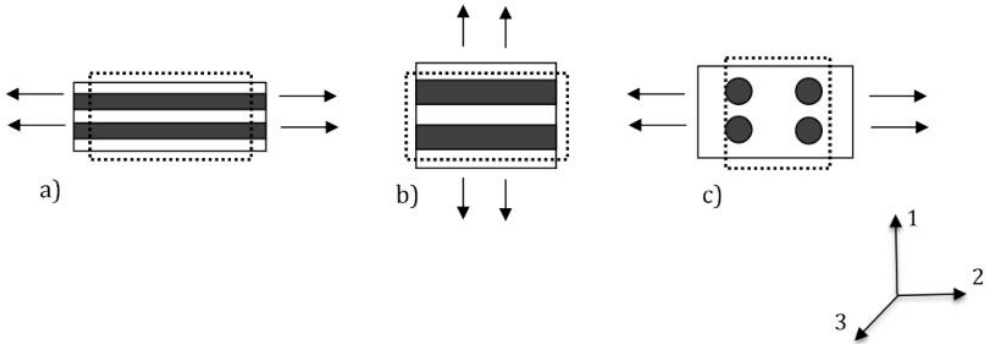

Figure 2.2 Schematic diagram, from (1), showing the effect of Poisson's ratio on fibre composites loaded in different directions: (a) a load along the principal fibre axis leads to equal to applied strains but unequal Poisson strains; (b) a load across of the fibres leads to unequal applied strains but equal Poisson strains; (c) a load transverse of the fibres leads to unequal applied strains and unequal Poisson strains. Dotted boxes represent state of composite before loading.

Poisson's ratio can be described therefore by the following equations:

$$\nu_{ij} = -\frac{\varepsilon_j}{\varepsilon_i} \qquad \text{Equation 2.4}$$

$$\frac{\nu_{12}}{E_1} = \frac{\nu_{21}}{E_2} \qquad \text{Equation 2.5}$$

$$G_{23} = \frac{E_2}{2(1+\nu_{23})} \qquad \text{Equation 2.6}$$

where ν_{ij} is the Poisson's ratio, where the *i*-direction is the direction at which the stress is applied and the *j*-direction is the direction of the deformation caused by the load in the *i*-direction; ε_i is the strain within the plane, ε_j is the strain normal to the plane, *E* is the Young's modus and *G* is the shear modulus.

Laminate composites describe a sequence of stacked and bound sheets of a composite material with different fibre arrangement within each lamina. Three types of composites are useful for applications where there is an equal distribution of stresses along all the directions. A laminate, as opposed to a random fibre mat, allows higher fibre volume fractions of fibres aligned in different and specific directions and is therefore useful for the effective transfer of loads in different directions (1). The composite mechanics theories of Voigt, Reuss and Halpin-Tsai are therefore also critical in describing the mechanical properties of composite structure laminates containing arranged fibrous reinforcements but can additionally predict mechanical behaviour in materials that approximate to laminate structures.

2.3 Structural Biological Composites

2.3.1 Overview

The study of biological materials has received increasing interest in recent years due to the often extraordinary mechanical properties and unusual structures these materials possess. A wide range of biological materials are complex composites with overall mechanical properties that are considered high performance despite using low performance constituents from which they are assembled. This limited mechanical behaviour of the constituents is a result of the ambient temperature, aqueous environment processing, as well as of the limited availability of elements (primarily C, N, Ca, H, O, Si and P) (10, 14). Biological organisms produce composites that are organized in terms of composition and structure, containing both inorganic

and organic components in complex structures. These components are hierarchically organized from the molecular to the macro (structural) level. The structural biological composites, which have risen from hundreds of million years of evolution, have attracted scientists to study their structure-property relationships for decades and stimulated the development of bio-inspired synthetic composites.

The study of structural biological materials such as seashells, antler, teeth and bones have yielded fascinating insight into how these inorganic/organic materials adjust their microstructure and growth conditions to provide superior structural properties. Mechanical property maps, more commonly known as Ashby maps, have become a convenient manner of concentrating a large amount of information into one simple diagram (15, 16). Two maps are presented in Figure 2.3 and present the Young's modulus and strength as a function of density. Several striking and defining features are noted:

- A wide range in Young's modulus from 0.01 to 100 GPa, indicating a stiffness diversity of four orders of magnitude, is utilized in the natural world.
- The range of toughness is almost as broad as the Young's modulus, varying over five orders of magnitude: 0.001 - 100 $kJ \cdot m^2$.

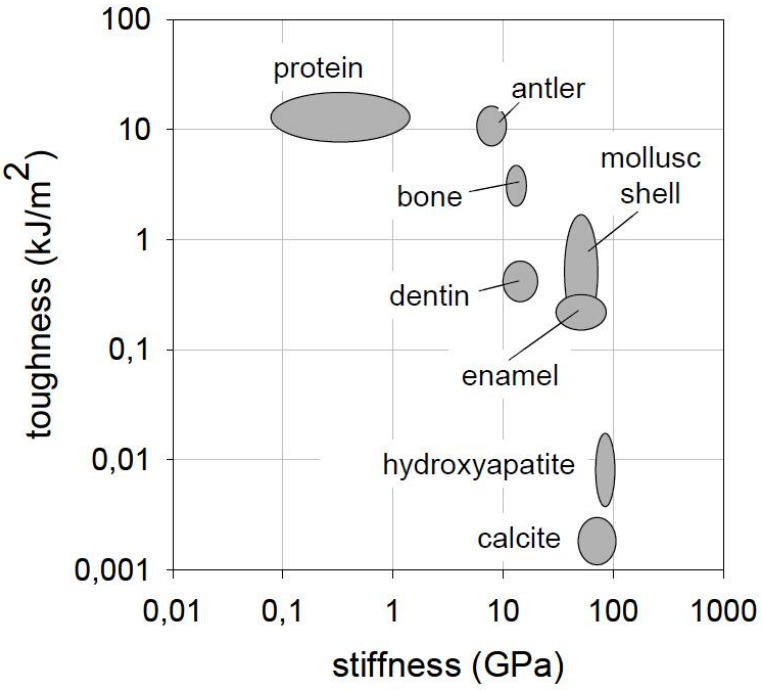

Figure 2.3 Ashby plots for biological materials showing toughness and modulus (16).

These biological composites have an integrated, hierarchical structure with an increasing complexity of the macro constituents as the dimension becomes smaller. The macroscale shape has been optimized for external influences such as protection and fighting and the nanoscale displays an intricate interaction between the mineral and organic components (10, 17). This interaction, which has components of strong chemical and mechanical adherence, is maintained throughout various length scales. It has been shown that the length scale of the component is important for the optimized mechanical performance (18, 19). Using the Griffith criterion for brittle fracture, the stress (σ) required to activate a flaw of size $2a$ is:

$$\sigma = \frac{K_c}{\sqrt{\pi a}} \qquad \text{Equation 2.7}$$

where K_c is the toughness of the brittle component. The fracture toughness is ~1 MPa$\sqrt{m}$ for aragonite (20) and ~1.2 MPa$\sqrt{m}$ for hydroxyapatite (21). From Figure

2.3, the elastic modulus of aragonite and hydroxyapatite is ~100 GPa. Estimating that the theoretical strength of the material is $E/10$ (9, 19), this strength is reached at a length scale of ~25 nm. Biological structures therefore tend to use constituents for high strength by producing the constituents in the nanometre range.

2.3.2 Basic Building Blocks

2.3.2.1 Biominerals

One of the defining features of rigid biological systems that comprise a significant fraction of the structural biological composites is the existence of two components: a mineral and an organic component. The intercalation of these components occurs at the nano, micro, meso or macroscale and often takes place at more than one length scale. Table 2.2 exemplifies this incorporation of mineral and organic components for a number of systems. The mineral component provides strength and the organic component contributes ductility as expected in typical composite design. This combination of strength and ductility leads to high energy absorption prior to failure. The most common mineral components are calcium carbonate, calcium phosphate (hydroxyapatite) and amorphous silica, although over 20 minerals (with principal elements being Ca, Mg, Si, Fe, Mn, P, S, C and the light elements H and O) have been identified. These minerals are embedded in complex assemblages of organic macromolecules that are hierarchically organized. The natural world is dominated by keratin, collagen and chitin acting as organic macromolecular frameworks.

Table 2.2 Principal components of common structural biological composites (10).

	Mineral					Organic				
Biological Composite	**Calcium Carbonate**	**Ca**	**Silica**	**Hydroxy Apatite**	**Other**	**Keratin**	**Collagen**	**Chitin**	**Cellulose**	**Other**
Shells	X									X
Horns		X				X				
Bones				X			X			
Teeth				X						X
Bird Beaks		X				X				
Crustacean Exoskeleton	X							X		X
Insect Cuticle								X		X
Woods									X	
Spicules			X							X

Table 2.3 below shows the minerals that have been identified in biological systems (22). The number of minerals is relatively limited compared to the range of functions required by the biological organism.

Table 2.3 Principal minerals found in biological systems (22).

Carbonates	Calcite	Amorphous calcium carbonate family
	Aragonite	Hydrocerrusote
	Vaterite	Protodolomite
	Monohydrocalcite	
Phosphates	Carbonated apatite (dahllite)	Brushite
	Francolite	Amorphous calcium phosphate family
	Octacalcium phosphate	Vivianite
	Whitlockite	Amorphous pyrophosphate
	Struvite	
Halides	Fluorite	Amorphous fluorite
	Hieratite	Atacamite
Sulfates	Gypsum	Jarosite
	Celestite	Calcium sulfate hemihydrate
	Barite	
Silicates	Silica (opal)	
Oxides and hydroxides	Magnetite	Amorphous manganese oxide
	Goethite	Amorphous ilmenite
	Lepidocrocite	Todotokite
	Ferrihydrite	Birnessite
	Amorphous iron oxide	
Sulfides	Pyrite	Galena
	Amorphous pyrrhotite	Greigite
	Hydrotroilite	Mackinawite
	Shalerite	Wurtzite
Native element	Sulfur	
"Organic Minerals"	Whewellite	Uric acid
	Weddelite	Paraffin hydrocarbon
	Manganese oxalate	Wax
	Calcium tartrate	Magnesium oxalate (glushinskite)
	Calcium malate	Copper oxalate (moolooite)
	Earlandite	Ferric oxalate anhydrous
	Guanine	Sodium urate

Organic molecules in solution can influence the morphology and orientation of inorganic crystals if molecular complementarity at the crystal-additive interface occurs (20). Understanding the process in which living organisms control the growth and structure of inorganic materials could lead to significant advances in materials science, allowing novel synthesis techniques for nanoscale composites. Mann (23) states that in order to address the question of nanoscale biologically induced phase transformations and crystallographic control we must study the

bonding and reactivity of extended organized structures under the mediation of organic chemistry. We examine two important processes of nucleation and morphology to describe the formation of the hard phase in biological structures.

The control of nucleation of inorganic materials in nature is achieved by the effect of activation energy dependency on organic substrate composition. Inorganic precipitation is controlled by the kinetic constraints of nucleation. Mann (23) states that this activation energy may also depend on the two-dimensional structure of different crystal faces, indicating that there is a variation in complementarity of various crystal faces and the organic substrate. Weissbuch et al. (24) describe the auxiliary molecules which promote or inhibit crystal nucleation depending on their composition.

The morphology of the inorganic material created in nucleation is controlled through the interaction with the organic matrix. Activation energies can be influenced in the presence of an organic matrix in three possible ways. Firstly, Figure 2.4 describes the possibilities of polymorphic nucleation (23). The activation energies of two non-specific polymorphs, 'A' and 'B', are shown in the presence (state 2) and absence (state 1) of the organic matrix. If 'A' is more kinetically favoured in the absence of the organic matrix then it is possible to examine the effect of the organic phase on the activation free energy ($\Delta G^{\#}$) of various polymorphs with respect to each other. In the first case both polymorphs are affected equally, thus 'A' remains kinetically favourable. In the second case the effect on the 'B' polymorph is much larger than for 'A' and thus, when in the presence of the organic matrix, 'B' is

kinetically favourable. In the last case we see a combination of the two earlier cases, in which the kinetic favourability of the two polymorphs is influenced by genetic, metabolic, and environmental processes.

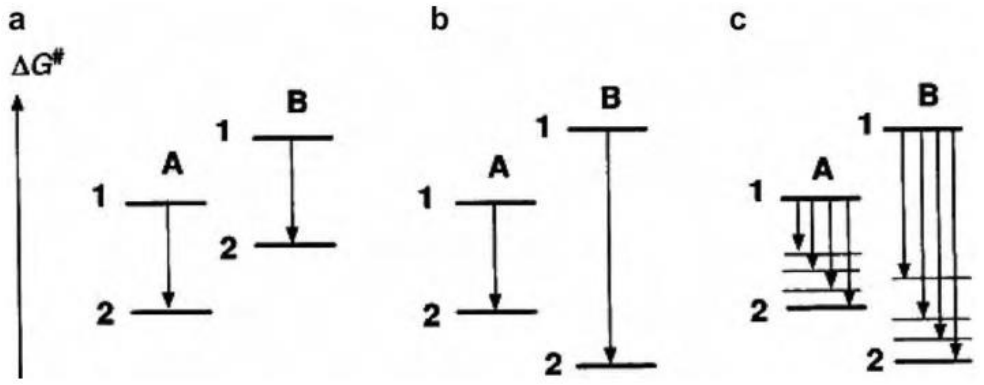

Figure 2.4 Structural control by organic matrix-mediated nucleation. (a) Promotion of non-specific nucleation in which both polymorphs have the activation energies reduced by the same amount; (b) promotion of structure-specific nucleation of polymorph B due to more favourable crystallographic recognition at the matrix surface; (c) promotion of a sequence of structurally non-specific to highly specific nucleation (25).

The selection of the polymorph will also be determined by the transformation sequence. This starts, in Figure 2.5, with an amorphous mineral and continues through a series of intermediate structures that have the same composition but decreasing free energy (increasing thermodynamic stability) (23, 26). This cascade is shown in Figure 2.5 and will either follow the one step route (A) or travel along a sequential transformation route (B) depending on the activation energies of nucleation, growth, and transformation. Addadi et al. (27-29) proposed that the role of the solid-state amorphous precursor phase could be fundamental in the biomineralization process.

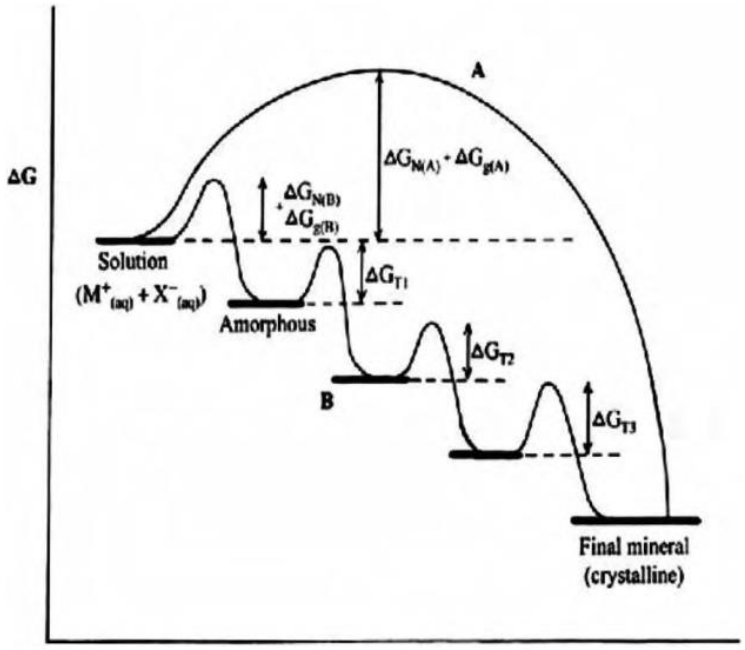

Figure 2.5 Representation of activation energies of nucleation in the presence and absence of an organic matrix for two non-specific polymorphs (25).

The composition of the complex structure in biological composites is mediated by the phase transformations, which occur by surface dissolution of the precursor. The phase transformation is dictated by the solubility of amorphous precursor into the crystalline intermediates, and the effect of these precursors on the free energies of activation of these interconversions. Thus an animal that is able to control its emission of molecular precursor (organic matrix, or soluble protein) will be able to control the growth and structure of its inorganic biocomposite. Addadi and Weiner (27) and Addadi et al. (28, 29) demonstrated the stereoselective adsorption of proteins in the growth of calcite crystals resulting in a slowing down of growth in the c-direction and altering the final shape of the crystal. This evidence of the influence of organics on inorganic crystal growth led them to examine the influence of proteins on the morphology of crystal growth.

2.3.2.2 Biopolymers

The organic structures formed from cellular activity provide the framework in the biomineralization process. The organic material is typically a complex protein polymer, referred to as a biopolymer. Most proteins are complex macromolecules but typically incorporate amino acid chemistry containing both amine ($-NH_2$) and carboxyl (-COOH) groups, with this chemical structure shown in Figure 2.6:

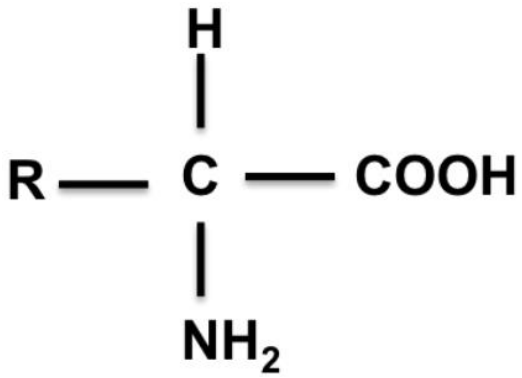

Figure 2.6 Chemical structure of amino acids containing an amine and carboxyl group. R represents organic side groups.

Twenty common amino acids are used in proteins, with the common amino acids given as: Arginine (Arg), Asparagine (Asn), Aspartate (Asp), Glutamine (Gln), Glycine (Gly), Histidine (His), Isoleucine (Ile), Methionine (Met), Threonine (Thr), Tryptophan (Trp), Tyrosine (Tyr), and Valine (Val) (30). The amino acids form linear chains similar to polymer chains known as polypeptide chains. These polypeptide chains acquire distinct configurations through the formation of bonds (hydrogen, van der Waals, and covalent bonds) between amino acids on the same or different chains. The two most common configurations are the alpha helix and the beta sheet

as shown in Figure 2.7. The alpha helix is formed due to hydrogen bonding between adjacent NH and CO groups in separate chains that facilitate helical shape. This structure can shift towards a beta sheet configuration shown in Figure 2.7b.

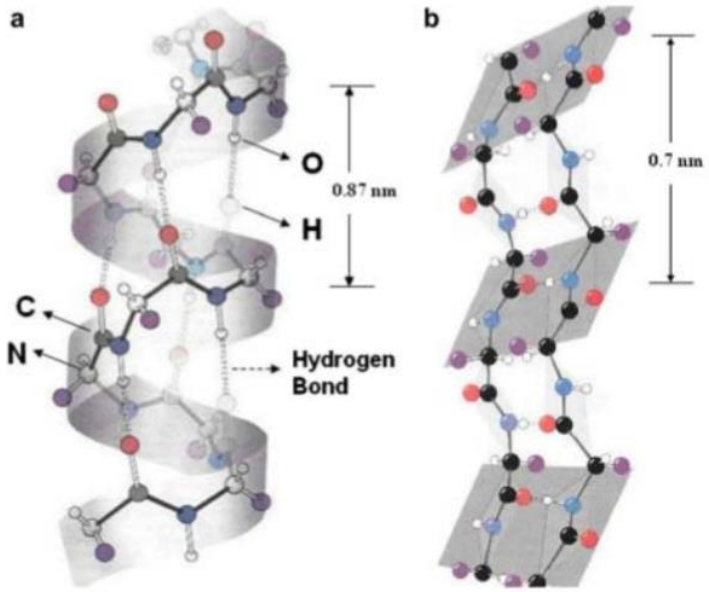

Figure 2.7 (a) Structure of alpha helix; dotted double lines indicate hydrogen bonds; (b) structure of beta sheet with two anti-parallel polypeptide chains connected by hydrogen bonds (double dotted lines) (31).

Further detail on the alpha helix structure is shown in Figure 2.8. The hydrogen bonds that hold the polymer chains together, shown in Figure 2.8a as present in both the alpha helix and beta sheet, are combined with steric repulsion from the organic side groups to give the alpha helix structure.

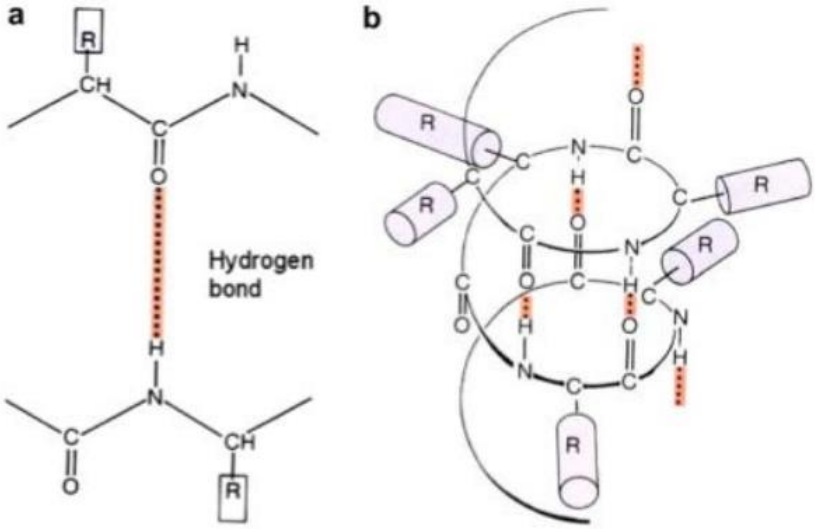

Figure 2.8 (a) Hydrogen bond connecting a CO to a NH group in a polypeptide; (b) successive hydrogen bonds on same polypeptide chain leading to formation of a helical arrangement (32).

Organic frameworks require the combination of proteins using the amino groups present on the polymer chains to form fibrous constituents. These fibrous constituents can then build further structures, as will be discussed, and act as the template from which mineralization can occur. Interestingly, the majority of organic frameworks are formed from fibrous materials constructed from the following biopolymers (20):

• Polypeptide chains, which are the building blocks for collagen, elastin, silks and keratins.

• Polysaccharides, the building blocks for cellulose and hemicellulose.

• Hybrid polypeptide–polysaccharide chains, the building blocks for chitin.

For example, mammals use polypeptide chains almost exclusively to form fibrous collagen constituents as a framework for mineral formation whereas a number of

sea creatures use corresponding fibres constructed from polysaccharides. Therefore, while the biopolymers used by organisms can change, the principal of an organic framework holds in all mineralized tissue.

2.3.3 Mechanical Analysis of Structural Biological Composites

A wide range of mineralized biological composites are hierarchically structured beginning from the smallest length scale with mineral nano-fibres, -platelets, or -spheres which are embedded within proteins and arranged into superordinate structures at larger dimension levels. For example, hierarchical structuring can embrace up to 7 levels of hierarchy (33) within bone where the largest structural elements can reach length scale of millimetres (33). Table 2.4 gives a brief overview of the hierarchical structures of some mineralized biological materials discussed in this section. All these materials are built from the bottom up with the first composite level consisting of mineral platelets, fibres or spheres embedded within a protein phase. The levels of hierarchy are counted from this first mineral-protein composite level up to the bulk material level.

Table 2.4 Overview of selected biological materials with a brief description of their hierarchical structures (34).

Material	Mineral content [vol.%]	Structure	Levels of hierarchy
Nacre (20, 35-37)	95	Aragonite nano-grains are glued together to form nano-platelets **(1)** which are staggered into a brick- and mortar-like structure, enveloped by proteins **(2)**	2
Enamel (38)	85	Hydroxyapatite nano-fibres **(1)** are bundled together to micro-fibres ('rods') **(2)** which are partially arranged in a superordinate decussated structure **(3)**	3
Sponge spicule (39-42)	89	Hydrated silica nano-spheres **(1)** are arranged into lamellae **(2)** which are arranged concentrically around a central cylinder **(3)**	3
Dentin (43)	45	Collagen fibrils are reinforced by hydroxyapatite nano-platelets **(1)** and form a network-like structure **(2)** around the dentinal tubules which are cylindrically shaped and surrounded by a highly-mineralized cuff **(3)**	3
Conch shell (44, 45)	99	Layered, ply-wood like structure: Three meso-layers **(1)** 0^o /90^o /0^o are composed by first-order lamellae in a $\pm 45^o$ orientation **(2)**. Each first-order lamella consists of second-order lamellae **(3)** which in turn consist of single crystal third-order aragonite lamellae **(4)**	4
Cortical bone (33)	40	Collagen fibrils are reinforced by hydroxyapatite nano-platelets **(1)** and assemble into fibres **(2)** which are arranged into lamellar sheets **(3)** which are arranged concentrically into Haversian systems **(4)** which are arranged in parallel to the bone long axes **(5)**	5
Antler bone (46, 47)	36	Structure similar to cortical bone but less mineralized	5

In general, investigations of mechanical properties of biological materials can be divided into two major groups, namely micro/nanoindentation and miniaturized

bulk mechanical testing. On the one hand, mechanical properties such as elastic modulus, hardness and toughness are determined via indentation methods. In a traditional indentation test (macro or microindentation), a hard tip whose mechanical properties are known (frequently made of a very hard material like diamond) is pressed into a sample whose properties are unknown. The load placed on the indenter tip is increased as the tip penetrates further into the specimen and soon reaches a user-defined value. At this point, the load may be held constant for a period or removed. The area of the residual indentation in the sample is measured and the hardness, H, is defined as the maximum load, P_{max}, divided by the residual indentation area, A_T:

$$H = \frac{P_{\max}}{A_T} \qquad \text{Equation 2.8}$$

Nowadays nanoindentation has superseded microindentation due to the need to understand the mechanical properties of nanoscale constituents. Table 2.5 (34) summarizes data determined via indentation tests for biological materials described in Table 2.4. As the issue of this section is to understand and discuss the mechanical properties of biological materials in regards to their hierarchical structures, the data presented here is allocated according to the hierarchical level classification presented in Table 2.4.

As can be seen, indentation techniques are appropriate to determine the mechanical properties of small structural elements at the microscale or nanoscale. However, several problems need to be solved before applying small length scale mechanical testing techniques to perform compression, bending or tensile tests for elastic

modulus, strength and toughness of biological materials. Firstly, the sample preparation of relatively small specimens requires suitable isolation and manipulation from bulk specimens. Secondly, standard experimental setups for mechanical testing of such small samples are uncommon and new techniques need to be developed. Indentation testing remains perhaps the only standard test that is sufficient to measure the mechanical properties of materials at small length scales. Nanoindentation has been applied to measure the elastic modulus, strength and toughness of many biological material and structure constituents in a range of loading modes as summarized in Table 2.5 below.

Table 2.5 Characterization of biological materials via indentation (34).

Material	Level of hierarchy tested	Elastic modulus [GPa]	Hardness [GPa]	Fracture toughness [MPa·m$^{1/2}$]
Nacre	2: staggered platelet arrangement	30-120 (12, 36, 48, 49)	0.5-8 (12, 36, 48, 49)	6.8 (49)
Enamel	0: single crystals 1: nano-fibre arrangement ('intra-rod') 2: multiple rods	40-115 (50) 120 (50) 80-82 (49-51)	2.5-4 (51, 52)	0.5-1.3 (49)
Sponge spicule	1: nano-sphere arrangement (single concentric layer) 2: layered structure	42-43 (41) 41-42 (41) 35 (39)	4.2-4.4 (41) 3.8-4.1 (41) 2.5-3 (39)	0.84 (53)
Dentin (43)	2: intertubular dentin network	17-21 (54)	0.49-0.52 (54)	Material too soft for indentation toughness measurements (55)

Conch shell	2: peritubular highly-mineralized cuff 2: second-order lamella structure	29 (54) 60-100 (56)	2.2-2.5 (54) 3-6 (56)	Highly damaged zone around indents but no well-defined radial cracks for toughness calculations (57)
Cortical bone	4: single Osteon lamellae 4: interstitial lamella	Dry: 22.5 Wet: 18 (58, 59) Dry: 25.8 Wet: 18 (58, 59)	0.4-0.6 (58, 59)	0.5-2 (60)
Antler bone	4: lamellae	5.5-7.6 (61)	0.16-0.21 (61)	

Biological materials simultaneously adopt a generic nanostructure consisting of protein and mineral, suggesting a convergent evolution of the microstructural design of biomaterials at the microscale or nanoscale, from previous studies (18, 19) examining the mechanical properties of different biological materials. Ji and Gao et al. (18, 19) found that nanostructures play critical roles in the stiffness and toughness of biological materials through a so-called tension-shear chain (TSC) model. Gao et al. (19, 62-64) carried out a series of studies on the mechanical properties of biological nanostructure, including fracture strength of the mineral phase becomes insensitive to existing flaws and approaches theoretical strength limits when the dimensions of the mineral crystal approach critical nanometre length scales.

While the reduction of the size of mineral crystal can enhance the fracture strength and toughness of the nanocomposite structure, this size reduction significantly increases the interfacial region of mineral and protein in bulk structures. For example, the area of the interfacial region can be as large as a football field in a rain-drop-size volume of a nanocomposite (65). Nanocomposites can therefore be considered as 'interface' materials, and thus the interface plays more dominant roles in their mechanical properties in comparison with the conventional composites. In particular, many biological materials, such as bone, teeth and shells, are polymer nanocomposites of protein and mineral that have drastically different in mechanical properties: mineral is hard and brittle, but protein is soft, tough, and as a typical biopolymer its molecular conformation largely determines mechanical properties. Experimental studies have suggested that the static Coulomb force might dominate the interaction between mineral and protein in biological materials (66-69). However, to date, it is still unclear what mechanisms dominate the fracture strength and toughness of this hybrid interface and how the interface configuration changes when the materials deform and fail.

At the most elementary structure level, biological composites exhibit a generic microstructure consisting of staggered mineral bricks as shown in Figure 2.9a. Jaeger and Fratzl (70) discussed the mineral platelet arrangement in collagen fibrils and developed a simple mechanical model to estimate the stiffness of biocomposites. Under an applied tensile stress, the Jaeger-Fratzl model can be schematically represented by Figure 2.9b, where the mineral platelets carry the tensile load while the protein matrix transfers the load between mineral crystals via shear. The path of

load transfer in the composite is thus simplified to a one-dimensional serial spring system consisting of mineral elements (tension) interspersed among protein elements (shear) (19). The large aspect ratio of mineral platelets compensates for the low modulus of the protein phase. According to this simple model, the stiffness (Young's modulus) E of the composite can be expressed as:

$$\frac{1}{E} = \frac{4(1-\Phi)}{G_p \Phi^2 \rho^2} + \frac{1}{\Phi E_m} \qquad \text{Equation 2.9}$$

where E_m is the elastic modulus of mineral, G_p is the shear modulus of protein, Φ is the volume concentration of mineral, and ρ is the aspect ratio of the mineral platelets. The equation above indicates that the high stiffness of biocomposites is achieved by the large aspect ratio of mineral platelets, with most of the load carried by the hard mineral platelets via stress transfer through protein between the mineral.

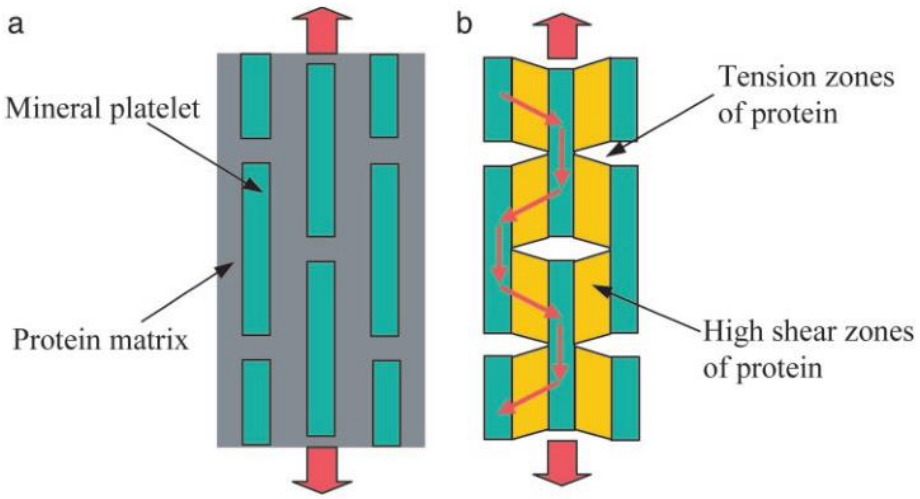

Figure 2.9 A model of a biocomposite. (a) A schematic diagram of staggered mineral crystals embedded in protein matrix. (b) A simplified model showing the load-carrying structure of the mineral–protein composites. Most of the load is carried by the mineral platelets whereas the protein transfers load via the high shear zones between mineral platelets (19).

Gao and Ji (19) applied a Griffith criterion to indicate that the strength of the mineral plate in a biocomposite as shown in Figure 2.9 is equal to the theoretical strength when the mineral size drops below 30 nm, even if flaws were present within the mineral itself. Therefore, the mineral phase in biological structures are theoretically expected to be insensitive to flaws at this scale. Gao et al. (71) and Gao and Ji (19) proposed a conceptual framework that explains the lowest scale of the structural elements in hard biological materials (bone, teeth, and shells) and applied Griffith's criterion to the mineral components of hard biological materials thus:

$$\sigma_f = \alpha\left(\frac{E\gamma}{h}\right)^{1/2} \qquad \text{Equation 2.10}$$

Where γ is the surface energy of the mineral, α is a proportionality constant, and h is the thickness of the mineral. Gao defined a parameter ψ by:

$$\Psi = \sqrt{\frac{\gamma}{Eh}} \qquad \text{Equation 2.11}$$

Where, for the thumbnail crack shown in Figure 2.10a, the value of α is $\sqrt{\pi}$. The theoretical stress, σ_{th}, has been defined, according to the Orowan criterion (72), for crystalline materials, as:

$$\sigma_{th} \cong \frac{E}{n},\ 2\pi < n < 30 \qquad \text{Equation 2.12}$$

The analysis predicts a limiting value of h (or a), for which the strength is no longer size dependent, as:

$$h^* \cong \alpha^2 \frac{\gamma E}{\sigma_{th}^{\ 2}} = \frac{\alpha^2 n\gamma}{E} \qquad \text{Equation 2.13}$$

This critical value of about 30 nm was calculated for bone, which is the approximate size of the mineral platelets observed experimentally (33). The critical value of ψ, ψ^*, is marked in Figure 2.10b.

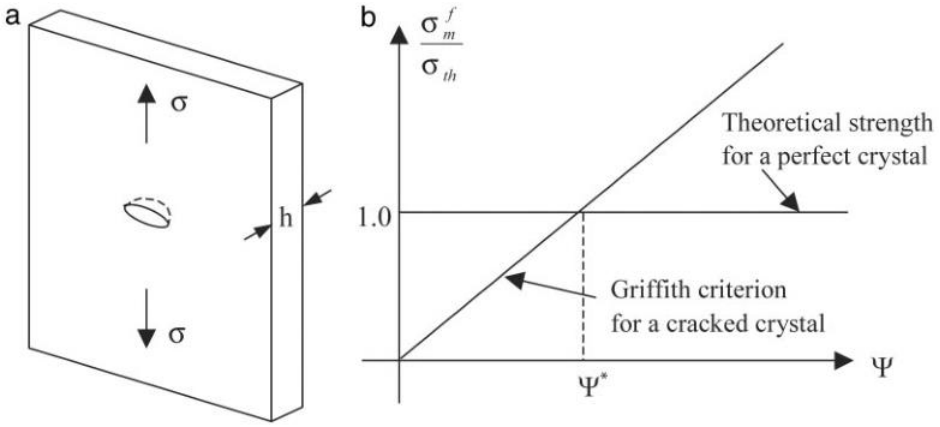

Figure 2.10 A length scale for optimized fracture strength in mineral platelet. (a) Schematic of a mineral platelet with a surface crack (Griffith analysis); (b) comparison of the fracture strength of a cracked mineral platelet calculated from the Griffith criterion with that of a perfect crystal (71).

Meyers et al. (73) used a similar approach to Gao et al. (71) to examine the strength of the nanoscale components in abalone shell. Abalone shell has a complex structure, as will be discussed later in this chapter, but contains nanoscale mineral bridges that have the potential to be high strength due to the relatively small size. These mineral bridges are shown in Figure 2.11a and b, with the corresponding schematic indicating sub 100 nm features. The calculation of the mineral bridge strength is shown in Figure 2.11c and highlights a rapid increase in the mineral strength as the bridge diameter decreases. This work suggested that the mineral bridge diameters are design to maximize strength.

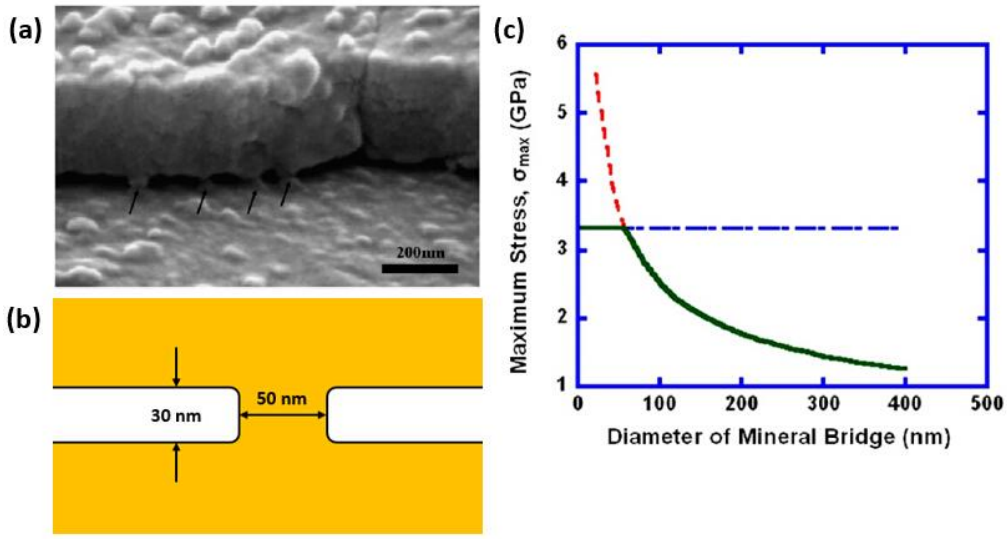

Figure 2.11 (a) SEM micrograph showing mineral bridges (marked by arrows) between tile layers (73). (b) Schematic showing the nanoscale mineral bridges connecting layers of aragonite tiles. (c) Tensile strength of mineral as a function of bridge diameter (73).

2.4 Nacre

2.4.1 Hierarchical Structure

Nacre is a biological composite that has been extensively studied due to its highly organized hierarchical structure and its exceptional mechanical properties (12, 74-80). Nacre is part of the two-layer armour system adopted by most molluscs to protect their soft bodies from marine predators and other mechanical aggressions such as rocks or debris displaced by currents and waves. As shown in Figure 2.12b, the outer layer of shells consists of large prismatic calcite grains (rhombohedral calcite) which are hard and appropriate to withstand impact against shells, but prone to brittle failure (81). However, nacre is relatively ductile, capable of bearing

larger inelastic deformation than the pure mineral phase and dissipating mechanical energy during impact process (82). In order to achieve such mechanical performance, the structure of nacre is well organized at multiple length scales. Nacre is composed of 95% highly organized mineral calcium carbonate ($CaCO_3$) tablets in the aragonite form separated by 20 to 50 nm thick layers of biopolymer mortar mainly composed of proteins and polysaccharides (36, 77, 83). The mineral is in the form of hexagonal tablets 5 to 15 μm in diameter and 0.2 to 0.5 μm in thickness. These tablets are strictly arranged as an interlocked 'brick and mortar' structure, as shown in Figure 2.12.

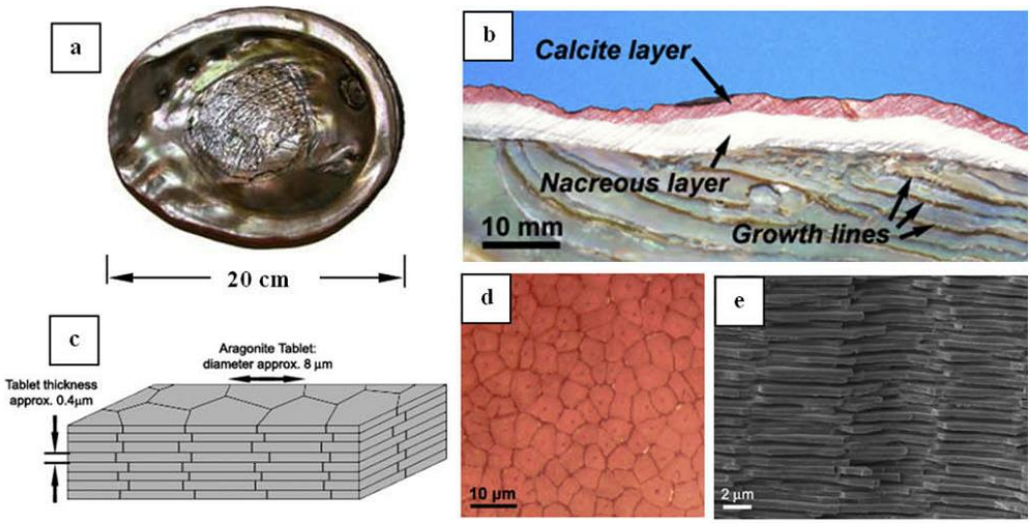

Figure 2.12 Nacre at different length scales (all images from red abalone): (a) inside view of the whole shell; (b) cross section of a red abalone shell; (c) schematic of the 'brick and mortar' structure; (d) top view optical micrograph showing the tiling of the tablets; (e) SEM image showing a fracture surface of nacre (84).

The aragonite tablets in nacre are normally described and modelled as flat at the microscale. However, closer observation reveals that this is not the case, and that the

interfaces between the tablets exhibit an evident waviness, as shown in Figure 2.13a and Figure 2.13b. Such features have been observed by a number of methods, such as optical microscopy, scanning electron microscopy (SEM), transmission electron microscopy (TEM) and atomic force microscopy (AFM) (12, 85, 86). The waviness of the tablets in nacre was also detected using a laser profilometer, as shown in Figure 2.13c. AFM on the opposed faces of a cleaved sample (Figure 2.13d) reveals that the topology of the surface from one tablet to the next is highly conformal, making the tablets fit together perfectly.

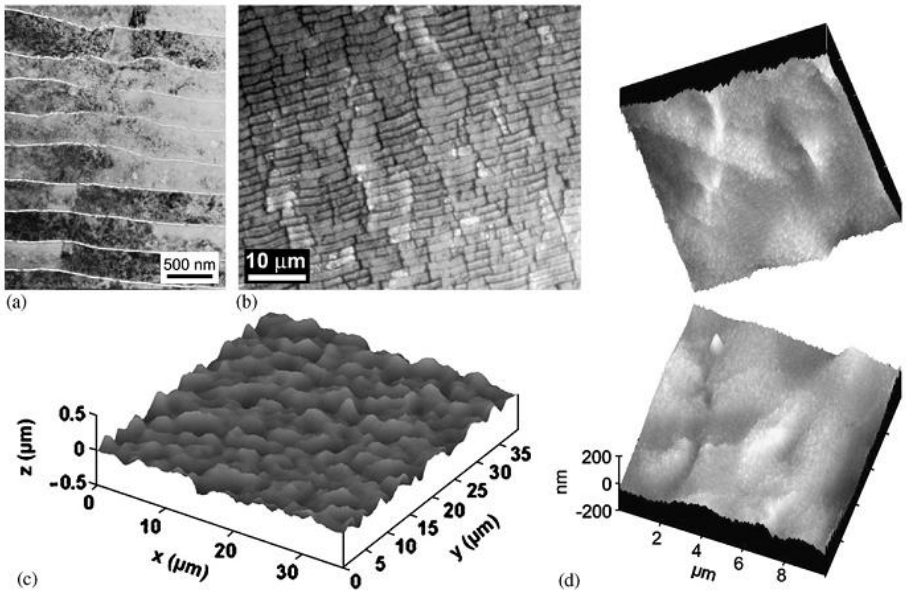

Figure 2.13 Nacre at the microscale. (a) TEM of nacre from red abalone showing tablet waviness; (b) optical micrograph of nacre from fresh water mussel Lampsilis Cardium; (c) layer topology from laser profilometry; (d) AFM images of opposed tablets (36, 87).

The smallest features in the hierarchical architecture of nacre are observed at the nanoscale. The tablets are composed of single aragonite grains, with the [001] crystallographic orientation normal to the plane of the tablets. Figure 2.14a presents

a TEM image that demonstrates the existence of nanograins within the tablets. The interface between the tablets is a complex multi-layer system mainly composed of biopolymer species with the thickness of 20 - 30 nm (87). Aragonite bridges and nanoasperities on the surface of the tablets are observed using high resolution TEM (Figure 2.14b and Figure 2.14c), both of which are believed to provide direct mechanical interaction between tablets (76, 88). AFM imaging of a cleaved sample exhibits the distribution of these nanoscale features on the surface of the tablets, as shown in Figure 2.14d. The density and size of these features vary from one area to another (36), and on average they are 10 - 30 nm in height and width, with spacing of the order of 100 - 200 nm. All of the structural features identified in this section at different length scales have a potential influence on the mechanical performance of nacre, which will be discussed in detail in the next section.

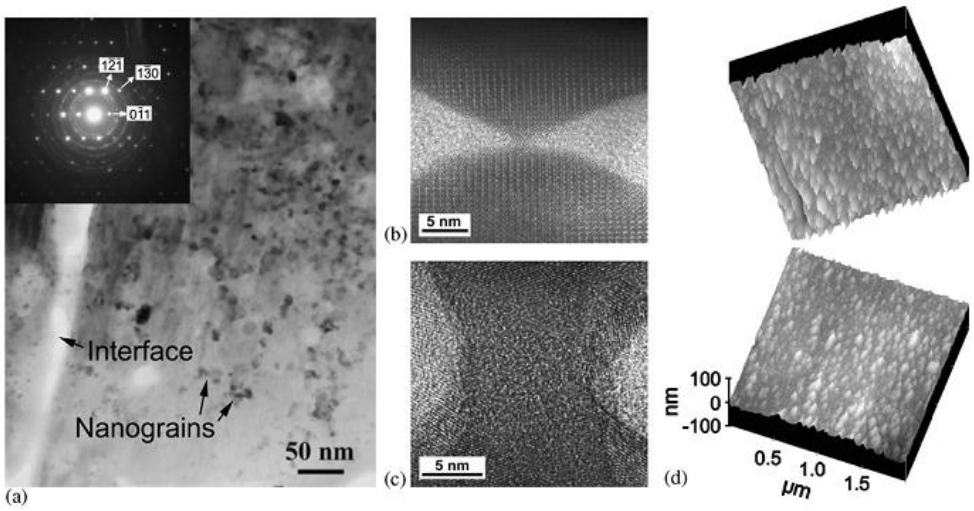

Figure 2.14 Nacre at the nanoscale. (a) TEM of a nacre tablet, showing nanograin inclusions; (b) high resolution TEM of asperity inside a tablet interface; (c) high resolution TEM of an aragonite bridge connecting two tablets across the interface; (d) AFM images of opposed tablet surfaces showing nanoscale features (76, 88).

2.4.2 Mechanical Properties

The superior mechanical properties of nacre were first revealed by Currey (89) who performed measurements of mechanical properties of nacre from a variety of bivalves, gastropods and cephalopods. The studies demonstrated that nacre had a fracture strength in bending varying between 56 and 116 MPa and the maximum measured strain was 0.018. The work of fracture varied significantly in different loading directions, being about 1.65×10^3 J·m^{-2} when fractured across the grain, and 1.5×10^2 J·m^{-2} when fractured along the grain. Currey indicated that the tablet geometry and arrangement were optimized for stiffness as well as energy absorption, with nacre exhibiting considerable ability to stop cracks leading to catastrophic failure. Further investigation of nacre was performed by Jackson et al. (85) who studied the effect of hydration on nacre from the shell of a bivalve mollusc, *Pinctada*. This work reported a Young's modulus difference of approximately 70 GPa for dry samples (ambient conditions) and 60 GPa for hydrated samples (soaked in water); the tensile strength of nacre was demonstrated to be 170 MPa for dry and 140 MPa for hydrated samples. The work of fracture varied from 350 to 1240 J·m^{-2}, depending on the species, degree of hydration, span-to-depth ratio and the orientation of load applied. Hydrated nacre showed superior toughness by associated introduction of plastic work. In contrast, monolithic calcium carbonate showed a work of fracture up to 3 orders of magnitude lower than that of nacre (74, 85). Jackson et al. (85) concluded that water affects the Young's modulus and tensile strength by reducing the shear modulus and strength of the organic matrix. The toughness of nacre is enhanced by water, which plasticizes the organic mortar with

the result of enhanced crack blunting and deflection ability (85). Compared with traditional brittle ceramics (Al_2O_3) and high toughness ceramics (ZrO_2), the crack propagation behaviour of nacre reflects its highly anisotropic structure resulting in a high degree of crack tortuosity (90). Jackson et al. thus concluded that the increased path length of cracks is responsible for enhanced work of fracture. Meyers (91) also observed crack deflection at the thick (20 μm) organic interfaces mesolayers.

The deformation behaviour of nacre has been experimentally studied via a variety of methods including tensile (89, 92) and compressive (36, 77) tests, three and four point bending tests (74, 85) and shear test (92, 93). The mechanical behaviour of macroscopic nacre at high strain rates was also characterized by Menig et al. (77). Besides these mechanical tests at the macroscale, nanoindentation on individual aragonite tablet (12, 36) and load-extension curves on single molecules of organic matrix in nacre (13) were used to detect the mechanical response of individual components of nacre at smaller length scales. At the macroscale, the most significant mode of deformation is the uniaxial tensile test along the direction of the tablets. In considering the two-layer armour system of seashells discussed in Section 2.4.1, the outside layer is always subjected to compressions and impacts, thus the inside nacreous layer is subjected to tension along the tablets most of the time. Figure 2.15a and 2.15c presents the stress-strain curves of nacre in tensile and shear tests and the associated deformation modes as shown in Figure 2.15b and 2.15d, showing some ductility at the macroscale. The stress-strain curves show relatively large deformations, accompanied by hardening up to failure at a strain of around 2%.

Unloading paths show a decrease in elastic modulus, resulting from progressive accumulation of damage. The tensile behaviour of aragonite is also shown in Figure 2.15a and indicates a linear elastic deformation followed by sudden, brittle failure at relatively small strain. Nacre therefore exhibits ductile behaviour with relatively large failure strains despite being made of 95% by volume of brittle aragonite mineral.

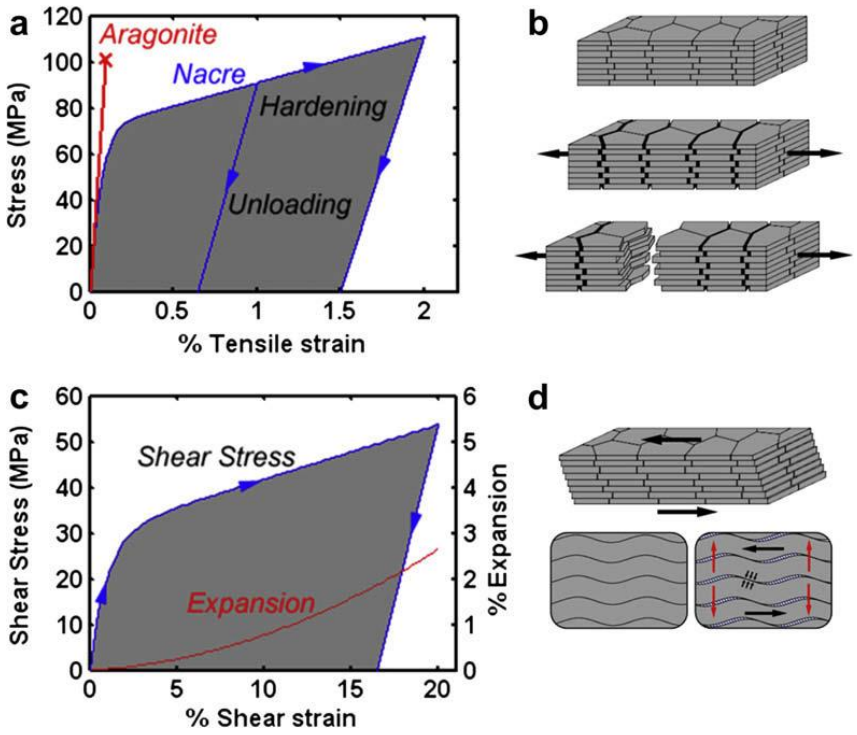

Figure 2.15 (a) Experimental tensile stress-strain curve for nacre and (b) associated deformation modes. (c) Experimental shear stress-strain curve for nacre and (d) deformation mechanism. Tablet waviness generates resistance to sliding, accompanied by lateral expansion (red arrows) (94).

2.5 Arthropod Exoskeleton

2.5.1 Hierarchical Structure

Arthropods are the largest phylum of animals including the trilobites, chelicerates (spiders, mites, and scorpions), mariapods (millipedes and centipedes), hexapods (insects), and crustaceans (crabs, shrimps, lobsters, and others). All arthropods are covered by a rigid exoskeleton, which is periodically shed as the animal grows. The multifunctional arthropod exoskeleton supports the body mass, resists mechanical loads as well as providing environmental protection and resistance to desiccation (95-98). The three main components of exoskeleton are chitin, polysaccharide, structural proteins, and inorganic minerals, typically calcium carbonate. The exoskeleton is a multi-layered structure and can be observed under optical microscope. The outermost layer is the epicuticle, a thin, waxy layer that is the main waterproofing barrier. Beneath the epicuticle is the procuticle, the main structural part primarily designed to resist mechanical loads. The procuticle is further divided into two parts, an exocuticle and an endocuticle (99). The exocuticle (outer layer) and endocuticle (inner layer) are similar in structure and composition. The difference between exocuticle and endocuticle is that the exocuticle is stacked more densely while the endocuticle is sparsely stacked. Generally, the layer spacing in the endocuticle is about three times thicker than that in the exocuticle.

The most characteristic feature of arthropod exoskeletons is their well-defined hierarchical organization which reveals different structural levels as shown in Figure 2.16. At the molecular level is the polysaccharide chitin which arrange into an anti-parallel fashion forming α-chitin crystals. The next structure level consists of 18 - 25 of such molecules, wrapped by proteins, forming nanofibrils of about 2 - 5 nm in diameter and about 300 nm in length. These nanofibrils further assemble into bundles of fibres of about 50 - 300 nm in diameter. The fibres then arrange parallel to each other and form horizontal planes. These planes are stacked in a helicoid fashion, creating a twisted plywood or Bouligand structure (100-103) that have completed a 180° rotation in organization, which further forms the exocuticle and endocuticle. The Bouligand (helical stacking) arrangement provides structural strength that is in-plane isotropic (x-y plane) in spite of the anisotropic nature of the individual fibre bundles. In crustaceans, the minerals are mostly in the form of crystalline $CaCO_3$, deposited within the chitin-protein matrix (23, 25, 104, 105). The highly mineralized Bouligand arrangement provides strength in the in-plane (or in-surface) direction and can be considered as the hard or brittle component.

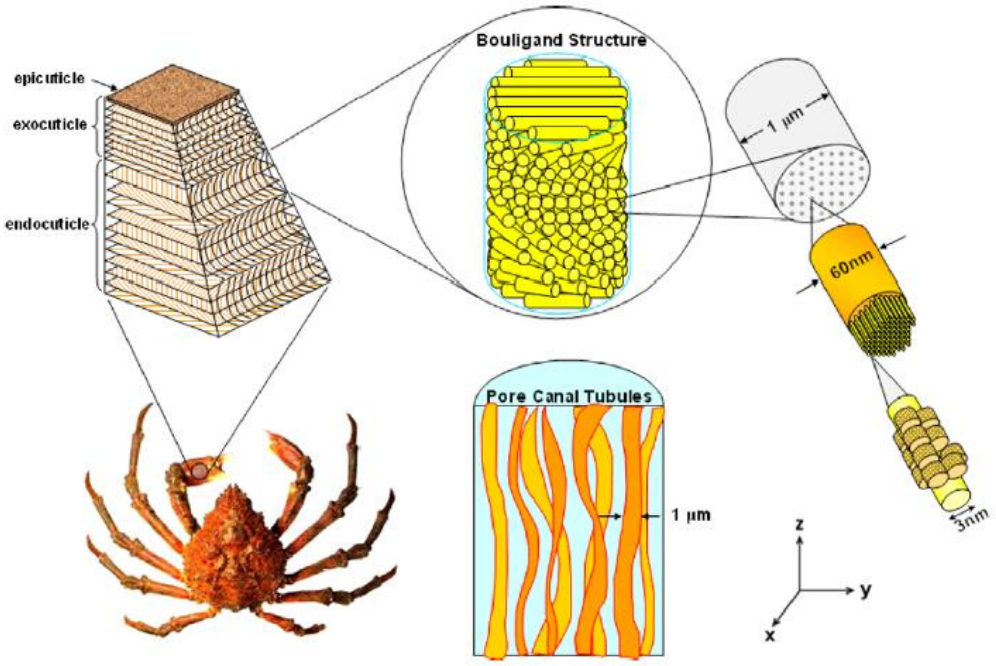

Figure 2.16 Hierarchical structure of the exoskeleton of sheep crab, Loxorhynchus grandis. Chitin fibrils (~3 nm in diameter) wrapped with proteins form a fibre of ~60 nm in diameter. Fibres further assemble into bundles, which form horizontal planes (x-y plane) superposed in a helicoid stacking, creating a twisted plywood structure through a 180° rotation. Ribbon-like tubules, 1 µm wide and 0.2 µm thick organize in the z-direction and run through the pore canals (106).

2.5.2 Mechanical Properties

The mechanical properties of crustacean exoskeletons (mud crab, *Scylla serrata* and the prawn, *Penaeus mondon*) were first investigated by Hepburn and Joffe (107, 108), followed by Raabe and co-workers (American lobster, *Homarus americanus*) (109-114) and Chen et al. (106) (sheep crab, *Loxorhynchun grandis* and Dungeness crab, *Cancer magister*). The tensile stress-strain curves for various exoskeletons are shown in Figure 2.17. The results from Hepburn and Joffe (99, 107) show a unique discontinuity (load drop) in the low strain region. The authors suggested that this

discontinuity is associated with the brittle failure of the mineral phase. When exoskeleton specimens are stretched, brittle failure of the mineral phase occurs at a low strain, leaving the chitin and protein phases to bear the load as shown in Figure 2.17. Table 2.6 additionally shows the mechanical properties of crustacean exoskeletons, highlighting the importance of water in defining mechanical properties. The dried exoskeleton material is therefore rigid and brittle compared to that in the hydrated state.

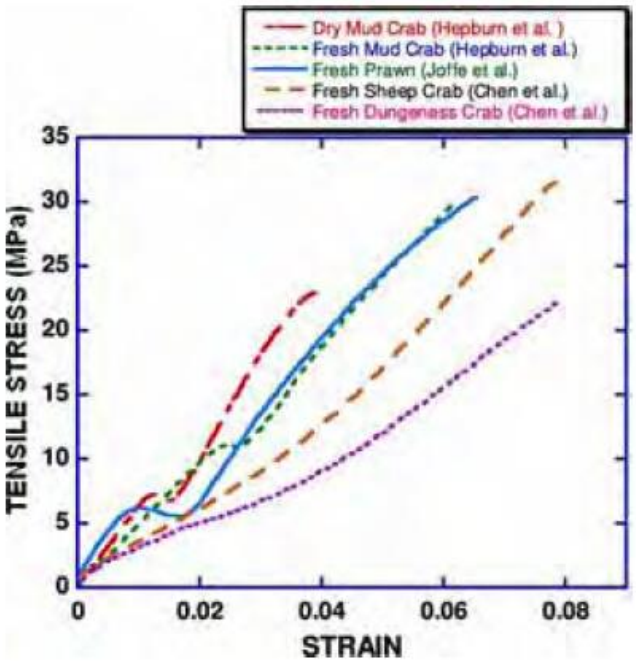

Figure 2.17 Tensile stress-strain curves for crustacean exoskeletons (20).

Table 2.6 mechanical properties of crustacean exoskeletons (106, 107).

Sample		UTS (MPa)	Young's modulus (MPa)	Fracture strain (%)
Sheep crab	Wet	29.8 ± 7.2	467 ± 92	6.9 ± 1.8
Loxorhynchus grandis	Dry	12.5 ± 2.3	735 ± 65	1.7 ± 0.3
Mud crab	Wet	30.1 ± 5.0	481 ± 75	6.2
Scylla serrata	Dry	23.0 ±3.8	640 ± 89	3.9
Prawn	Wet	28.0 ±3.8	549 ± 48	6.9
Penaeus mondon	Dry	29.5 ± 4.1	682 ±110	4.9

Melnick et al. (115) studied the hardness and toughness of exoskeleton of the stone crab, *Menippe mercenaria*, which exhibits a dark colour (ranging from amber to black) on tips of chelae and walking legs. The dark material was much harder and tougher than the light-coloured material from the same crab chela, as presented in Table 2.7. Scanning electron micrographs as shown in Figure 2.18 showed that the dark exoskeleton material has lower level of porosity, and this may relate to the tanning effect and more progressed mineralization.

Table 2.7 Mechanical properties of stone crab, Menippe mercenaria (115).

	Hardness (GPa)	Fracture strength, σ_f (MPa)	Fracture toughness, K_{Ic} (MPa·m$^{1/2}$)
Black	1.33	108.9	2.3
Yellow	0.48	32.4	1.0

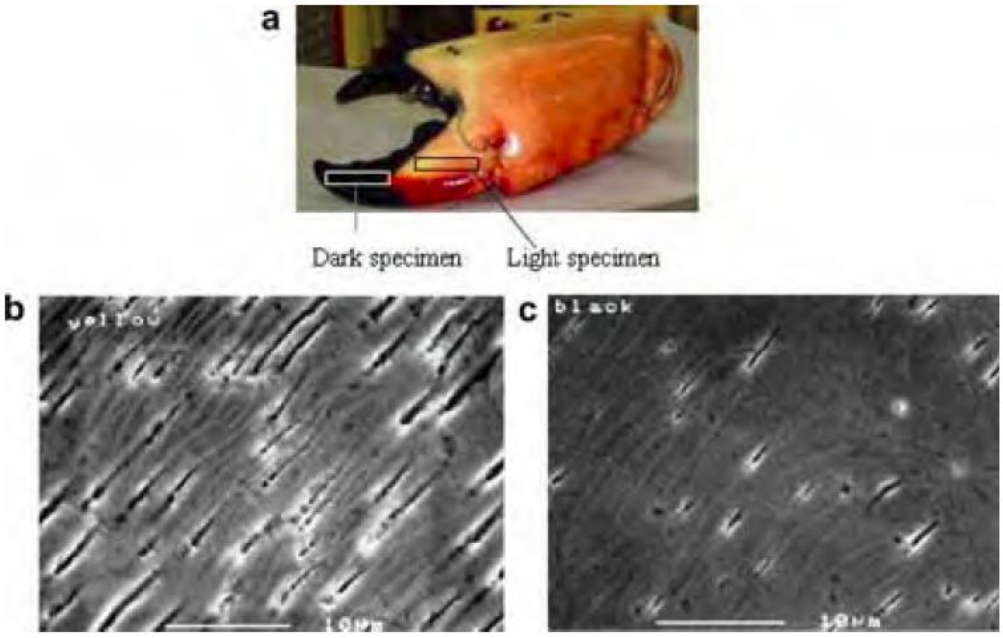

Figure 2.18 (a) Stone crab, Menippe mercenaria, chelae showing dark and light-coloured region. (b) SEM photograph showing high levels of porosity in yellow exoskeleton material. (c) SEM photograph showing high levels of porosity in black exoskeleton material (115)

Raabe and co-workers extensively studied the structure and mechanical properties of the exoskeleton of American lobster, *Homarus americanus* (109-114). The authors observed the unique honeycomb-type arrangement of the chitin-protein fibres surrounding pore canals, as shown in Figure 2.19. The through-thickness mechanical properties of American lobster exoskeleton were studied using both micro- and nanoindentation techniques (110, 111). The hardness and stiffness of the exocuticle (outer layer) are higher than those of endocuticle (inner layer). This increased hardness in exocuticle is due to the dense twisted plywood structure when compared to the coarse twisted plywood structure in endocuticle.

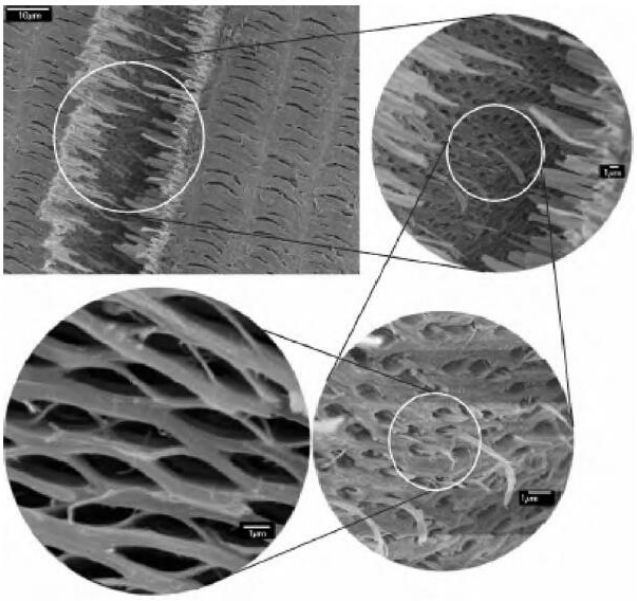

Figure 2.19 SEM micrographs taken from fractured specimens of lobster Homarus americanus showing the hierarchical structure. The honeycomb-type arrangement of the chitin-protein fibres is visible at higher magnifications (112).

2.6 Tendon-to-Bone Attachment

2.6.1 Mechanical Challenge of Attaching Tendon to Bone

Tendon and bone display dramatically different mechanical behaviour (116-118). At the hierarchical level of the tissue, tendon has a tensile modulus on the order of 200 MPa in the direction of muscle force, but buckles in compression (i.e., it behaves like a rope) (117). Bone, on the other hand, has a modulus of 20 GPa in both tension and compression, and is rigid and brittle relative to tendon (116). The attachment of a compliant material such as tendon to a relatively stiff material of bone is a

fundamental engineering challenge (119). As is evident from the study of attachment of engineering materials, potentially damaging stress concentrations can be expected to arise at the insertion if the insertion is not tuned to this stiffness mismatch. The tendon-to-bone insertion has a complex composition, structure, and mechanical behaviour that is effective in transferring stress from tendon to bone. However, this complex attachment results in a particularly difficult challenge for effective response to injury. The unique transitional tissue that exists between uninjured tendon and bone is not recreated during tendon-to-bone healing (120-125). Surgical reattachment of these two dissimilar biological materials therefore often fails. For example, failure rates for rotator cuff repair (which requires tendon-to-bone healing) have been reported to range between 20% for repair of small tears to 94% for repair of massive tears (126, 127). Similarly, outcomes after anterior cruciate reconstruction (which also depend on tendon-to-bone healing) are poor (128, 129). Studies in rotator cuff and anterior cruciate ligament animal models indicate that poor healing is due to the lack of regeneration of a specialized tissue to connect tendon and bone (124, 130-134). Engineering a replacement tissue for the enthesis or to develop treatments for tendon-to-bone healing requires understanding of structure-function relationships at the natural interface between tendon and bone.

2.6.2 Graded Morphology of the Tendon-to-Bone Insertion

While numerous types of insertions exist between tendon and bone, the most common anatomy is of tendon inserting into bone across a fibrocartilaginous transition (135, 136). This form of attachment has commonly been categorized into four zones (135). The first zone consists of tendon proper, and has properties similar to those found at the tendon mid-substance. This zone consists of well aligned type I collagen fibrils with small amounts of the proteoglycan decorin (117, 137). The second zone consists of fibrocartilage and marks the beginning of the transition from tendinous material to bony material. This zone is composed of types II and III collagen, with small amounts of types I, IX, and X collagen, and small amounts of the proteoglycans aggrecan and decorin (137-141). The third zone contains mineralized fibrocartilage, indicating a marked transition towards bony tissue. Here, the predominant collagen is type II, and there are significant amounts of type X collagen as well as aggrecan (138-142). Finally, zone four consists of bone, which is made up predominantly of type I collagen with a relatively high mineral content. Recent studies indicate that there are no sharp boundaries between the different 'zones' (143). Rather, a gradation exists in structure and composition between tendon and bone. This continuous change in tissue composition from tendon to bone is presumed to aid in the efficient transfer of load between the two materials.

2.6.3 Structure and Function of the Tendon-to-Bone Insertion

The tendon-to-bone insertion is biomechanically, compositionally, and structurally complex. The four discrete types of tissue recognized under the optical microscope are tendon, fibrocartilage, mineralized fibrocartilage, and bone (136). Between the unmineralized and mineralized fibrocartilage is a narrow zone that darkens markedly during tissue staining. This line was traditionally thought to represent a mineralization front, or mechanically, a boundary between soft and hard tissue (136). Supraspinatus tendon-to-bone insertions from rats were used to evaluate the gene expression, collagen organization, mineral content, and biomechanical properties of the insertion (138, 143). Assays were performed at various points along the transition zone. For gene expression, in situ hybridization was performed for extracellular matrix genes. The normal insertion site appeared as a fibrocartilaginous transition zone between tendon and bone as shown in Figure 2.20. Collagen fibril orientation sections were viewed under polarized light and angular deviation was calculated. Collagen fibres were less oriented at the insertion compared to the tendon (144). The mineral along the insertion was examined using individual Raman microprobe analyses with an approximately linear increase of relative mineral concentration vs. distance across the insertion site observed (Figure 2.21). Specimens were tested in tension to determine their biomechanical properties and the enthesis was significantly stiffer at the tendon end compared to the bony end. Based on these results, it is apparent that the tendon-to-bone insertion

site varies dramatically along its length in collagen structure, extracellular matrix composition, mineral content, geometry, and viscoelastic properties. This gradation in properties likely distributes forces more effectively across the transition from a flexible (i.e., tendon) to a rigid (i.e., bone) material.

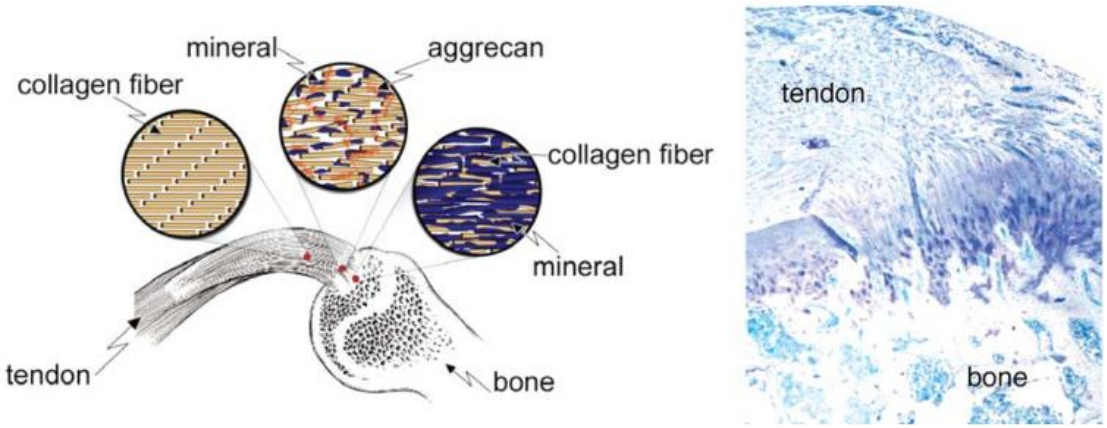

Figure 2.20 Morphology of the supraspinatus tendon-to-bone insertion site.

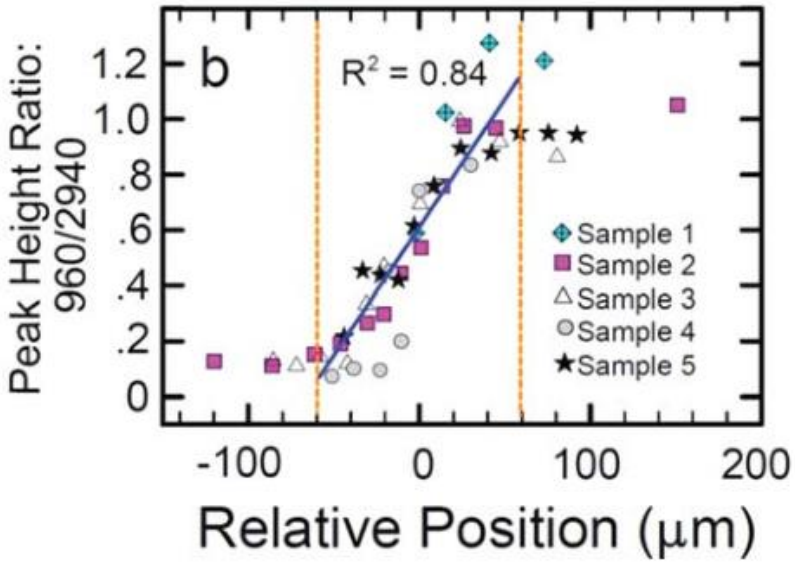

Figure 2.21 Plot of the ratio of mineral to collagen, shown as the peak height of mineral apatite [960 Δcm^{-1}] to collagen [2940 Δcm^{-1}] evaluated by Raman spectroscopy across the tendon-to-bone insertion of the rotator cuff (143, 144).

A finite element model of the tendon-to-bone insertion was generated to examine structure-function relationships at the insertion (145). It was hypothesized that the microscopic structure of the insertion measured experimentally is optimized to minimize stress and strain concentrations associated with load transfer from the relatively compliant tendon to the relatively rigid bone. To explore this, collagen fibre orientation distributions were used to derive material properties for a two-dimensional mechanical model of an insertion. Comparison between stress concentrations in an idealized model and those in three comparison models showed that the microstructure serves to 1) simultaneously reduce stress concentrations and material mass, and 2) shield the insertion's outward splay from the highest stresses.

The effect of mineral content on load transfer was modelled at the insertion (146). Mineral content and collagen fibre orientation was suggested as combining to give the tendon-to-bone transition a unique grading in mechanical properties. Results supported a new organ-level physiological model of continuous tissue transition from tendon to bone where the linear increase in mineral accumulation within collagen fibres moving from tendon to bone provides significant stiffening of the partially mineralized fibres as shown in Figure 2.21, but only for concentrations of mineral above a 'percolation threshold' corresponding to formation of a mechanically continuous mineral network in Figure 2.22. Increasing dispersion in the orientation distribution of collagen fibres from tendon to bone is a second major determinant of tissue stiffness. The combination of these two factors results in the nonmonotonic variation of stiffness over the length of the tendon-to-bone insertion,

and describes how tendon-to-bone attachment is achieved in nature through a functionally graded material composition. These experimental and modelling results provide a nano- and micro-mechanical understanding of collagen and mineral combinations to achieve the grading of material properties that is necessary for tissue engineered tendon-to-bone grafts.

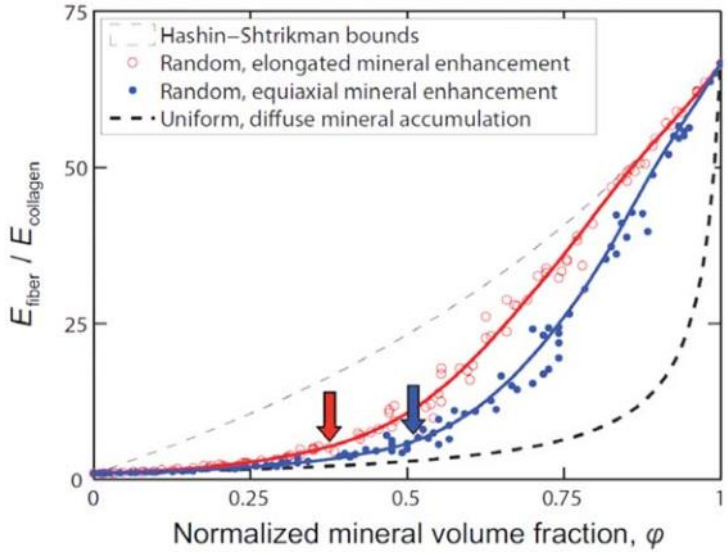

Figure 2.22 Bounds (lines) and Monte Carlo estimates (circles) for the elastic modulus (E) of collagen fibrils containing mineral deposits up to the level of mineralization found in bone. The stiffening of collagen fibrils by mineral increases dramatically above a critical mineral concentration called the 'percolation threshold' (arrows). This concentration is a function of the shape and distribution of mineral (red: aspect ratio of 1:1; blue: aspect ratio of 2:1) (144, 147).

2.7 Summary

This chapter gives a broad overview of fundamental composite theories, focusing on the critical role of interfaces in defining composite mechanical performance. Many

biological materials can be considered as fibre-reinforced or laminate composites on which the composite theory can be applied. The formation and constituents of different biological composites are discussed in detail in this chapter. All the biological materials studied in this thesis can be considered as composites and their structures and mechanical properties are reviewed respectively. A general lack of information of the microscale or nanoscale interfaces in these biological composites and their resultant contribution to the overall mechanical mechanics are highlighted. Therefore, understanding these biological interfaces at small length scales would be a significant contribution to understanding complex biological composite mechanics.

Chapter 3 - Methodologies

3.1 Introduction

This chapter provides an overview of the methodologies applied throughout the thesis. As the biological materials studied in the thesis are considered as laminate or fibre-reinforced biological composites at the microscale or nanoscale, specific experimental techniques are required to both prepare and mechanically characterize biological samples at small length scales. The approach taken here is to exploit preparation methods that isolate a specific structural feature in a complex biological material so that further mechanical testing can be used to evaluate the mechanical performance, and thus the importance of the feature, with respect to the larger scale biological structure. Therefore, novel techniques combining focused ion beam (FIB) for small length scale sample preparation, scanning electron microscopy (SEM) for in situ imaging and an custom built in situ atomic force microscopy (AFM) for mechanical testing are extensively employed, with these techniques described in detail in this chapter before applications in subsequent experimental chapters.

3.2 SEM Imaging

Scanning electron microscopy, first developed in the 1940s, is a technique that uses electrons focused onto the surface of a sample to produce a two-dimensional image (148). SEM is typically used where higher resolution imaging of materials is required beyond optical microscopy. The standard setup of a typical SEM is shown in Figure 3.1. The SEM used throughout the studies in the thesis is combined with a FIB system to give what is commonly referred to as a dual-beam microscope (Quanta 3D FEG, FEI, USA/EU). The SEM operates as any standard electron imaging system and uses a field emission gun (FEG) as the electron source for high resolution SEM imaging, in this case down to <1 nm. The electrons from the FEG are accelerated onto the surface of the sample and three condenser lenses focus the electron beam to a diameter of the order of 1 nm.

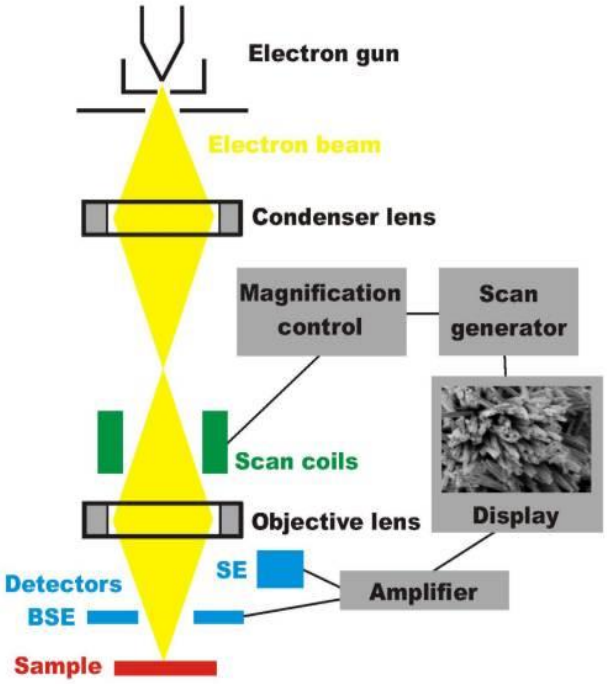

Figure 3.1 Schematic representation of a typical scanning electron microscopy (149).

Interaction of the primary electron beam with a sample produce a number of complementary electrons, including secondary electrons (SE) due to the primary beam knocking electrons from the shells of the sample atoms and backscattered electrons (BSE) that are primary electrons deflected by the nuclei of sample atoms. Both SE and BSE are scattered from the surface and sub-surface of the sample during raster-scanning of the primary electron beam and are counted by detectors. The number of electrons detected at each position of the primary beam on the surface of the sample produces a resultant 2D image. The most common electron detector is an Eberhart-Thornley detector, which is a scintillator-photomultiplier sitting at the side of the specimen chamber inside SEM. Eberhart-Thornley detectors operate by attaching scattered low energy secondary electrons to the small positive voltage (+250 V) on the screen of the detector. Secondary electrons pass the screen and are accelerated to impact the scintillator in order to cause light emission, which is then detected by a photo-multiplier (148). The acceleration voltages in this setup range from 0.2 - 30 kV with currents up to 200 nA.

The collection of BSE using a detector is schematically shown in Figure 3.2. Backscattered electron detector imaging is also used in this thesis as it provides decent contrast between different materials. Image contrast using BSE is particularly useful and is given by the number of BSE produced, which is dependent on the atomic number of the elements in the specimen (148). Therefore, elements of higher atomic numbers scatter a relatively large number of backscattered electrons, resulting in a brighter image area, whereas elements of lower atom numbers scatter

a relatively small number of backscattered electrons, resulting in a darker image area.

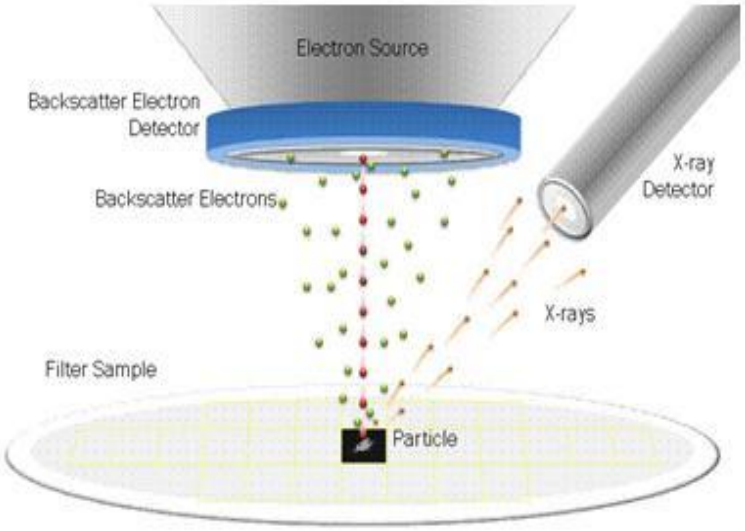

Figure 3.2 Schematic of a typical backscattered electron detector (150).

The production and scattering of electrons typically require a vacuum environment so that electrons do not scatter off air molecules. Thus, samples have to be mounted inside a vacuum chamber. The SEM-FIB dual-beam system used throughout this thesis allows for the vacuum chamber to be adjusted to different states. The two states applied in this thesis are high vacuum (HV) and low vacuum (LV) with vacuum pressures of 5.25×10^{-4} Pa and 120 Pa respectively. SEM technique has been widely used for the study of biological materials and the wide range of hierarchal structures they possess (151-154). Although there is controversy on the possible damage the electron beam and the vacuum environment might cause on biological samples (153, 155, 156), SEM is extensively used as a suitable method for imaging biological materials at small length scales due to the high spatial resolution and flexibility of the technique.

3.3 Sample Preparation Using FIB

The aim of sample preparation using FIB described in this section is to produce biological samples with volumes suitable for investigating their mechanical properties at the microscale or nanoscale. The capability of FIB to be used as a milling tool of producing small length scale samples for mechanical testing has already attracted increasing attentions in the study of synthetic materials (157, 158). FIB has also been proved suitable for site-specific milling of subsurface structures of biological samples in order to select a specific region for conventional electron microscopy examination (159). The capability of FIB to produce small discrete volumes of samples is particularly important for understanding the microscale or nanoscale mechanical properties of structural biological composites, which is impossible to achieve at large length scales where the shape and geometry of the sample in addition to the inherent material properties together define the overall mechanical properties of the material.

Pioneering works reporting on the use of ion beams to modify and remove materials from a sample were found in the 1970s, notably from the literature of Abrahams et al. (160). This work used argon cations to thin samples of GaAs for inspection using transmission electron microscopy (TEM) and was found to produce damage to the sample. Improvements in producing ion beams that caused less sample damage and focused to sub-microscale beam diameters were achieved by using gallium ions

(161). A schematic showing the focusing of gallium ions is present below in Figure 3.3a and a modern SEM-FIB dual-beam system is shown in Figure 3.3b.

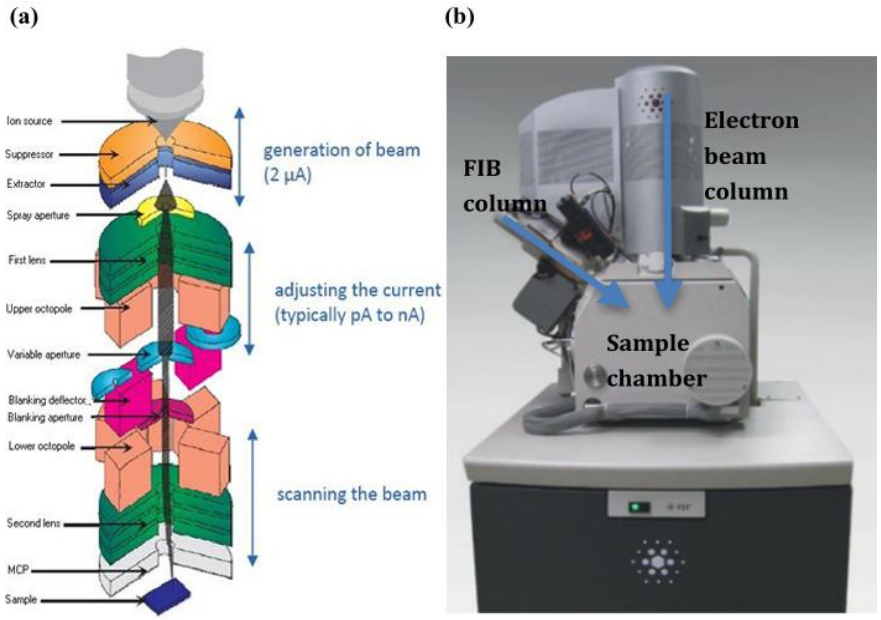

Figure 3.3 (a) Schematic diagram of a FIB ion column (161). (b) A modern dual-beam instrument combining an electron column, for SEM, and an FIB column.

The preparation of biological materials for mechanical testing using FIB is fairly uncommon in the literature. Perhaps the first example is the use of FIB to prepare triangular cross-section beams of tooth enamel for subsequent bending to failure experiments (11). The sample preparation in this work of Chan et al. (11) is shown in Figure 3.4 and indicates a beam with length of approximately 10 µm and width of 2 µm. The dimensions of the FIB-fabricated beam shown in Figure 3.4 are of great interest as they approach, or even exceed, the dimensions required to study the microscale or nanoscale biological structures in this work. Therefore, in principle, FIB can be used to isolate discrete volumes suitable for understanding the sub-microscale mechanical behaviour of biological composites.

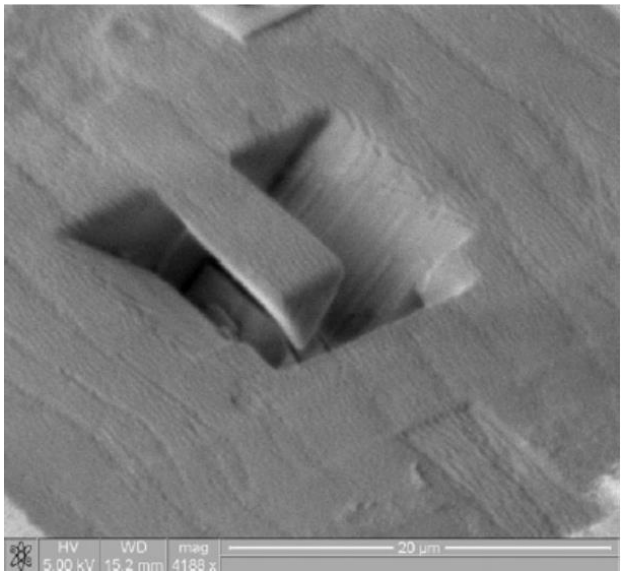

Figure 3.4 FIB preparation of cantilever micro-beam with a triangular cross-section in human primary molar sliced sections (11).

More recent works have prepared more standard rectangular cross-section beams for the study of limpet teeth and bone samples as shown in Figure 3.5 (155, 162). Rectangular cross-section beams are considered suitable for studying mechanical properties of biological materials at small length scales, especially as conventional continuum mechanical descriptions exist to describe bending experiments on such beams.

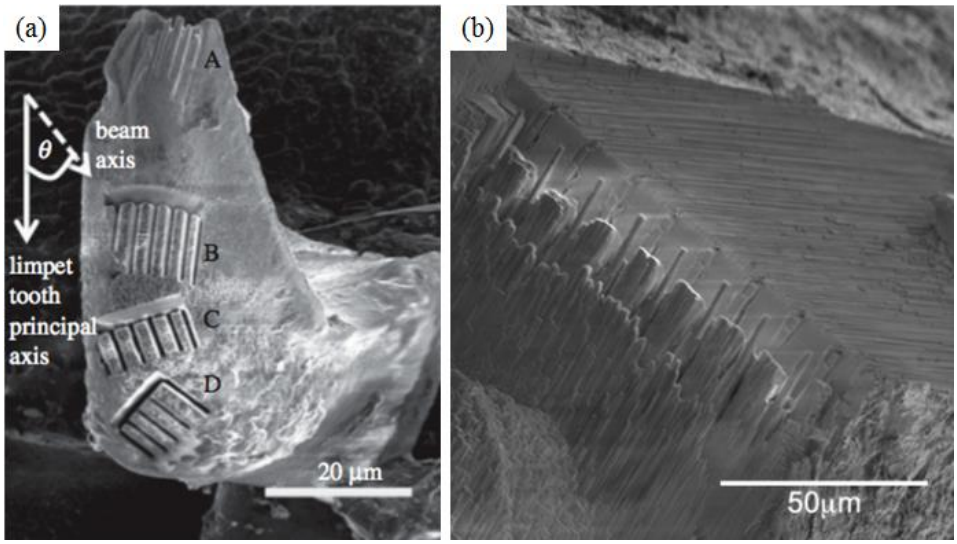

Figure 3.5 FIB-fabricated micron-sized beams produced in (a) limpet teeth (162) and (b) bone samples (155).

The use of FIB to prepare biological samples and isolate discrete volumes from the bulk require a series of preparation steps, typically performed inside a SEM-FIB dual-beam system so that the SEM is able to image the progress of the sample preparation. SEM is located above the sample stage and FIB is located at a 52° angle to the vertical direction as shown schematically in Figure 3.6. The sample needs to be tilted 52° in order to align FIB to the sample and proceed to mill the sample with FIB orientation parallel to the target surface of the sample. Indeed, the parallel orientation of FIB to the surface of the sample is critical in order to prevent the implantation of gallium ions into the sample. An ion beam that is incident to the surface of a sample will cause ion implantation, potentially changing the mechanical properties of the sample. Two factors are critical to protecting the sample from defocused ions. The first one is to deposit a thin layer of metal coating on the surface of the sample to prevent ion charging and the second one is to orientate the FIB

direction parallel to the sample surface produced, thus minimizing gallium ion implantation (163).

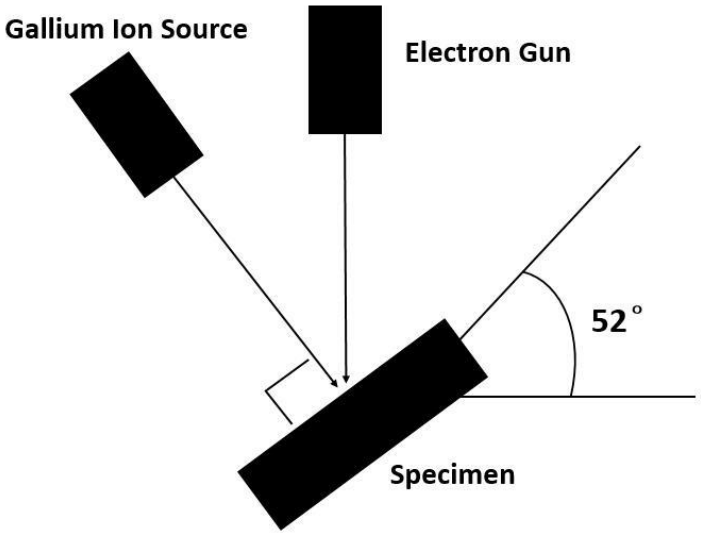

Figure 3.6 Schematic of the SEM-FIB dual-beam setup (Quanta 3D FEG, FEI, USA/EU). The SEM beam is above while the FIB is at a 52° angle (164).

Biological samples were prepared for FIB fabrication by first dehydrating the samples to remove water. Water within a sample is potentially problematic, as exposure of the sample to a partial vacuum will cause the water to evaporate rapidly, which may cause damage to the solid structure. Basically, biological samples were kept in ambient air environment for 2 hours before subsequent preparation using SEM and FIB, which had been proved to be sufficient to dehydrate the biological sample for SEM imaging and FIB fabrication (155). Biological samples were then gold coated for 45 seconds to improve their electrical conduction and fixed to the SEM sample stage using carbon tape in the SEM-FIB dual-beam system. The following describes an example of the FIB fabrication work on nacre by a succession

of processes summarized in Figure 3.7. FIB fabrication on other biological materials follows similar procedures with potential differences.

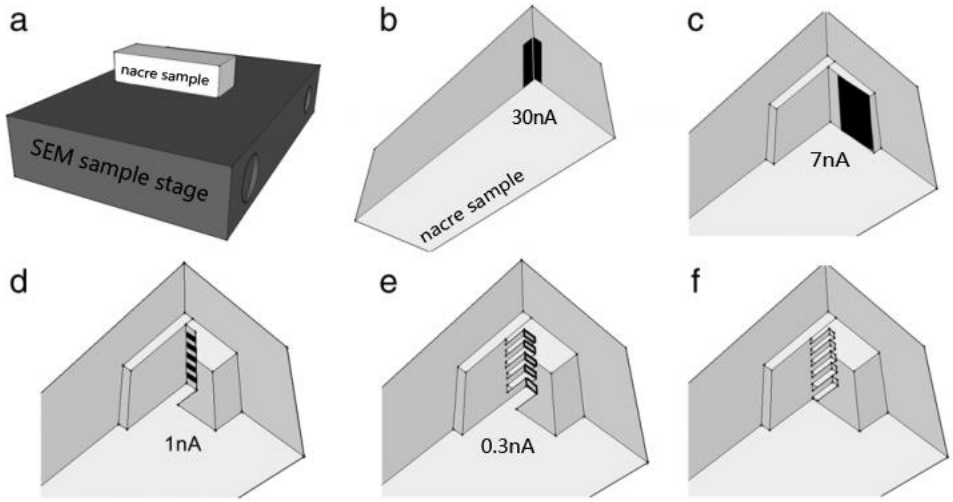

Figure3.7 Schematic of the FIB milling process (155). The black rectangles mark the FIB-fabricated area. (a) Nacre sample mounted on the SEM sample stage, (b) initial edge polishing using a current of 30 nA, (c) separation of bulk material from edge using 7 nA, (d) isolation of beams using 1 nA, (e) fine cutting and shaping of beams using 0.3 nA, (f) finalized sample showing 5 parallel beams. All cuts were performed with an acceleration voltage of 30 kV.

FIB was used to remove material from the biological structure in order to create discrete volumes by first polishing the edge of the sample using a high current ion beam of 30 nA and accelerating voltage of 30 kV as summarized in Table 3.1. Flattening of the sample edges allowed further removal of smaller volumes using smaller ion beam currents down to 0.3 nA. These smaller ion beam currents were used to minimize ion beam damage to the biological sample. Finally, materials were removed from the parent sample so that beams with dimensions of approximately 10 × 2 × 2 μm were created for mechanical testing as shown in Figure 3.8.

Table 3.1 Ion currents used in FIB to produce micron-sized beams suitable for mechanical testing. The steps are chronological from top (high current) to bottom (low current).

Current (nA)	Dimension (μm)	Time (min)
30	100 × 20 × 2	40 ± 10
30	100 × 20 × 2	40 ± 10
7	100 × 10 × 1	30 ± 5
1	5 × 10 × 1	20 ± 5
0.3	Polish around the beam	15 ± 5

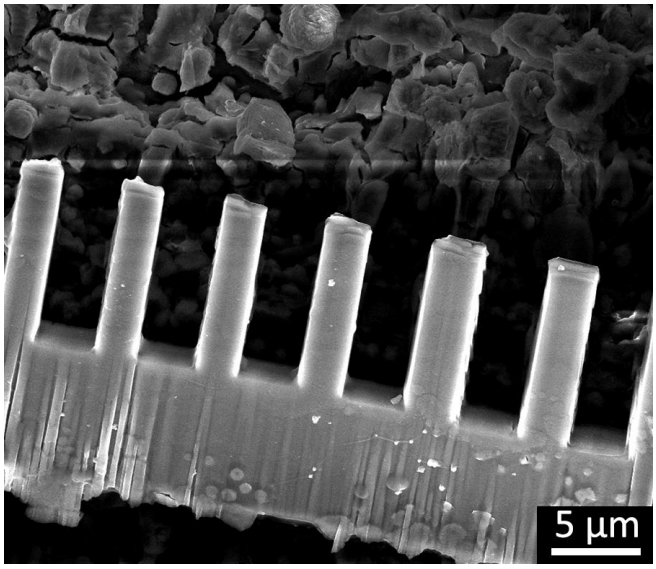

Figure 3.8 SEM micrograph showing a series of FIB-fabricated micron-sized nacre beams.

3.4 AFM Mechanical Testing

3.4.1 Introduction

Rapid advances in nanotechnology and growth in synthetic nanomaterial manufacture have brought significant requirements for mechanical characterization

of materials at small length scales. A wide range of biological materials can be considered as fibre-reinforced or laminate composites with different hierarchical structures that provide optimized mechanical properties. Current challenges exist in relating the microscale or nanoscale biological components to their overall mechanical properties at larger length scales. Investigating the mechanical properties of biological components at small length scales is therefore critical in determining the overall mechanical properties of biological materials incorporating microscale or nanoscale components.

3.4.2 AFM Working Principle

In this work, mechanical testing of FIB-fabricated biological samples was performed using an AFM technique. AFM allows characterization and manipulation of small length scale samples and is an important technique for deforming samples at small loadings (165, 166). As FIB-fabricated biological samples have relatively small volumes, AFM has sufficient force resolution for mechanical testing on these samples (165). The AFM system involves an AFM cantilever with a sharp tip at the end attached to a set of piezo-electric ceramics, normally used to scan the topography of a sample surface. Historically, AFM has been used to produce 3D topographic reconstructions of sample surface by detecting the interaction between AFM tip and sample surface (167, 168). These interactions include Van der Waals forces, capillary forces, chemical bonding, electrostatic forces, magnetic forces, Casimir forces and solvation forces (169). Subsequent study has also shown the possibility of

measuring additional quantities simultaneously through the use of specialized AFM tips (169).

The interaction between an AFM tip moved into contact with a solid surface in most typical cases can be described by the Lennard-Jones potential (170), which is a mathematical model describing the interaction between two neutral atoms, molecules or surfaces as they approach each other. The Lennard-Jones potential can be best described by a graph of the interaction versus the distance as shown in Figure 3.9. The curve indicates the interaction between two objects across a range of distances. Two objects with a relatively large separation distance interact weakly but in attraction, indicated by a small negative interaction energy in Figure 3.9, which increases to an energy minimum. Decreasing the separation distance beyond the energy minima causes a less favourable interaction energy, defined as a negative gradient, and therefore repulsion.

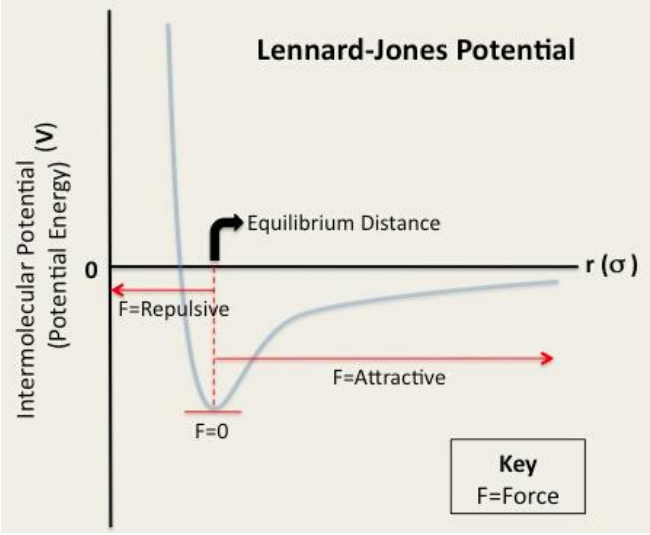

Figure 3.9 Lennard-Jones curve showing the interaction energy between two surfaces with separation r between the surfaces (171).

AFM for topography imaging uses the Lennard-Jones potential when an AFM tip is systematically scanned over a sample surface with piezoelectric positioners while monitoring the extent of tip-sample interactions. Changes in sample topography will cause changes in the interaction between the scanning tip and the surface. These changes can be related to surface topography so that, for example, a high feature on the surface will increase the interaction between the tip and the sample whereas a hole on the surface will decrease the tip-sample interaction as the sample surface is relatively far away from the AFM tip. An imaging AFM tip is able to measure the AFM tip-sample surface interactions by the cantilever system attached to the AFM tip so that repulsion and attraction cause corresponding bendings of the cantilever.

An optical system is additionally used to convert the AFM cantilever bending behaviour into measurable electrical signals. AFM imaging exploits a feedback system so that, during scanning of the AFM tip across the sample surface in an x-y plane, the tip-sample interaction is monitored and the AFM tip moved towards or away from the sample surface using a z-piezo positioner in order to maintain the AFM tip-sample interaction. Therefore, recording the piezo (x, y, z) co-ordinates during AFM tip scanning over the sample surface produces a topographic image of the sample. This mechanism can also be used to accurately measure forces when an AFM tip moves towards a sample into contact or away from a sample to perform a mechanical test rather than imaging. Forces acting between the AFM tip and sample surface will cause a corresponding deflection of the cantilever during approach or retraction of the AFM tip from the sample. According to Hooke's Law, the bending of an AFM cantilever can be converted to force by considering the spring constant k of

the cantilever, which is defined by both the elastic modulus of the cantilever material (silicon in this work) and the cantilever dimensions. A standard AFM technique calculates the spring constant of an AFM cantilever by the Sader calibration method involved in the AFM software package (Nova, NT-MDT, Russia) (172), which uses the plan area of the cantilever, the resonance frequency, the quality factor of the AFM cantilever and the density and viscosity of the fluid in which these factors are measured, in this case air (172, 173). These factors are then considered in the following equation:

$$k = 7.5246\rho_f w^2 L Q f_0{}^2 \Gamma_i(\mathrm{Re}) \qquad \text{Equation 3.1}$$

where

$$\mathrm{Re} = \frac{2\pi\rho_f f_0 w^2}{4\eta_f} \qquad \text{Equation 3.2}$$

where k is the spring constant, ρ_f is the density of the media around the AFM cantilever, w is the width of the cantilever, L is the length of the cantilever from the base to the apex, Q is the quality factor of the cantilever, f_0 is the resonance frequency of the cantilever, Γ is the imaginary component of the hydrodynamic function, which in turn is a function of the Reynolds number, *Re*, defined in Equation 3.2 using the viscosity of the fluid η_f. Both the quality factor of the cantilever and the resonance frequency are determined by performing a power spectral analysis of the cantilever's thermally driven oscillations. The resonance peak is fitted with the following harmonic model:

$$A = A_{white} + \frac{A_0 f_0{}^4}{(f^2 - f_0{}^2)^2 + (\frac{f \cdot f_0}{Q})^2} \qquad \text{Equation 3.3}$$

Where A_{white} is the white noise fit baseline and A_0 is the zero frequency amplitude. The four parameters are fitted using a least-squares method (173). Overall, the Sader method is accurate for calibration of AFM rectangular cantilevers and has been determined to have only ~4% uncertainty, with the cantilever width as the major source of error (173).

Deformation of a sample during contact or separation from an AFM tip is further required so as to determine the mechanical performance of the sample. A profile of the force acting on the AFM tip (with respect to the tip position relative to the sample) is required, known as a force-distance curve as shown in Figure 3.10. Two force-distance curves are required when evaluating the deformation behaviour of a sample when loading with an AFM tip. The first curve recorded is that of the AFM cantilever deflection as a contacting AFM tip is moved towards a rigid non-deformable surface, which is referred to as the calibration curve, shown in red in Figure 3.10. This curve shows that the z-piezo movement causes a corresponding deflection in the AFM cantilever. Therefore, the cantilever deflection measured using the AFM optical setup can be directly converted to a length displacement. The second curve in Figure 3.10 corresponds to an AFM tip moving towards and into a deformable sample surface, therefore producing a mechanical test on the sample and is referred to as the test curve, shown in blue in Figure 3.10.

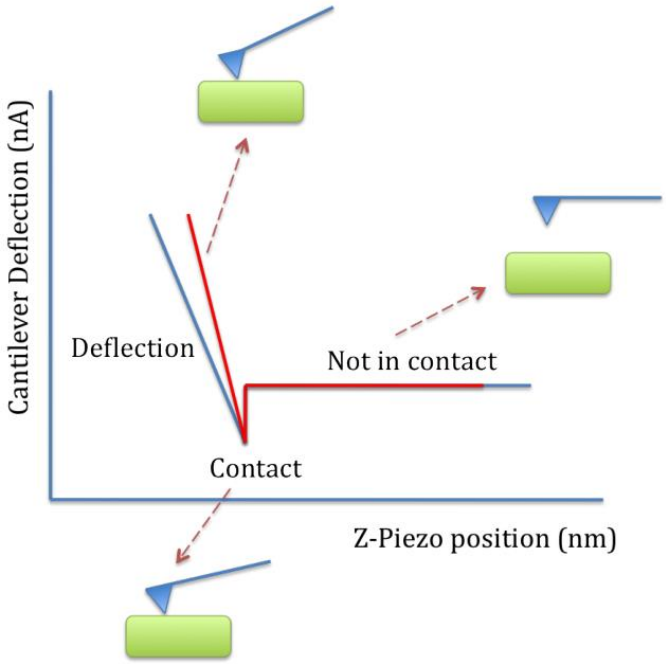

Figure 3.10 Schematic plot of AFM cantilever deflection against z-piezo position. The red line corresponds to the approach and contact of an AFM tip with a rigid non-deformable sample in order to carry out AFM cantilever deflection calibration. The blue line indicates approach and contact between an AFM tip and a deformable sample.

The displacement of the tip into the sample can be found by aassuming that the sample will behave as a deformable surface relative to a rigid surface. Considering an initial position of an AFM tip contacting a sample surface with zero force, further extension of the z-piezo (Z_0) will cause the AFM tip to move into the sample by a distance D_0 and a resultant applied force causing a deflection of the cantilever C_0 such that: $Z_0 = D_0 + C_0$.

The force applied by the AFM tip to the sample is measured from the deflection of the AFM cantilever to give:

$$F = kd \qquad \text{Equation 3.4}$$

Where F is the force applied by the AFM tip, k is the AFM cantilever spring constant and d is the deflection of the AFM cantilever under the applied force F in the calibration curve. The force applied by the AFM tip to the sample therefore depends on the spring constant of the AFM cantilever being used and the displacement of the AFM cantilever.

3.4.3 SEM-AFM Setup for Mechanical Testing

A novel in situ nanomechanical AFM testing methodology is employed in this thesis and applied to FIB-fabricated biological samples by incorporating the mechanical testing capability of a custom built AFM system (Attocube System AG, Germany) with the imaging capability of the high resolution SEM (Quanta 3D FEG, FEI, USA/EU) in the SEM-FIB dual-beam microscopy system as shown optically in Figure 3.11. Sample gripping and manipulation are achieved using accurate AFM piezoelectric ceramic positioners while mechanical testing experiments continually record cantilever deflection at high force resolution using AFM force spectroscopy. This configuration allows accurate force-deflection signals to be recorded during mechanical testing and a wide range of mechanical properties to be achieved.

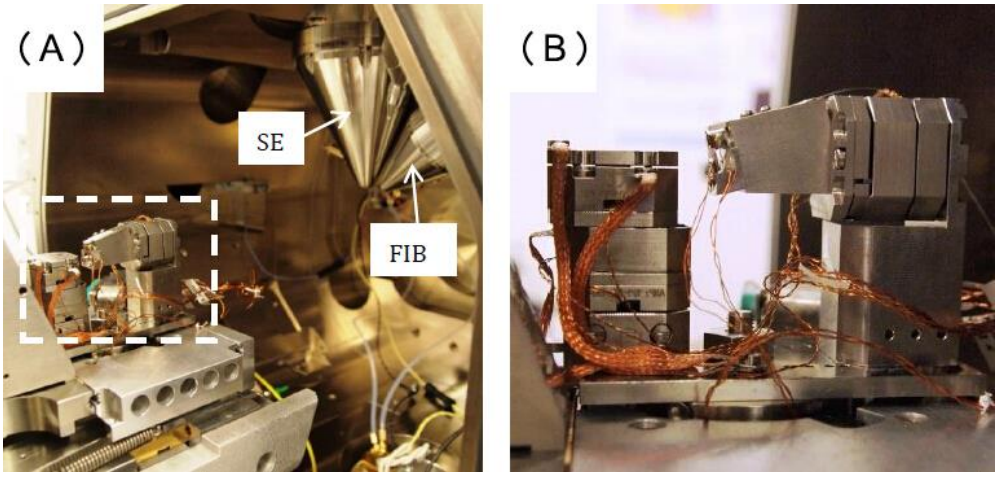

Figure 3.11 (A) Optical photograph showing AFM fitted on SEM sample stage when the door of SEM chamber is open. Dashed rectangle indicates location of the AFM. Secondary electron (SE) axis and focused ion beam (FIB) axis are also labelled. (B) Higher magnification optical side view image of the AFM on the SEM sample stage.

This novel SEM-AFM mechanical testing system has the capability for general mechanical testing including bending, tensile, buckling and peeling tests (154, 155, 174-176). The Attocube AFM sits horizontally in the SEM chamber to allow electron beam access to the sample, as shown schematically in Figure 3.12, with AFM control and data acquisition obtained using vacuum feed-through points in the SEM chamber. Both the sample stage and the AFM head could move in three dimensional directions to allow accurate location of particular regions in the sample using SEM.

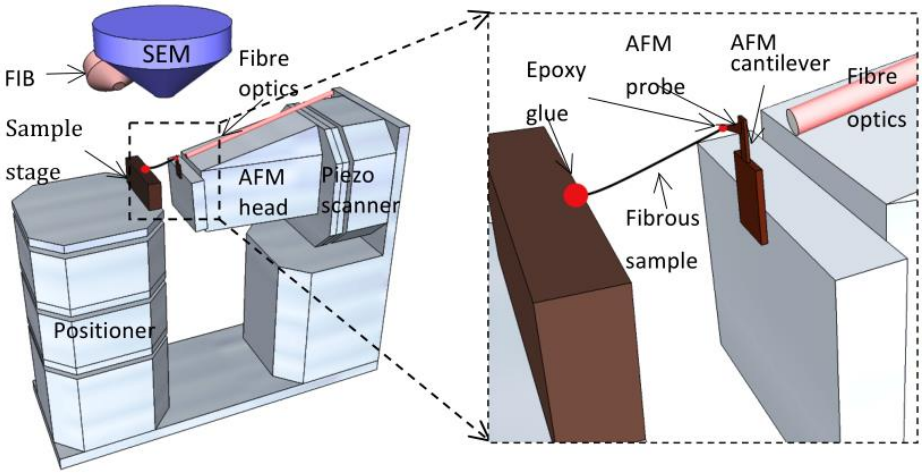

Figure 3.12 Schematic diagram showing the in situ SEM-AFM configuration. The insert shows fixing of a nanofibre with glue between the substrate and AFM cantilever (154).

An optical interferometry is used in the Attocube AFM system to record the AFM cantilever deflection during mechanical testing. Interference is the superposition of two or more waves which results in a new wave pattern. Interference usually refers to the interaction of waves that are correlated or coherent with each other, either because they come from the same source or because they have the same or nearly the same frequency. If there is a fixed phase relation between two waves, interference is confirmed to either constructive or destructive as shown in Figure 3.13. Consider two waves that are in phase, with amplitudes A_1 and A_2. Their troughs and peaks line up and the resultant wave will have amplitude $A = A_1 + A_2$. This is known as constructive interference. If the two waves are π radians, or 180°, out of phase, then one wave's crests will coincide with another wave's troughs and they will tend to cancel out. The resultant amplitude is $A = |A_1 - A_2|$. If $A_1 = A_2$, the resultant amplitude will be zero. This is known as destructive interference.

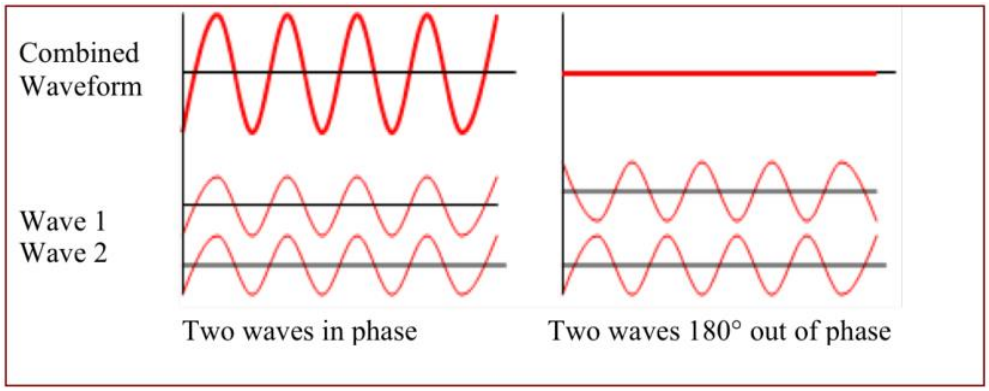

Figure 3.13 Constructive and deconstructive interference of two waves.

In the Attocube AFM system, two reflected laser beams with high monochromaticity are generated by two pivotal reflecting surfaces, which make interference possible. These two surfaces are schematically shown in Figure 3.14. The reflection of the original laser signal at the end surface of the detecting optic fibre and the back of the AFM cantilever produces two resulting reflected laser signals, which forms the detectable signal of the interferometer. A force applied to the AFM tip will therefore produce a corresponding cantilever deflection and interaction between the reflected laser signals. As cantilever deflects, the distance between the AFM cantilever and the optic fibre end changes, with an example of force applied to the AFM tip. The reflected laser from the back of the cantilever will travel a correspondingly different path length resulting in progressively different interference between the two reflected laser light wavelengths. Thus, corresponding change in the interference signal from the combination of the two reflected wavelengths is indicative of the AFM cantilever bending and the resultant force acting on the AFM tip.

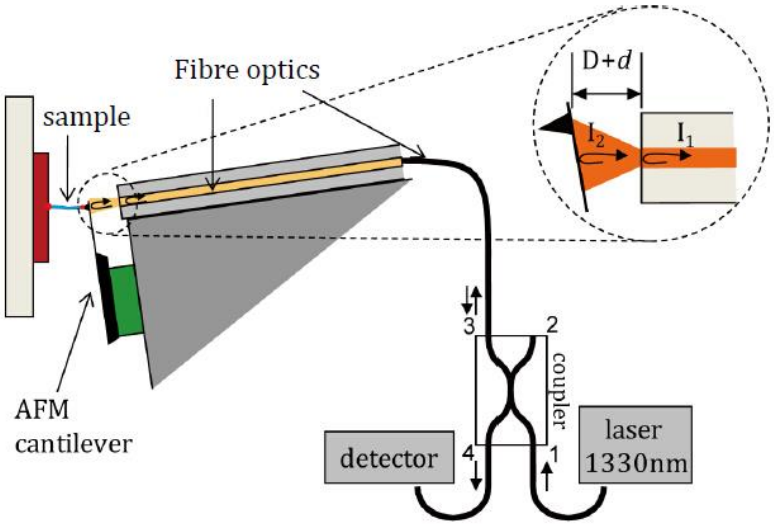

Figure 3.14 Schematic diagram of the laser interferometer used in the AFM illustrating the interference signal measured. Approximately 4% of the laser light is reflected at the glass-air interface with an intensity of I_1 while 96% of the light is transmitted and partially reflected at the AFM cantilever with an intensity of I_2. The intensity I_2 depends on the reflectivity of the AFM cantilever.

The force spectroscopy measurement using the Attocube AFM is driven as a similar way as conventional AFM described above. Two piezoelectric ceramic positioners are involved: the z-piezo and dither piezo. A dither piezo is used to set up the initial distance between the AFM tip and the optic fibre end. In force spectroscopy, the z-piezo expands in order to move the AFM tip towards the sample. With continuous expansion of the z-piezo after contact with the sample, the AFM tip causes a change in the gap between the optic fibre end and the AFM cantilever. If the z-piezo movement is continual, the total intensity change of the two interfered reflected laser beams collected by the optic fibre will follow sinusoidal behaviour, indicative of an interferometer curve as shown in Figure 3.15. Contact between the AFM tip and the sample is shown as a start of the sinusoidal signal response which progresses as the cantilever deflects further, causing corresponding destructive and

constructive interference between the two reflected laser light pathways. The progression of the sinusoidal signal is indicative of increasing force acting between the AFM tip and the sample.

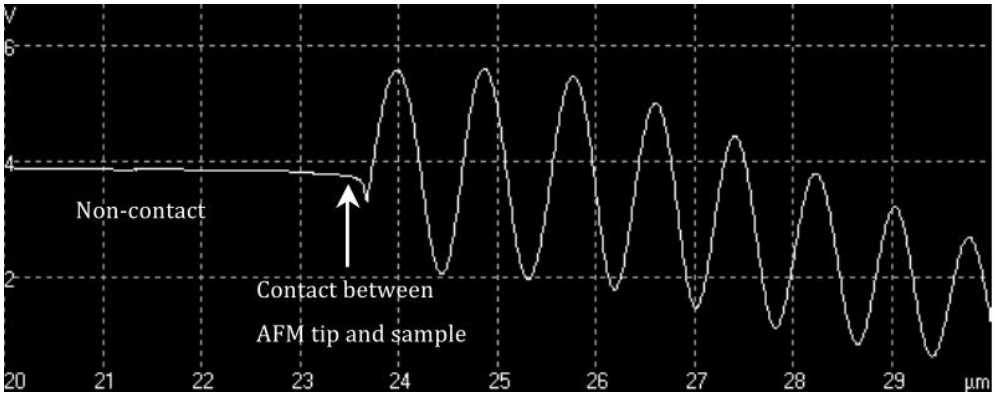

Figure 3.15 Detected laser signal during force spectroscopy (y-axis) as the z-piezo expands from left to right on the x-axis. Contact between the AFM tip and the sample causes a deflection of the AFM cantilever and a corresponding change in the collected laser intensity.

3.4.4 AFM Data Analysis

The capability of the Attocube AFM to record force during force spectroscopy can be used to measure the mechanical quantities of stress and strain applied to a sample by the end of an AFM tip. For tensile testing, the tensile stress applied to the sample can be calculated using Hooke's Law:

$$\sigma = \frac{F}{A} = \frac{kd}{A} \qquad \text{Equation 3.5}$$

where F is the force applied on the sample, k is the spring constant of the cantilever, d is the cantilever deflection and A is the cross-sectional area of the sample.

When the cantilever is translated away from the sample stage, the retraction distance of piezo scanner *X* behind the cantilever is recorded by AFM. This translation causes the AFM cantilever deflection and the deformation of the sample. The retraction distance *X* is therefore equal to the sum of the cantilever bending deflection *d* and the sample deformation *ΔL*. Hence, the sample strain δ can be calculated using:

$$\delta = \frac{\Delta L}{L} = \frac{X - d}{L} \qquad \text{Equation 3.6}$$

where *ΔL* is the elongation of the sample, *L* is the original length of the sample taken from SEM images at the start of tensile testing and *X* is the retraction distance of the piezo scanner.

Equations 3.5 and 3.6 indicate that determination of AFM cantilever bending is required to measure both the stress and strain behaviour of the sample during mechanical testing. The mechanical deformation of the sample shown in Figure 3.16 clearly indicates a sinusoidal variation in the collected laser intensity as the cantilever deflects during z-piezo scanner translation. The collected laser intensity is defined by the intensity of incident lights I_1 and I_2 as well as the optical path length difference between the two, defined as $2(D + d)$ as shown in Figure 3.14:

$$I_0 = f(z) = I_1 + I_2 + 2\sqrt{I_1 I_2}\cos[\frac{2\pi}{\lambda} \times 2(D + d)] \qquad \text{Equation 3.7}$$

where I_0 is the reflected laser intensity, I_1 and I_2 are the reflected laser intensities, *D* is the initial cantilever-fibre optic distance and $(D + d)$ is the cantilever-optic fibre distance as the tensile test proceeds. λ is the wavelength of the laser (1330 nm) used

in the laser interferometer setup. The cantilever bending *d* is therefore calculated from:

$$d = \arccos \frac{I_0 - I_1 - I_2}{2\sqrt{I_1 I_2}} \frac{\lambda}{4\pi} - D \qquad \text{Equation 3.8}$$

Equation 3.8 can therefore be applied to the collected laser intensity data to determine the cantilever bending. The force sensitivity of each test is evaluated by defining the resolution of data collection in the sinusoidal intensity-displacement curve. The laser intensity changing between two adjacent data points could be converted to the minimum displacement recorded in the test by Equation 3.8. The force resolution can then be calculated from the minimum displacement of the cantilever recorded combined with the spring constant of the selected AFM cantilever, and typically gives a force resolution of (5.4 ± 0.8) × 10^{-4} μN using AFM cantilevers with relatively small spring constants of approximately 1 N·m^{-1}.

3.5 Summary

This chapter details the main experimental methodologies used throughout this thesis to produce discrete volumes of biological samples at the microscale or nanoscale using FIB microscope in the SEM-FIB dual-beam system. Further mechanical testing techniques based on the custom built in situ AFM system within the SEM-FIB dual-beam system are described to show how to apply accurate small forces to small length scale objects and ultimately, perform a variety of mechanical tests on FIB-fabricated biological samples at the sub-microscale. These methodologies will be repeatedly referred to in the following experimental chapters.

Chapter 4 - Influence of SEM Vacuum on the Mechanical Properties of Nacre

4.1 Introduction

Nacre, along with many other biological composites, is physiologically in a hydrated state (73, 92, 177-180). Therefore, the mechanical performance of these biological materials is partly dependent on the level of hydration of the material. However, evaluating the structure-mechanical relationships of biological materials at small length scales using techniques that potentially introduce vacuum environments, such as SEM and FIB microscopy detailed in Chapter 3, potentially compromise the measured mechanical properties (181, 182). Therefore, small deflection bending testing of FIB-fabricated nacre beams at the microscale under different environmental conditions are carried out in this chapter to evaluate the influence of SEM vacuum conditions on the mechanical properties of nacre, thereby validating the methodology applied in this thesis.

A wide range of investigations have been performed to study the mechanical properties of nacre under different hydration conditions (81, 85, 92, 183-186).

Figure 4.1 shows typical tensile and shear behaviour of nacre studies in the literature under dry (ambient conditions) and hydrated conditions (soaked in water), showing some ductility at the macroscale (92, 183). The tensile stress–strain curves are shown in Figure 4.1a; the behaviour of dry nacre is similar to that of pure aragonite and fails in a brittle fashion. The plot indicates that dehydrated nacre loses toughness, defined as the area under the stress-strain curve, with suggestions that the dehydration affects the small fraction (5 wt.%) of organic materials (5 wt.%) and highlighting the importance of the soft phase to overall nacre mechanics. Hydrated nacre shows an initial linear elastic response under loading, which is similar to dry nacre, but then exhibits plasticity with increasing strain starting at a stress of approximately 70 MPa. Plastic deformation in nacre is clearly observed when shearing the bulk (Figure 4.1b) but is less obvious in tension (Figure 4.1a) due to tablet interlocking causing more stress transfer to the hard phase. Jackson et al. (85) concluded that water affects the elastic modulus and tensile strength of nacre by reducing the shear modulus and shear strength of the organic matrix. Toughness is enhanced by water, which plasticizes the organic matrix, resulting in greater crack blunting and deflection abilities.

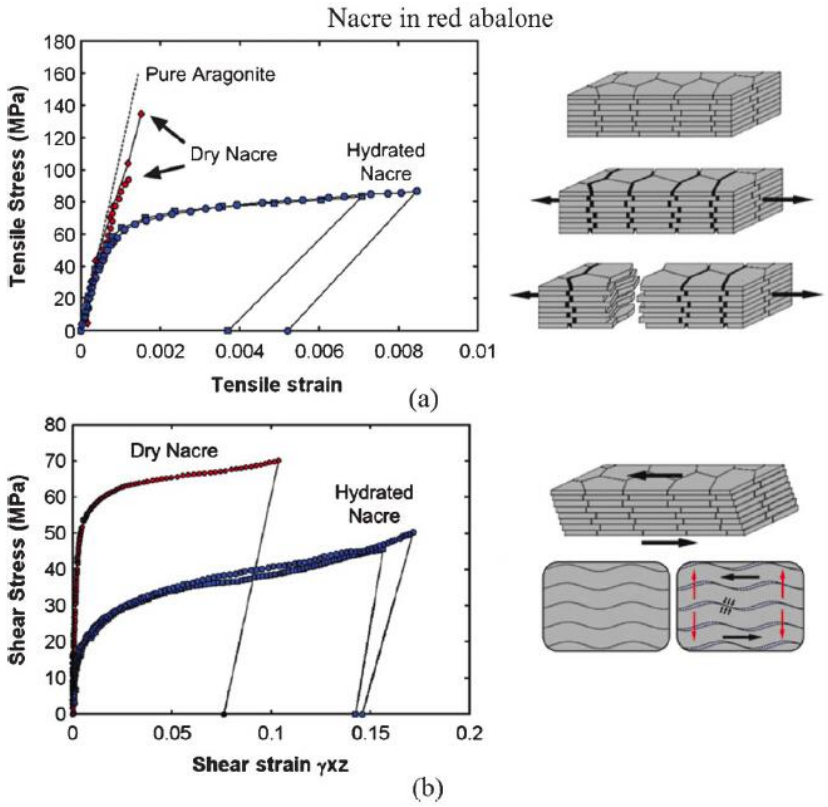

Figure 4.1 (a) Tensile and (b) shear stress–strain curves for nacre in red abalone and a schematic of lamellar tile structures showing associated deformation modes. Tablet waviness generates resistance to sliding, accompanied by lateral expansion (vertical arrows) (92, 183).

Micro-scratch tests and indentation tests were also performed on both dry and soaked surfaces of nacre from green mussel shells (184) to investigate the role of water content in the organic matrix and the scratch/nanoindentation hardness on the toughness mechanism. Both scratch and indentation experiments showed a decrease in hardness as a result of hydration. These results suggest that the toughness of nacre is affected by sample hydration. Further friction and wear behaviour of sheet nacre has been studied in dry and wet environments (185, 186). The coefficient of friction was found to be high under dry conditions (0.45) and increases further under wet conditions (0.78) (185). The environment was indicated

as influencing the wear mechanisms of nacre by means of various physicochemical interactions on the water-soluble 'intracrystalline' organic phase. Friction-induced damage mechanisms involving thermal effects remain poorly understood (186).

Previous investigations detailed above have examined the hydration of nacre and corresponding influence on the mechanical behaviour of nacre, yet so far little work has been done to examine the influence of vacuum environment on nacre properties. The vacuum environment is essential in many cases where electron or ion microscopy is employed, such as SEM and FIB microscopy applied in this work. The evaluation of nacre mechanics using techniques involving SEM, FIB and AFM has distinct advantages compared to previous works. Principally, observation and modification of relatively small volumes of nacre sample can be achieved in the SEM-FIB dual-beam system, with subsequent mechanical behaviour evaluated using the custom built AFM. Mechanical testing of nacre at small length scales is advantageous compared to that at larger length scales since the effect of structural hierarchies can be potentially ignored or simplified. Such methodology allows the study of nacre mechanics at small length scales rather than the whole nacre mechanical behaviour. The influence of SEM vacuum condition on potential structural and mechanical changes in nacre due to water removal, which is the main focus of this chapter, is therefore able to be evaluated. Previous works (154, 155) have used a SEM-FIB-AFM setup to mechanically test a variety of bone samples from the microscale to the nanoscale within SEM vacuum environments, showing that dehydration of bone in vacuum chamber does not have an effect on the mechanical properties of bone at sub-micron length scale. In this chapter, cantilever beam bending test was

performed on FIB-fabricated nacre beams under a range of environmental conditions to investigate the influence of vacuum on the mechanical properties of nacre. The results and discussion in this chapter will also validate the methodology performed in subsequent chapters on other biological composites, like arthropod exoskeleton and tendon-to-bone attachment.

4.2 Materials and Methods

4.2.1 Preliminary Sample Preparation

Nacre studied in this work was harvested from wild French abalone shells purchased from the Fish Society Company, London, UK. Wild French abalones (approximately 160 g each) were stored at -20°C in a freezer prior to dissection. Specimens were carefully dissected using a water-cooled rotating diamond saw (Struers Accutom-5). Structural motifs were examined using optical and electron microscopies as shown in Figure 4.2. Specifically, Figure 4.2b shows an SEM image of the cross section area of the nacreous layer, showing the structure of mesolayers with thickness of approximately 150 μm separated by thick organic layers with thickness of approximately 30 μm. SEM imaging also shows that the nacreous layer in abalone shell is columnar nacre where mineral tablets are stacked in columns with coinciding centres, as shown in Figure 4.2c. Higher magnification SEM image shown in Figure 4.2d reveals typical dimensions of the mineral tablet approximately 6.80 μm in width and 0.42 μm in thickness, measured by detailed pixel measurements (ImageJ, N.I.H., USA) with a dimensional measurement error smaller than 5%.

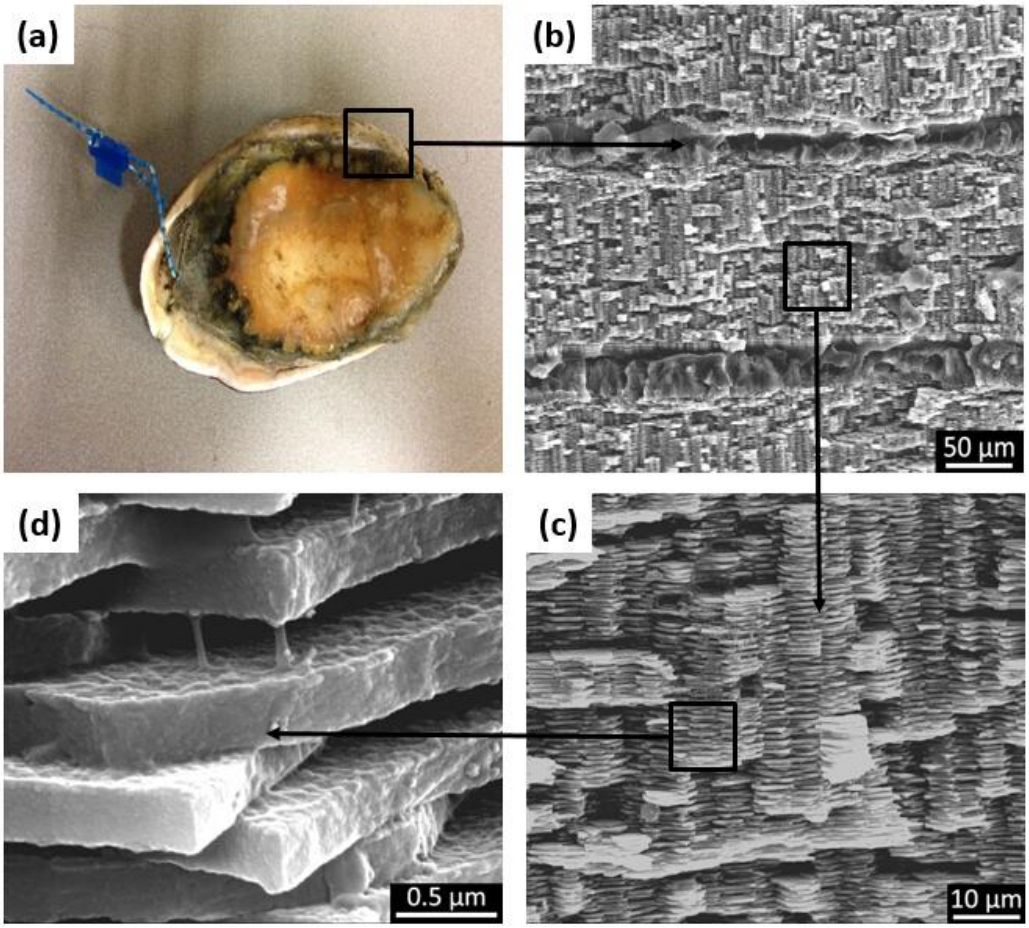

Figure 4.2 The hierarchical structure of nacre showing (a) optical image of whole French wild abalone studied in this work with SEM micrographs of the cross section of nacreous layer indicating (b) the structure of mesolayers within the cross section area of nacre sample, (c) typical 'brick and mortar' structural characteristic of the aragonite mineral tablets and the organic matrix and (d) higher resolution image showing organic material between the aragonite mineral tablets.

4.2.2 Sample Preparation Using FIB

Tensile test is regarded as the typical mechanical testing method in order to characterize a material but is practically difficult to perform at small length scales. Many researchers choose bending tests as a more suitable and practical method, primarily because careful gripping of small samples is normally not required in a

bending test (11, 155, 162). Therefore, cantilever beam bending test is applied herein to evaluate the influence of SEM vacuum environments on the mechanical properties of nacre. FIB technique is used to fabricate nacre samples suitable for mechanical testing at small length scales as described in section 3.3. Specifically, small pieces of nacre samples with dimensions of approximately 10 × 5 × 3 mm were first isolated from parent abalone shells using the water-cooled rotating diamond saw. Nacre samples were thoroughly rinsed and kept in distilled water at room temperature in order to keep samples clean and hydrated. Before FIB fabrication, samples were removed from distilled water and maintained in ambient air for 2 hours to dehydrate the nacre sufficiently for SEM imaging and FIB fabrication. Samples were subsequently sputter gold coated to avoid electron or ion charging effects that could interfere with FIB fabrication (155, 181), followed by placement into the SEM-FIB dual-beam system. Individual micron-sized nacre beams were created following the FIB fabrication procedure described in Section 3.3. Figure 4.3 shows typical FIB-fabricated nacre beams with dimensions of approximately 10 × 2 × 2 μm with the long axis of the beam parallel to the long axis of the mineral tablets. The beam was fabricated in this direction to make sure that the mineral tablets carry most of the load during the cantilever bending test rather than the weak organic interfaces if the beam was fabricated with the mineral tablet transverse to the long axis of the beam. The location of the beams was selected under SEM imaging to avoid the thick organic layers between mesolayers, making ensure that all nacre beams consist of the 'brick and mortar' structure.

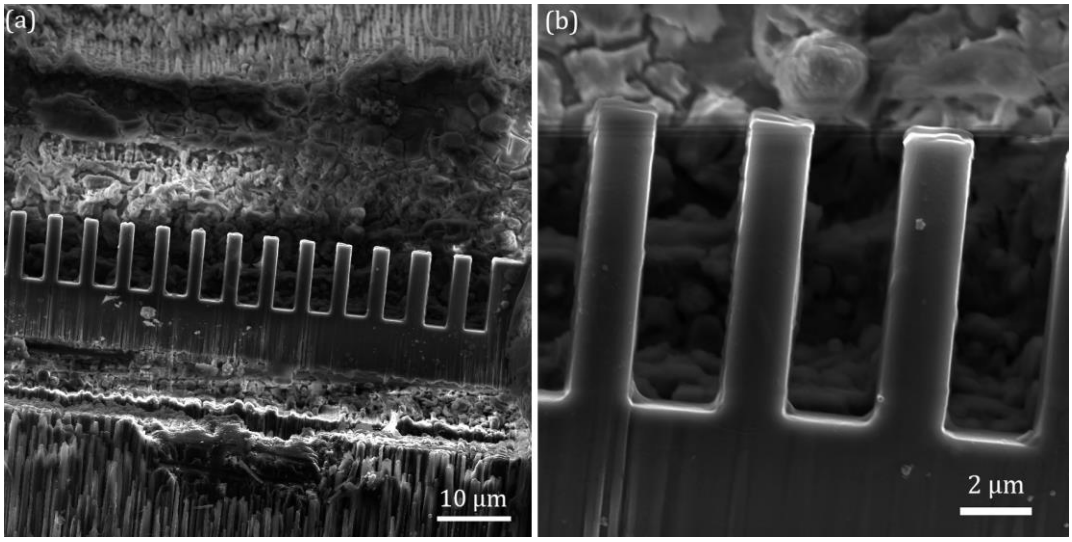

Figure 4.3 SEM micrographs showing a series of FIB-fabricated micron-sized nacre beams under a range of magnifications from low (left) to high (right), indicating the highly regular rectangular shapes produced.

After FIB fabrication, nacre samples were removed from the vacuum chamber of the SEM. Half of the samples were kept dry in ambient air environment as a control group and the other half were placed in an isolated vessel containing a beaker of distilled water with a high vapour concentration to allow sample rehydration. This rehydration method has been more effective than directly immersing FIB-fabricated samples into liquid solutions, which leads to the surface tension of liquid fracturing the relatively fragile FIB-fabricated samples (155). In order to assess the effectiveness of this rehydration process, the weights of five small nacre samples with dimensions of approximately 10 × 5 × 3 mm were measured following the same sample preparation process as described above. Table 4.1 records the weight loss measured for five samples subjected to various environmental conditions used in the sample preparation process and Figure 4.4 shows the weight change with time. Nacre samples were normally kept in distilled water for storage. Then samples were

removed from water and after removing excess surface water with filter paper, weighed using an electronic analytical microbalance (Sartorius, Germany) to four significant figures. The weights of these samples were taken as fully hydrated weight. Further preparation processes were recorded by the percentage of weight loss relatively to this fully hydrated nacre weight as shown in Table 4.1.

Table 4.1 Change in weight, as a percentage of the weight difference relative to hydrated nacre in distilled water. The cycle of hydration represented by the table was repeated on five different nacre sections.

Sample conditions	**Time (hours)**	**Weight loss compared to hydrated condition in distilled water (%)**
Stored in distilled water	Storage	0.000 ± 0.021
Dehydrated in ambient air	2	2.743 ± 0.115
Dehydrated in SEM vacuum (High vacuum 5.25×10^{-4} Pa)	2	3.961 ± 0.082
Rehydrated in high vapour concentration	4	0.035 ± 0.059
Dehydrated in SEM vacuum (High vacuum 5.25×10^{-4} Pa)	2	4.258 ± 0.091
Rehydrated in high vapour concentration	4	0.046 ± 0.035

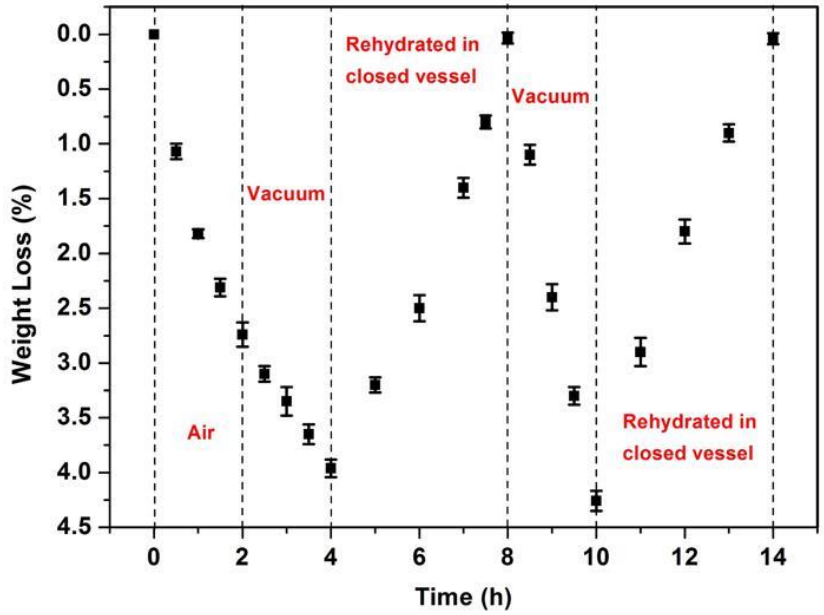

Figure 4.4 Weight loss of five nacre samples with time in different environmental conditions.

Nacre samples were first exposed to ambient air environment for two hours, as indicated in Table 4.1, and resulted in a weight loss of approximately 2.743%. Exposure to the vacuum environment of SEM chamber for two hours caused a further 3.961% weight loss. The initial weight loss of approximately 2.743% during exposure in air indicates a partial removal of free water in nacre whereas exposure to SEM vacuum removes more free water. Rehydration of dehydrated nacre samples for four hours in high vapour concentration recovered almost all lost water compared with the fully hydrated weight. Repeating the exposure to vacuum environment removed similar amount of free water from the sample compared with previous dehydration process and subsequent rehydration recovered the weight loss again, as would be expected if the rehydration process recovering water and the vacuum condition removing the water were consistent. We therefore conclude that

the dehydration-rehydration process removes the free water in nacre samples and can be fully recovered using our applied rehydration method.

4.2.3 Small-deflection Bending Test

Cantilever beam bending tests on both dry and hydrated nacre beams were performed using the custom built AFM (Attocube System AG, Germany) in three different environments: high vacuum (5.25×10^{-4} Pa) SEM vacuum chamber, low vacuum (120 Pa pressure provided by water vapor) SEM vacuum chamber and the ambient air environment by removal of the sample-mounted AFM system out of the SEM chamber. Comparison of the mechanical performance of nacre beams under the three environmental conditions provides an assessment of the hydration of nacre samples in the SEM chamber, which will provide validation of AFM mechanical testing in SEM. Mechanical testing was achieved by first approaching the AFM tip into contact with individual nacre beams as shown in Figure 4.5a. Extending the AFM tip into the free end of the individual nacre beam caused deflection of both the nacre beam and the AFM cantilever, as shown in Figure 4.5b. AFM tip (Bruker Nano GmbH, USA) with a cantilever spring constant of 150 $N \cdot m^{-1}$ (measured using the Sader calibration method (172)) was used for the beam bending experiments. The loading rate was kept constant at 0.2 $\mu m \cdot s^{-1}$ for all bending tests. Each beam was deflected by a small deflection of up to 0.3 μm to ensure elastic behaviour and avoid catastrophic failure so that each beam could be tested repeatedly in the three different environments. In addition, the bending test was performed repeatedly every 20 minutes within the timeframe of 2 hours in the three different

environments to investigate the potential change of mechanical properties of nacre beams within a certain period of time duration.

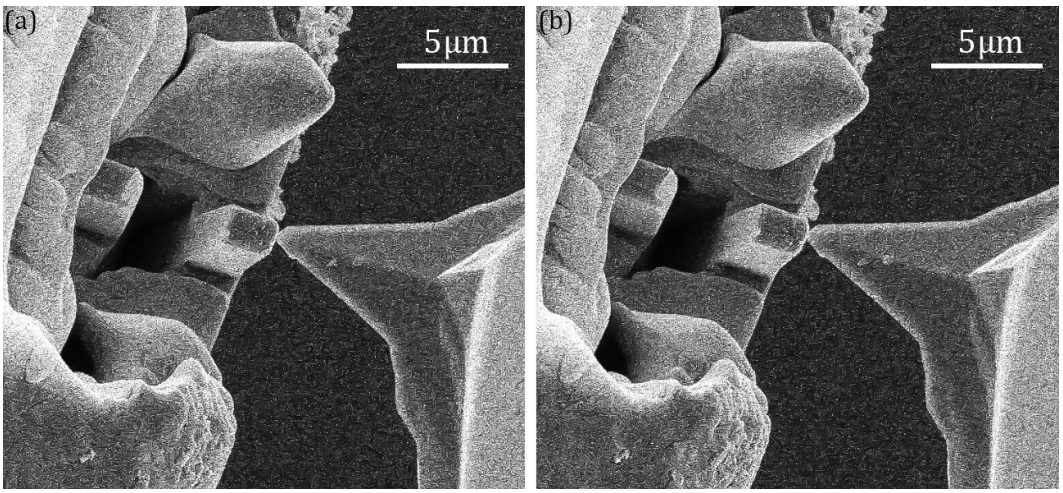

Figure 4.5 SEM images showing the movement of an AFM tip towards a FIB-fabricated nacre beam with (a) the moment the tip prior to contact with the nacre beam and (b) further deflection of the nacre beam. The SEM allows in situ observation of the contact between the AFM tip and the sample without need for AFM imaging whereas the AFM system will record the force acting between the AFM tip and the sample.

4.3 Results and Discussion

Force-deflection curves recorded for the bending tests on both dry and hydrated nacre beams in high vacuum, low vacuum and ambient air environments after 10 minutes of exposure to each environment are shown in Figure 4.6. All the force-deflection curves show a relatively linear trend within the small deflections of up to 0.3 µm so that gradients ($dF/d\delta$) can be fitted to these curves. The elastic modulus (E) of the micron-sized rectangular nacre beams can be calculated from these gradients using the Euler-Bernoulli beam bending theory (187, 188):

$$E = \frac{12l^3}{3bh^3} \cdot \frac{F}{\delta} \qquad \text{Equation 4.1}$$

where F is the force applied to the beam by AFM tip and δ is the resultant deflection of the free end of the beam. l is the length from the bottom of the beam to the contact point of the AFM tip. b and h are the breadth and height of nacre beams respectively. All dimensions were measured directly from SEM imaging. Typical dimensions of individual nacre beams were l = 10 μm, b = 2 μm and h = 2 μm.

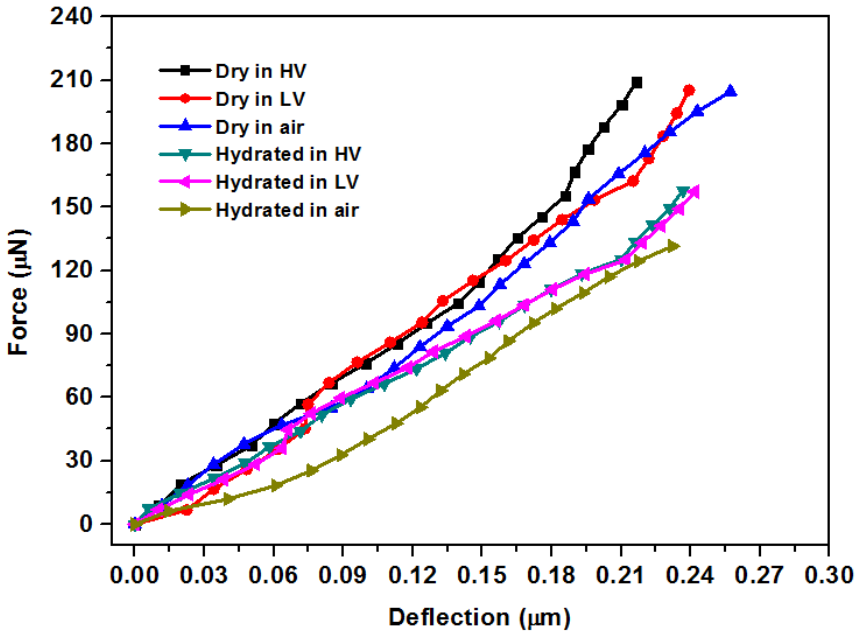

Figure 4.6 Force-deflection curves of the AFM bending tests on dry and hydrated nacre beams under high vacuum, low vacuum and ambient air environments.

Figure 4.7 shows the calculated elastic modulus values for both dry and hydrated nacre beams tested under the three different environmental conditions every 20 minutes within the time frame of 2 hours, with the error in elastic modulus calculated from the standard deviation of the values for the elastic modulus arising from the changes of the contact point during testing. The elastic modulus shows little

change for both dry and hydrated nacre samples either in air environment or time of exposure in the SEM vacuum chamber. This observation is true for all micron-sized nacre beams tested in the cantilever bending test.

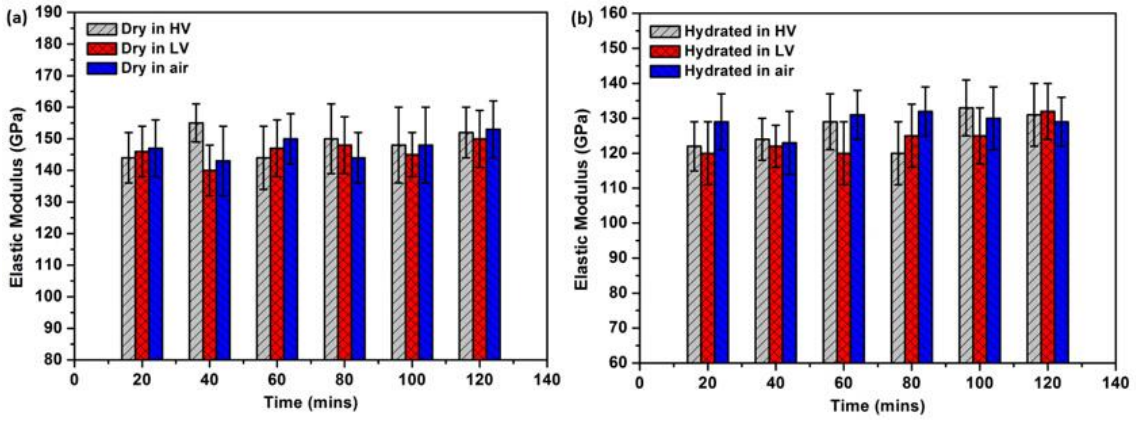

Figure 4.7 Plots of calculated elastic modulus for (a) dry and (b) hydrated nacre beams under high vacuum, low vacuum and ambient air environments within the time duration of 2 hours.

Table 4.2 Calculated elastic modulus of dry and hydrated nacre beams under high vacuum, low vacuum and ambient air environments.

Sample	**Elastic modulus (GPa)**		
	High vacuum	Low vacuum	Ambient air
Dry nacre	150.8 ± 4.3	149.5 ± 4.8	151.4 ± 4.5
Hydrated nacre	129.5 ± 3.9	126.8 ± 4.2	127.9 ± 3.6

The elastic modulus of dry nacre beams calculated from Equation 4.1 are shown in Figure 4.7a for the bending testing in high vacuum, low vacuum and air environments, with results detailed in Table 4.2. All tested environments provide a constant elastic modulus of ~150 GPa, suggesting that both high and low vacuum

and air environments are insufficient for plasticizing the sample due to hydration. Bending of hydrated micron-sized nacre beams in high vacuum, low vacuum and air environments also provides a constant elastic modulus value, which is noticeably lower than dry beams at ~128 GPa, as shown in Figure 4.7b and Table 4.2. These results highlight the inability of the SEM vacuum environment to remove the water molecules that are expected to be tightly bonded within the nacre architecture. Indeed, such a mechanism has been observed for bone material (155). The preparation of biological micro-beams prior to mechanical testing through either dehydrated or hydrated processes is therefore critical in defining whether water is present in the sample whereas high vacuum, low vacuum and air environments simply maintain the level of hydration over the certain period of time duration (120 minutes) evaluated in this work. The elastic moduli calculated from our experiments correlate with previous literature showing that hydrated nacre exhibits a lower elastic modulus than dry nacre due to decrease in the shear modulus and shear strength of the organic matrix in nacre from plasticization from water (85, 92, 183). The elastic modulus of both dry and hydrated nacre beams obtained from our experiments is additionally noted as being slightly higher compared with previous literature results obtained from macroscopic tensile testing (81), potentially due to fewer defects and flaws involved when mechanical testing is carried out at relatively smaller length scales. However, the relatively similar elastic modulus values between our small length scale nacre volumes and whole nacre testing suggests an effective transfer of stress throughout nacre.

4.4 Summary

Small-deflection AFM bending test on both dry and hydrated nacre samples was performed in three different environments: high vacuum SEM environment, low vacuum SEM environment and ambient air environment. The lack of environmental influence on the mechanical properties of the micron-sized nacre beams indicates that the water content is constant in all mechanical testing cases. Biological samples exposed to high vacuum would be expected to provide the largest removal of water but similar elastic modulus of both dry and hydrated nacre beams in three different environments shows that the vacuum driving force is not sufficient to remove the water within the tested nacre volumes. The discrete volumes tested in this work must therefore contain bound water, which is not removed in any of the environmental conditions. We can conclude that the environmental conditions used for mechanical testing of micron-sized nacre beams are not evasive within the timescales examined in this chapter. Subsequent chapters will exploit this novel AFM mechanical testing procedure to examine the small length scale interfaces in nacre and other biological structural composites.

Chapter 5 - On the Nanoscale Origin of Rate-dependent Toughness in Nacre

5.1 Introduction

Nature has developed a diversity of complex biological structures that resist catastrophic failure during externally applied loads. Considerable literature has reviewed the toughness efficiency of these biological structures by examining a wide range of mechanical properties, with optimization of structure using a limited range of materials available highlighted as a particular strength in natural design (9, 14, 15, 18, 20, 189). Critically, these biological structures are often required to resist impact, yet structural design features that enable functional toughness under dynamic loading conditions, as opposed to less physiologically relevant quasi-static loading, is poorly understood. All biological structures exploit the assembly of nanomaterial building blocks to produce complex structures and have been recently demonstrated as effective at resisting extreme loading conditions (77, 162, 190, 191). However, understanding the relationship between these nanomaterials and resultant mechanical function is a persistent challenge, especially for dynamic loading rates that need to be resisted by the structure.

Nacre exhibits perhaps the highest toughness among many stiff biological composite structures (85, 89, 92) and is used in the interior layer of most mollusc shells for protection against dynamic loading conditions from predators and environmental impacts (92). The mechanical importance of nacre has led to a concerted effort in developing bio-inspired synthetic composites for applications where toughness is paramount (3-5, 192). Indeed, the toughness of nacre is outstanding and over three orders of magnitude higher than the aragonite mineral composing approximately 95% of the volume of nacreous structures (85, 89). Despite the high mineral content in nacre, a number of studies have identified the importance of the nanoscale interface region, which consists of organic material approximately 20 nm in thickness that binds the aragonite tablet within a distinctive 'brick and mortar' structure (13, 18, 85). This composite of mineral and organic in nacre is particularly notable as a structure maintaining the stiffness and strength of the mineral constituents (85, 89) while exceeding the toughness of high performance ceramics (85, 90). Evaluations of the loading rate-dependent mechanical properties of nacre are currently limited when compared to quasi-static mechanical performance, with changes in the elastic properties and strength of nacre with loading rate commonly observed (77). Toughening mechanisms have been extensively discussed for nacre under quasi-static testing and include crack deflection between mineral tablets (77, 81), frictional contact between mineral tablets due to tablet dovetailing (36) and tablet nanoasperities (36, 76, 193), deformation of the organic phase (13, 194) and fracture of mineral bridges between tablets (19, 36, 73, 86). However, the relevance of such mechanisms under dynamic loading conditions remains a barrier in understanding the use of nanomaterials within the structure of nacre. The aims of

the work in this chapter are to therefore identify the key mechanisms at the nanoscale interfaces that contribute to the toughness of nacre and provide effective design strategies in resisting dynamic loading.

The approach taken here is to quantify failure at the nanoscale interfaces in nacre directly using techniques that isolate discrete volumes of nacre material. Chapter 3 has reviewed the use of FIB to isolate specific regions of interest in a range of materials including metals, ceramics, polymers and biological samples for mechanical testing (11, 157, 181, 182, 195-197). These experimental methods have yet to be adapted for the evaluation of small scale interfacial failure in nacreous material, or indeed other biological composite structures where interfacial failure is prevalent. In this chapter, the combined technique of in situ AFM within the SEM-FIB dual-beam system described in Chapter 4 is used to investigate the mechanical behaviour of the inorganic-organic interface of nacre at the nanoscale (11, 155, 162, 174, 198). The mechanical testing of materials at small length scales while observing deformation behaviour in SEM has been shown to be particularly effective for identifying the structure-property relationships of a wide range of materials (11, 155, 162, 174, 196, 198). FIB is used to fabricate nacre samples into discrete volumes containing a single nanoscale interface for subsequent AFM mechanical testing, allowing direct study of the intrinsic nanoscale interface rather than the overall mechanical behaviour of whole nacre. These FIB-fabricated nacre samples were mechanically tested using the custom built in situ AFM system as detailed in Section 3.4. Standard mechanical testing of bulk composites often exploits shear stress to evaluate the strength of interfaces using a range of sample geometries and loading

conditions (92, 93, 183). Controlled failure at the nanoscale interfaces can therefore be achieved with suitable sample geometries fabricated using FIB. Failure at nanoscale interfaces was further correlated with modelling approaches to define the influence of intrinsic behaviour on the overall toughness of nacreous structures.

5.2 Materials and Methods

5.2.1 Macroscopic Tensile Test

Preliminary nacre sample preparation was performed following the procedure described in Section 4.2.1. Small dog-bone shaped nacre specimens were fabricated from the nacreous layer of abalone shells, at locations where the shell had minimal curvature using the water cooled rotating diamond saw. The width and thickness of the specimen was 1.2 mm and 0.6 mm. The gauge length of the specimen was 2.0 mm and the overall length of the specimen was 18.0 mm. The specimens were cut such that their long axis was aligned with the plane of the mineral tablets. Macroscopic quasi-static tensile test was performed on both dry and hydrated nacre samples using a commercial microtester (Deben, 200 N tensile stage, UK), as shown in Figure 5.1. Samples defined as dry were kept at ambient temperature and humidity in air prior to mechanical testing, while hydrated samples were soaked in distilled water for at least 2 hours prior to mechanical testing. The specimens were loaded at a strain rate of about 0.001 s^{-1}, up to failure. Four specimens were tensile tested for each case.

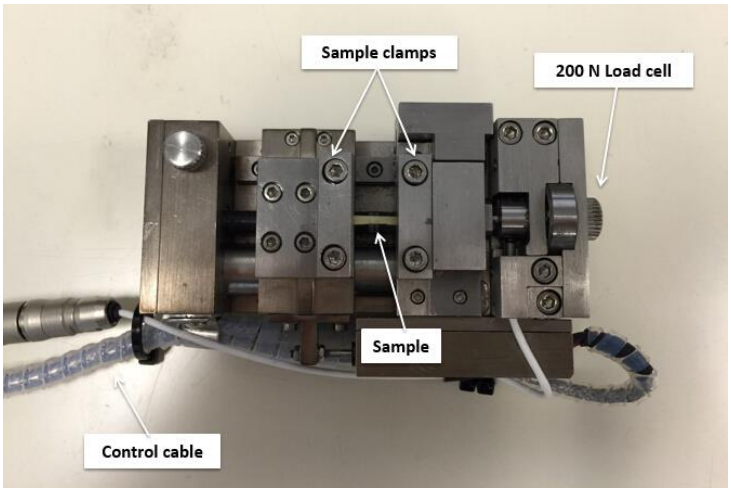

Figure 5.1 Digital image of the microtester, with the arrows showing the components of the tester.

5.2.2 Nanoscale Interfacial Shear Test

The nanoscale interfacial shear test was performed using the custom built in situ AFM within the SEM-FIB dual-beam system described in Chapter 3. Preliminary nacre sample preparation was performed as described in Section 4.2 so that only hydrated nacre samples were investigated in this work. The key point of the FIB sample preparation was to ensure that the nacre beam was FIB fabricated with the mineral tablets stacked perpendicular to the long axis of the beams. The backscattered electron micrograph, as shown in Figure 5.2, clearly shows the interfaces between mineral tablets as the dark lines and the mineral tablets in brighter pattern.

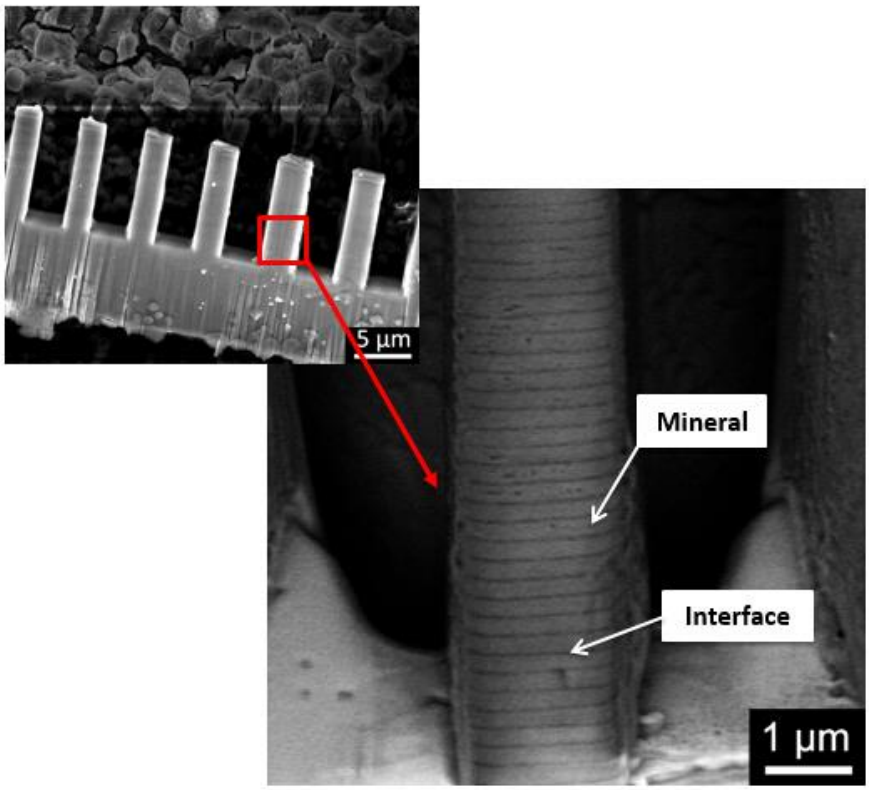

Figure 5.2 Backscattered electron micrograph of the FIB-fabricated nacre beam for nanoscale interfacial shear testing, with the mineral plate perpendicular to the long axis of the beam. Arrows show the existence of the mineral tablet and the organic interface. The insert SEM micrograph shows the FIB fabricated nacre beams at low magnification.

FIB-flattened AFM tips (Bruker Nano GmbH, USA) with cantilever spring constant of 40 $N \cdot m^{-1}$ was moved towards the bottom of the beam while imaging with SEM to ensure the tip contacted the base of the beam, as illustrated in Figure 5.3. Figure 5.3a indicates SEM imaging of the AFM tip approaching and contacting the base of an individual nacre beam and Figure 5.3b shows application of load to the base of the nacre beam, which results in shearing between the mineral tablets. The expected shearing on the interfaces between the mineral tablets in shown schematically in Figure 5.3c and d. Under this protocol, shear deformation occurs at the interface

between the bottom FIB-fabricated mineral tablet and the top surface of the bulk nacre sample. A range of loading rates (0.2 $\mu m \cdot s^{-1}$, 10 $\mu m \cdot s^{-1}$, 30 $\mu m \cdot s^{-1}$, 60 $\mu m \cdot s^{-1}$ and 90 $\mu m \cdot s^{-1}$) were applied in the shear test to investigate the influence of varying loading rates on the nanoscale interfacial shear behaviour of nacre. Four nacre beams were shear tested for each loading rate to determine an average value of shear strength.

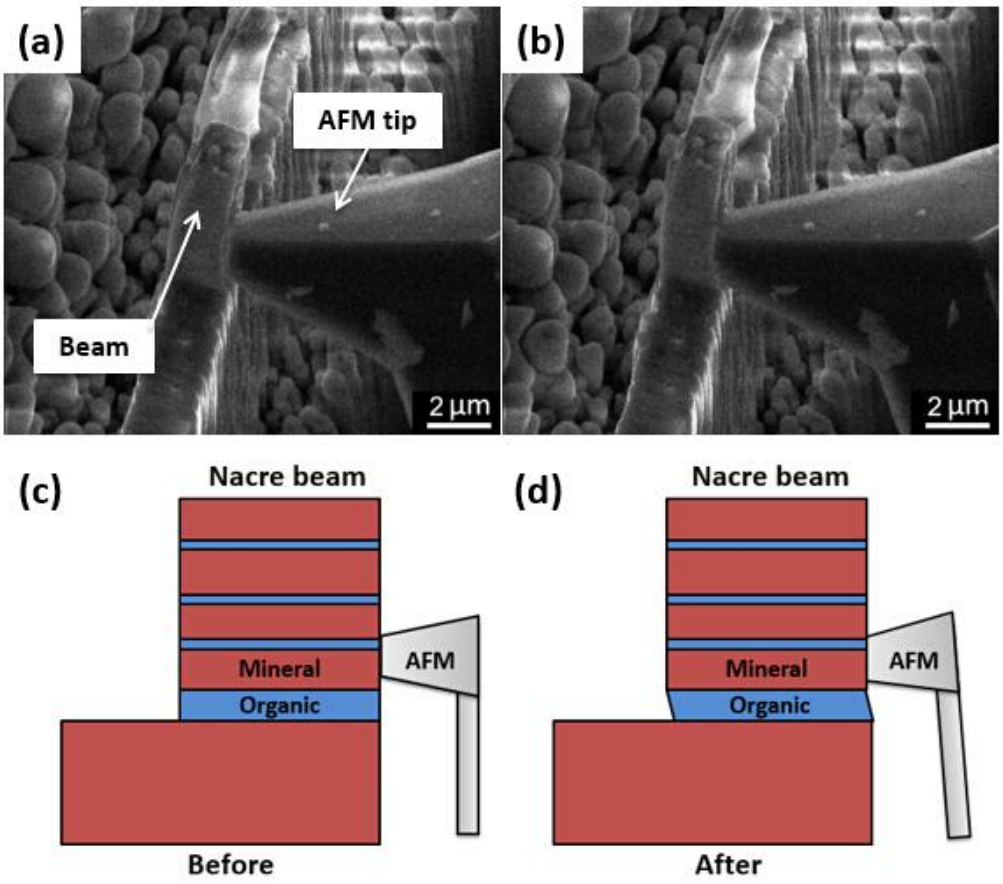

Figure 5.3 (a) SEM micrograph and (c) schematic showing the AFM tip approaching and contacting the base of an individual nacre beam; (b) SEM micrograph and (d) schematic showing application of load to the base of the nacre beam causing shearing between the mineral plates. Note the organic region at the base of the beam in the schematic is represented as larger than in the SEM image for clarity.

The shear strain (γ) at the interface between mineral plates in an individual nacre beam is defined by:

$$\gamma = \frac{\delta}{S} \qquad \text{Equation 5.1}$$

where δ is the axial displacement along the interface, and S is the distance between the point of applied force and the shear plane. The shear stress (τ) at this interface is defined as:

$$\tau = \frac{F}{A} \qquad \text{Equation 5.2}$$

where F is the force applied by the AFM tip to the sample and A is the interfacial area where shear occurs. The maximum shear stress to fail the interface between mineral tablets can therefore be calculated from Equation 5.2 as well as measuring the maximum force applied to the sample from the AFM and knowing the interface area from SEM images.

5.3 Results

5.3.1 Macroscopic Tensile Test

Figure 5.4 shows the stress-strain curves of the macroscopic tensile test on dry and hydrated nacre samples. Dry nacre behaved like a monolithic ceramic and failed in a brittle fashion. The response was linear elastic (E~100 GPa) up to a failure stress of ~100 MPa at a failure strain of 0.001. The behaviour of dry nacre is similar to that of pure aragonite (92). By contrast, hydrated nacre showed a linear elastic response

(E~60 GPa) followed by a region of larger inelastic strains starting at a stress of 62 MPa, with a final maximum strain to failure of 0.009 ± 0.001. The increase in the strain to failure of hydrated nacre relative to dry nacre highlights the role of water in plasticizing the organic phase at the interface between the mineral tablets. The water affects the elastic modulus and tensile strength of nacre by reducing the shear modulus and shear strength of the organic matrix between mineral tablets. Toughness is enhanced by water, which plasticizes the organic matrix, resulting in greater crack blunting and deflection abilities. The tensile behaviour of both dry and hydrated nacre corroborates previous macroscopic tensile tests on nacre (85, 92, 183). We obtain an average hydrated nacre toughness of 720.2 ± 34.0 $J \cdot m^{-3}$ by calculating the areas under the stress-strain curves. This toughness value serves as a macroscopic toughness value when considering the nanoscale interfacial shear test discussed below.

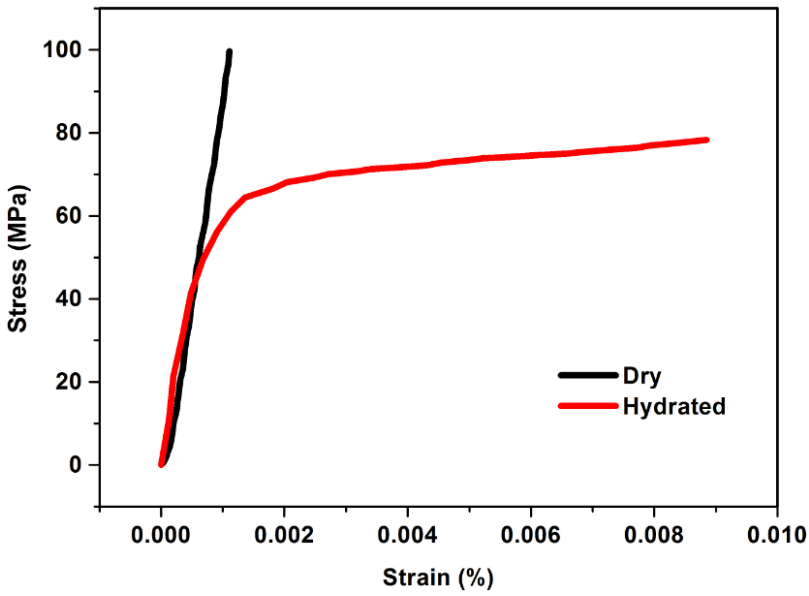

Figure 5.4 Typical stress-strain curves of dry and hydrated dog-bone shaped nacre samples under macroscopic tensile testing.

5.3.2 Nanoscale Interfacial Shear Test

Typical shear stress-strain curves for the nanoscale interfacial shear test are shown in Figure 5.5. All the curves indicate a relatively linear deformation up to the maximum shear stress, with slight plastic behaviour during the deformation. This mechanical behaviour shows no clear transition from elastic deformation to plastic deformation at the nanoscale interfacial level, which is contrary to the initial elastic region followed by a considerably larger linear plastic region observed in macroscopic shear testing (77, 92). The discrepancy between linear elastic-like behaviour in micron-sized nacre beams and a plastic response in macroscopic testing is expected to be due to the nanoscale lacking extrinsic crack deflection mechanisms available macroscopically. The nanoscale shear test is therefore evaluating the intrinsic shear response at the interface between adjacent mineral tablets. We additionally note that the linear increase in stress with strain in Figure 5.5 lacks the drop in stress with strain associated with failure of mineral bridges between tablets (19, 36, 73, 86), suggesting that these mineral bridges do not play a significant role in interfacial mechanics of nacre.

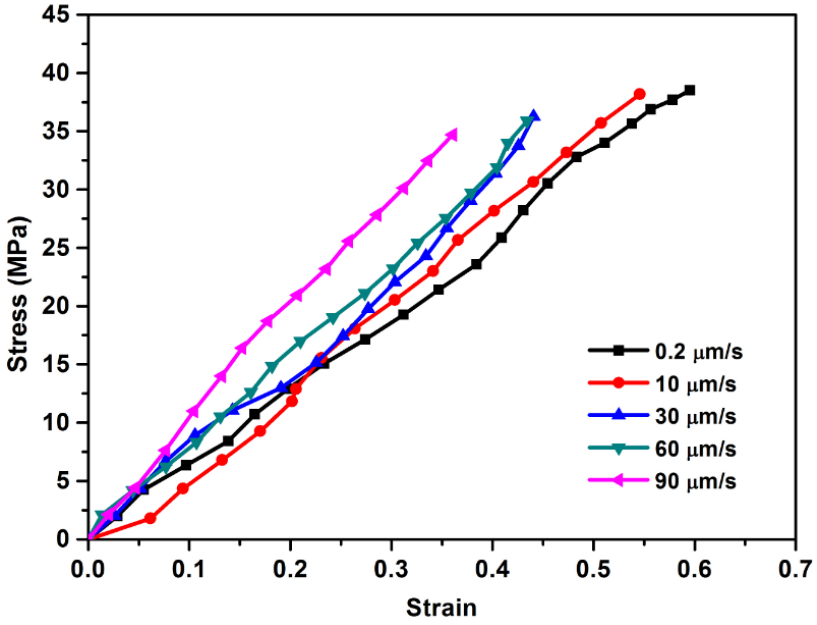

Figure 5.5 Stress-strain curves for nanoscale interfacial shear testing of hydrated nacre samples using five different loading rates (0.2 μm·s^{-1}, 10 μm·s^{-1}, 30 μm·s^{-1}, 60 μm·s^{-1} and 90 μm·s^{-1}).

The loading rate-dependent properties of the nanoscale interfaces in nacre are expected to be critical in defining the functional toughness of nacre and were thus explored further. Figure 5.6 shows the variation of shear strength, taken as the maximum stress applied from Figure 5.5 across a range of loading rates, in order to explore the dynamic response of the nanoscale interfaces in nacre. The interfacial shear strength is defined by the soft phase between the hard mineral plates and is observed to decrease as the loading rate increases as shown in Figure 5.6. A loading rate increase of approximately two orders of magnitude caused a shear strength decrease of approximately 10%. The y-axis starts from 33.5 MPa in order to emphasize the small shear strength change in the range between 33.5 MPa and 40.5 MPa. The corresponding interfacial work of fracture calculated from the area under the stress-strain curves as shown in Figure 5.6 also exhibits a degradation of

mechanical behaviour as the loading rate increases. The values of the interfacial shear strength and work of fracture under different loading rates are presented in Table 5.1. The variation in interfacial mechanical properties of nacre under different loading rates provides evidence for design strategies that potentially enhance energy absorption with higher rate impact.

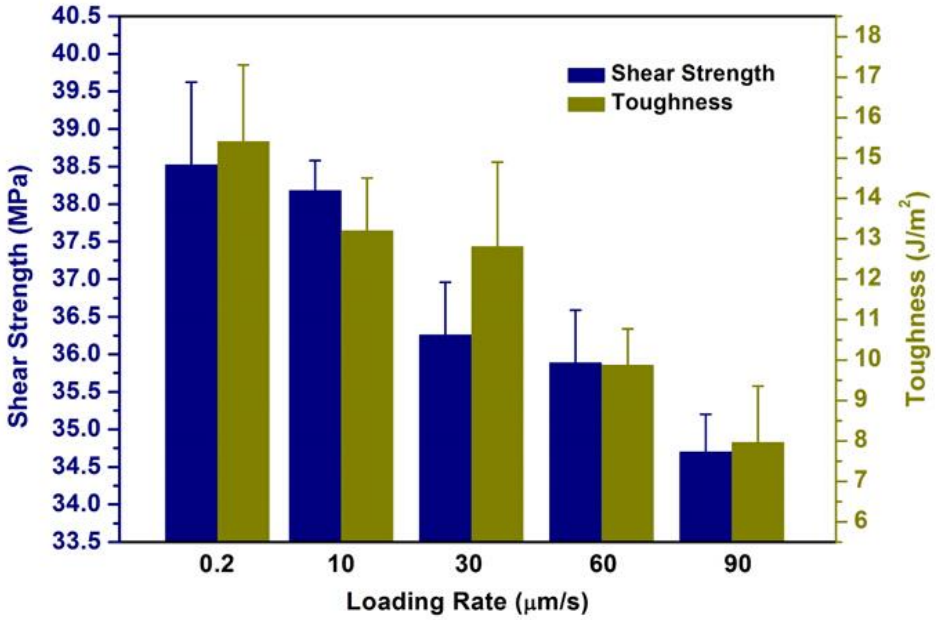

Figure 5.6 Plot of the nanoscale interfacial shear strength and work of fracture between mineral tablets under five different loading rates (0.2 μm·s^{-1}, 10 μm·s^{-1}, 30 μm·s^{-1}, 60 μm·s^{-1} and 90 μm·s^{-1}).

Table 5.1 Shear strength and interfacial toughness obtained from the interfacial shear test on nacre under different loading rates.

Loading rate ($\mu m \cdot s^{-1}$)	Shear strength (MPa)	Standard deviation	Interfacial toughness ($J \cdot m^{-2}$)	Standard deviation
0.2	38.525	1.156	15.476	1.926
10	38.180	0.462	13.243	1.385
30	36.257	0.786	12.838	2.162
60	35.888	0.775	9.873	0.975
90	34.739	0.524	7.964	1.457

5.4 Discussion

Interfacial shear strength and work of fracture are clearly observed to decrease with increasing loading rate as shown in Figure 5.6, and highlight the intrinsic weakening of the nanoscale interface in nacre as the loading rate increases. Such an observation is perhaps counter-intuitive as a higher loading rate impact will transfer more kinetic energy to the shell and, thus, the expectation that more work is required to fail the interfaces in order to absorb this impact energy. Synergy between this intrinsic material behaviour and extrinsic effects that define resultant failure must be considered in order to fully evaluate the toughness of nacre under dynamic loading conditions. Specifically, weak interfaces in composite structures are known to enhance crack propagation and increase toughness in quasi-static tests as the resultant failed surface area evolved increases (199, 200). Maintaining toughness with increased loading rate deviates from quasi-static conditions and are typically

achieved in, for example, engineered fibre reinforced plastics composites (201) where the mechanical properties of the polymer phase such as stiffness and strength increases. The advantage of decreasing interfacial strength with increasing loading rate as shown in Figure 5.6 must be considered.

Two possible nanoscale mechanisms are expected to be responsible for this rate-dependent shear behaviour. The first rate-dependent mechanism must consider the organic molecules entangled along the interface between mineral tablets (13, 194). These long organic molecules elongate in a stepwise manner as folded domains or loops are pulled open during tablet sliding, with previous literature detailing a saw tooth pattern in force-extension curves when the molecular chains were stretched by an AFM probe and demonstrated that every peak in the saw tooth pattern corresponded to a single chain domain unfolding (13). During further tablet sliding, the force repeatedly rises to a significant fraction of the force required to break a strong bond, but before a strong bond is broken, another domain unfolds. This process continues until all domains are unfolded and a strong bond breaks. The result is to sustain a relatively large force during tablet sliding before interfacial failure, making the nanoscale interface strong, while producing a larger area under the force-deflection curve for enhanced toughness. However, this stepwise elongation behaviour of the long molecules is a relatively slow process (13). At high loading rates, the long molecules have insufficient time to elongate, thus decreasing the mechanical energy that can be absorbed during this elongation process. Slower loading rates allow sufficient time for the long molecules to unfold fully so that a

relatively large shear stress could be achieved during tablet sliding before interfacial failure, thus providing an increase in the interfacial shear strength.

The second responsible mechanism is derived from potential electrostatic attraction along the inorganic-organic interface (202-205). At molecular length scales, positively charged divalent calcium ions in the mineral tablets interact with proteins, amino acids or polysaccharides containing negative charges within the organic region between the mineral tablets (184). The divalent calcium ions and negatively charged functional groups can form a network of sacrificial ionic bonds by electrostatic attractions along the inorganic-organic interface (184), as shown schematically in Figure 5.7. The work required to break this network during tablet sliding will cause failure of the sacrificial ionic bonds in the network. Previous works have shown how the sacrificial ionic bonds along the interface can reform to some extent, indicating these bonds can break and reform several times before complete interfacial failure (202-205). In this work, the nanoscale interfacial shear strength increases as the loading rate decreases. We believe that the sacrificial bond reforming during tablet sliding is responsible for larger shear strength when the loading rate is relatively low. Higher loading rates would allow insufficient time for the divalent calcium ions to transport sufficiently to bond reforming sites, which leads to a decreased shear strength. Slower tablet sliding velocities will therefore provide more time for the broken ionic bonds to reform, resulting in higher shear strength and more mechanical energy absorbed during tablet sliding.

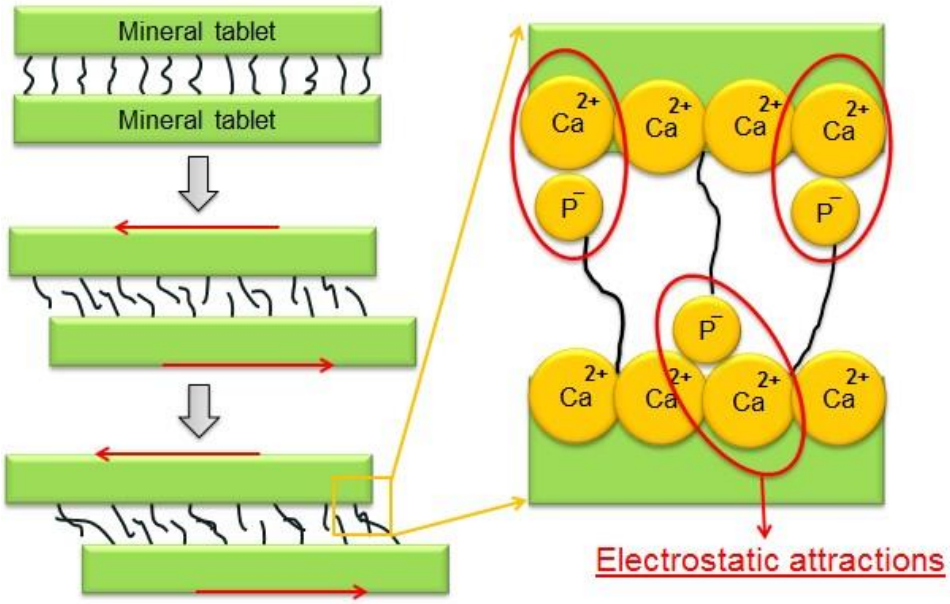

Figure 5.7 Schematic of the sacrificial ionic bonding network existing within the nanoscale inorganic-organic interface with the green rectangles representing aragonite mineral tablet and short random lines representing organic molecules. The grey arrows indicate the movement of mineral tablets causing shear along the interface. During tablet sliding, broken sacrificial bonds can reform to some extent by electrostatic attractions between the divalent calcium ions and negatively charged functional groups.

5.5 Summary

In conclusion, the nanoscale interfacial shear test on the inorganic-organic interface in nacre was performed using the in situ AFM within the SEM-FIB dual-beam system. Decreasing interfacial shear strength and work of fracture was found with increasing loading rates. Two potential interfacial mechanisms relating to entangled long organic molecule dynamics along the organic interface and the sacrificial ionic bond reformation between adjacent mineral tablets are proposed as being responsible for this rate-dependent shear behaviour. Such tuning of mechanical behaviour of the

nanoscale interfaces in nacre allows extrinsic failure to be the dominant toughening mechanism. True biomimetic design must therefore consider optimization of nanoscale interface behaviour to maximize the work to failure through an enhanced damage zone.

Chapter 6 - Rate-dependent Interfacial Nanomechanical Trends in Biological Composites

6.1 Introduction

The study of biological materials that have evolved through millions of years of evolution and natural selection can provide insights into heretofore-unexploited mechanical behaviour. A significant number of biological systems found in nature are subjected to a wide range of loading conditions for which the quasi-static test is simply not suitable in recreating the physiological loading conditions. Numerous structural biological composites are mechanically robust across a wide range of loading rates. Examples are prevalent in nature including the dynamic loadings of abalone shell as studies in Chapter 5 through impacts from predators and environmental aggression like rocks and debris (81), the fast loading rates found in the impact of deer antler bone (6) and the shell breaking appendages of mantis shrimp (arthropod) (97, 98). These biological composite systems exhibit common structural features at the nanoscale including a stiff majority reinforcement or

scaffold surrounded by an amorphous interfacial region with a relatively small volume. Small changes to these interfacial regions are expected to have a significant effect on dynamic mechanical response of the material.

However a majority of previous mechanical studies on these structural biological materials have been limited to quasi-static loading conditions while the dynamic mechanical properties of biological materials are scarce in the literature (17, 44, 77). The rate-dependent mechanical properties of these biological composites are expected to be localized in the flexible organic molecules in the narrow interfaces between biological reinforcements, which are themselves mechanically rate dependent. Our studies on the rate-dependent interfacial mechanical properties of nacre in Chapter 5 serve as a good example. But what is the dynamic mechanical behaviour of other structural biological composites besides nacre? Do they show similar behaviour as nacre or different mechanical performance? How does the confined nansocale interfacial structures in these biological systems control their dynamic mechanical performance? Furthermore, what is the relationship between their dynamic mechanical properties and their physiological loading conditions they experience in their real lives? To address these questions, we need more rate-dependent mechanical properties of biological composites and establish a relationship with their physiological loading conditions.

This chapter thus attempts to determine the relationship between the rate-dependent mechanical behaviour of biological composites with their nanoscale interfacial structures and their physiological loading conditions. The rate-dependent

mechanical properties of the nanoscale interfaces in nacre have been experimentally studied and modelled in Chapter 5 using the technique combing SEM, FIB and AFM. A weakening of inorganic-organic interfaces but enhanced overall nacre toughness was observed with higher loading rates applied in the experiment. The techniques developed in the last chapter are extended to study arthropod exoskeleton in this chapter. Arthropod exoskeleton has a unique hierarchical architecture from the macroscale to the nanoscale, which has been discussed in detail in Section 2.5, and is robust at higher loading rates than for nacre. Therefore, in this chapter, the nanoscale interfacial shear test on the interface between exocuticle layers of arthropod exoskeleton was performed under different loading rates using the same mechanical testing methodology applied on study of nacre in Chapter 5. Results on nacre and exocuticle are compared to literature, specifically previous work by Hang et al. (175) that investigated the rate-dependent nanoscale interfacial strength between non-collagenous protein and collagen fibrils in antler bone. Comparison of the rate-dependent interfacial mechanical behaviour of the above three well-studied biological composites (nacre, arthropod exoskeleton and antler bone) and the relationship to their physiological loading conditions are discussed in the following sections to present a general mechanism of biological composite behaviour under dynamic loading.

6.2 Materials and Methods

6.2.1 Sample Preparation

Two adult mantis shrimps were obtained from the Tropical Marine Centre Company, UK. The mantis shrimps were in the intermolt stage, in which the exoskeleton was completely developed and fully mineralized (206, 207). The mantis shrimp samples were transported to the lab in frozen condition and directly stored in the freezer at -20°C before dissection. Small exoskeleton sections with dimensions of approximately 8 × 4 × 4 mm were isolated from parent mantis shrimp samples using a water-cooled rotating diamond saw. Figure 6.1 shows optical images of a complete mantis shrimp and an exoskeleton piece sectioned for subsequent FIB fabrication.

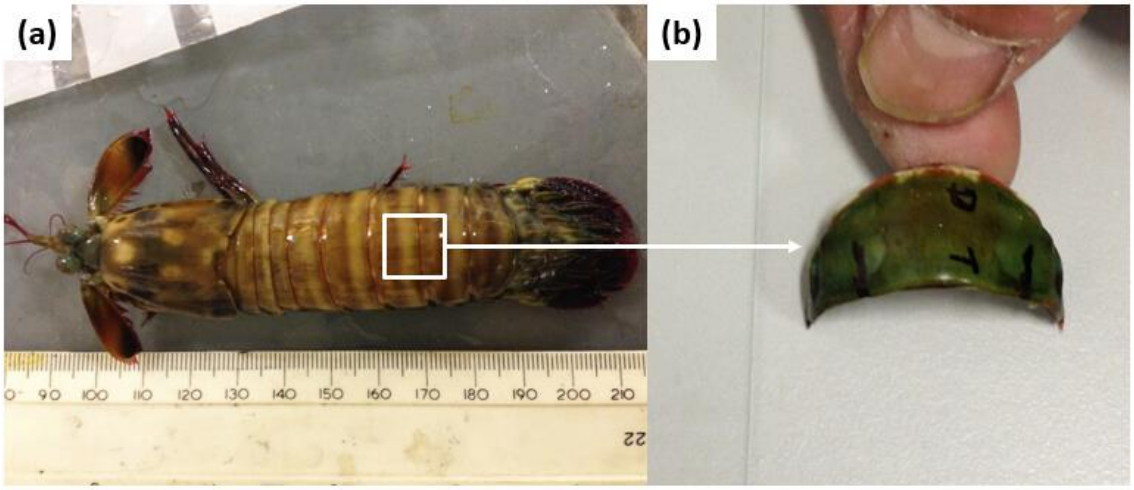

Figure 6.1 Optical images showing (a) the complete mantis shrimp and (b) one exoskeleton piece sectioned from the parent mantis shrimp sample.

The exoskeleton sections were thoroughly rinsed and kept in distilled water at room temperature in order to keep the samples clean and hydrated. Before FIB fabrication, sections were removed from distilled water and maintained in ambient air environment for 2 hours to provide dehydration prior to SEM imaging and FIB fabrication. Sections were subsequently sputter gold coated to avoid electron or ion charging effects that could interfere with FIB fabrication (155, 181), followed by placement into the SEM chamber. The exoskeleton section was mounted on the SEM sample stage with the order of epicuticle, exocuticle and endocuticle from top to bottom. The thin layer of epicuticle with thickness of approximately 4.8 μm was firstly removed using FIB to expose the exocuticle layer, which is the main subject of this preparation. The exocuticle layer, which shows a thickness of approximately 10 μm, is stacked more densely and regularly than the endocuticle layer. The interfaces were assumed to be similar throughout the exoskeleton as the materials used throughout are similar, but the exocuticle was considered more preferable for FIB fabrication and mechanical investigation on the interface between layers as porosity, such as found in the endocuticle or epicuticle, was absent. Figure 6.2 shows the SEM micrographs of the structure of the epicuticle, exocuticle and endocuticle layers at different magnifications, indicating the layered exoskeleton clearly. Individual rectangular beams were created following the same FIB fabrication procedure described in Section 3.3 into dimensions of approximately 35 × 8 × 8 μm as shown in Figure 6.2d. The exocuticle layers are stacked through the beam with the interfaces perpendicular to the long axis of the beam so that interfacial shear testing on the beam can be performed.

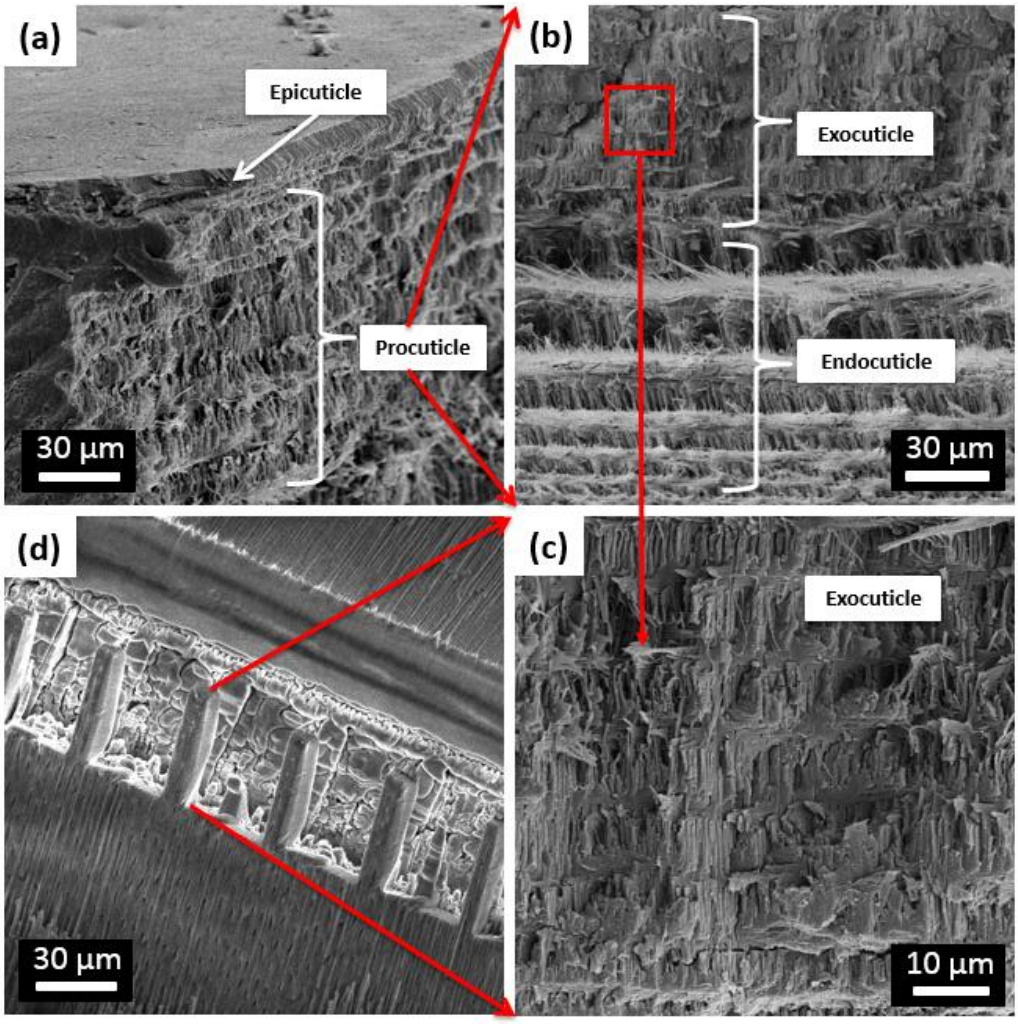

Figure 6.2 SEM micrographs showing (a) the existence of the thin epicuticle layer above the procuticle layer, (b) the exocuticle (outer) and endocuticle (inner) layers comprising the procuticle layer, (c) the exocuticle layer only showing the well-organized layered structure and (d) the FIB-fabricated exocuticle beams with the exocuticle layers stacked perpendicular to the long axis of the beam.

FIB-fabricated exoskeleton samples were rehydrated following the same rehydration protocol described in Section 4.2.1 to ensure the exoskeleton samples were fully rehydrated when mechanically tested. Table 6.1 records the weight loss measured from five exoskeleton samples subjected to various environmental conditions used in the sample preparation process and Figure 6.3 shows the weight

change with time. Exoskeleton samples were kept in distilled water before preparation. Samples were then removed from water and weighed using an electronic analytical microbalance (Sartorius, Germany) to four significant figures after removing excess water from the sample's surface with filter paper. The weights of these samples were taken as fully hydrated weight. Further preparation processes were recorded by the percentage of weight loss relatively to this fully hydrated sample weight as shown in Table 6.1.

Table 6.1 Change in weight, as a percentage of the weight difference relative to hydrated exoskeleton samples in distilled water. The cycle of hydration represented by the table was repeated on five different exoskeleton samples.

Sample conditions	**Time (hours)**	**Weight loss compared to hydrated condition in distilled water (%)**
Stored in distilled water	Storage	0.000 ± 0.015
Dehydrated in ambient air	2	6.746 ± 1.233
Dehydrated in SEM vacuum (High vacuum 5.25×10^{-4} Pa)	2	7.861 ± 0.792
Rehydrated in high vapour concentration	4	0.224 ± 0.265
Dehydrated in SEM vacuum (High vacuum 5.25×10^{-4} Pa)	2	6.955 ± 1.219
Rehydrated in high vapour concentration	4	0.287 ± 0.353

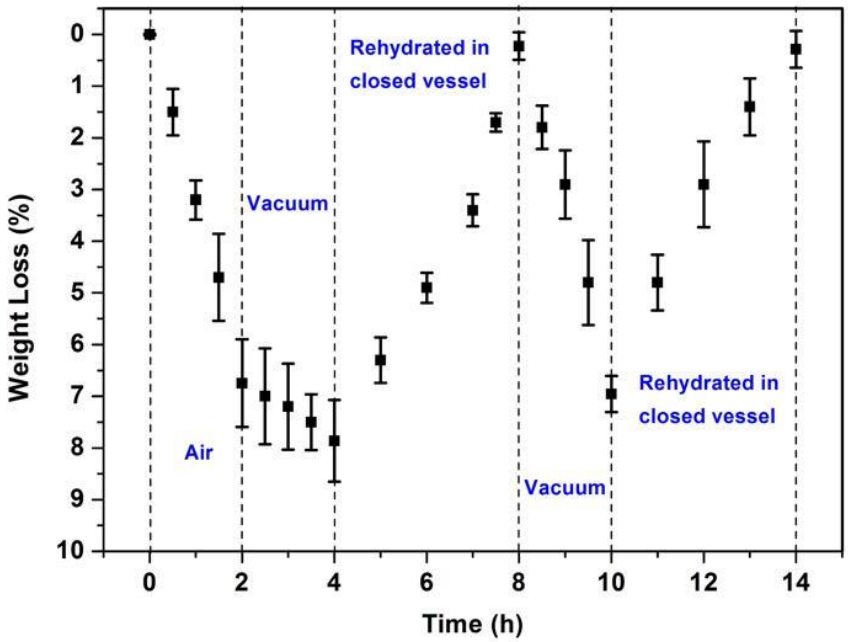

Figure 6.3 Weight loss of five arthropod exoskeleton samples with time in different environmental conditions.

Exoskeleton samples were first exposed to ambient air environment for two hours, as indicated in Table 6.1, and resulted in a weight loss of approximately 6.746%. Exposure to the vacuum environment of SEM chamber for two hours caused a further 7.861% weight loss. The initial weight loss of approximately 6.746% during exposure in air indicates a partial removal of free water in exoskeleton samples whereas exposure to SEM vacuum removes more free water. Rehydration of dehydrated exoskeleton samples for four hours in high vapor concentration recovered almost all lost water compared with the fully hydrated weight. Repeating the exposure to vacuum environment removed similar amount of free water from the sample compared with previous dehydration process and subsequent rehydration recovered the weight loss again, as would be expected if the rehydration process recovering water and the vacuum condition removing the water were

consistent. We therefore conclude that the dehydration-rehydration process removes the free water in exoskeleton samples and can be fully recovered using our applied rehydration method.

6.2.2 Nanoscale Interfacial Shear Test

Interfacial shear testing was applied to examine exocuticle layers within hydrated FIB-fabricated exoskeleton samples using the custom built in situ AFM within the SEM-FIB dual-beam system as detailed in Section 3.4. A FIB-flattened AFM tip (ACT, AppNano, USA) with spring constant of 200 $N \cdot m^{-1}$ was moved towards the bottom of the beam while imaging with SEM to ensure the FIB-flattened AFM tip contacted the bottom of the beam, as shown in Figure 6.4. A stiffer AFM cantilever was used when compared to the nacre testing in Chapter 5 as the AFM cantilever required larger forces applied to the exocuticle samples to cause shear failure, especially as the FIB-fabricated beams were generally larger than for nacre. In this way, shear deformation could be controlled to occur at the interface between the bottom FIB-fabricated exocuticle layer and the top surface of the bulk exocuticle sample. A wide range of loading rates (0.2 $\mu m \cdot s^{-1}$, 24 $\mu m \cdot s^{-1}$, 55 $\mu m \cdot s^{-1}$, 78 $\mu m \cdot s^{-1}$ and 110 $\mu m \cdot s^{-1}$) were applied in the shear test to investigate the influence of varying loading rates on the interfacial shear behaviour of exocuticle. Three exocuticle beams were shear tested for each loading rate to determine an average value of mechanical properties. The strain and stress information were calculated using the same method as described in Section 5.2.2.

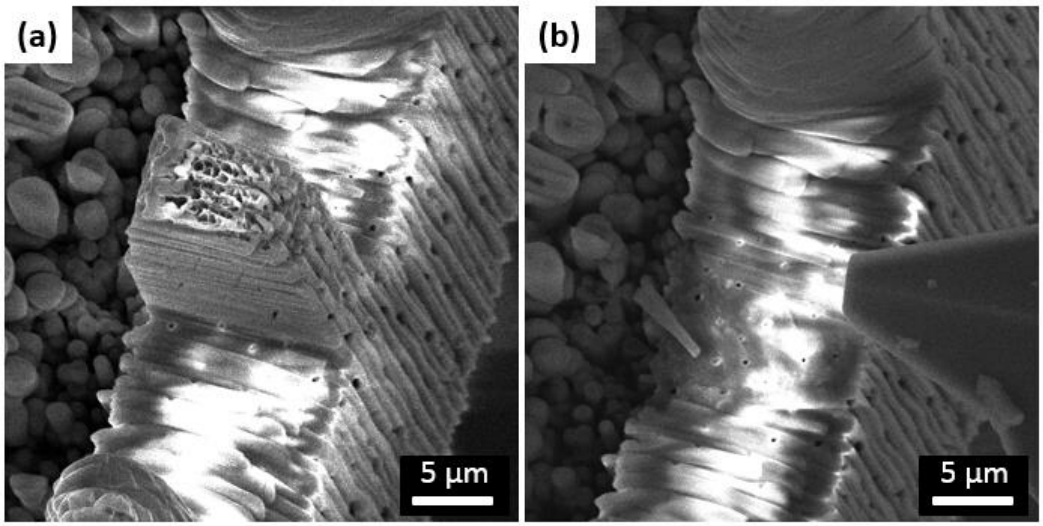

Figure 6.4 SEM micrographs showing (a) the FIB-fabricated exocuticle beam before mechanical testing and (b) the failed interface after the AFM interfacial shear test.

6.3 Results

Typical shear stress-strain curves for the interfacial shear test between exocuticle layers under five different loading rates (0.2 µm·s^{-1}, 24 µm·s^{-1}, 55 µm·s^{-1}, 78 µm·s^{-1} and 110 µm·s^{-1}) are shown in Figure 6.5. The loading rate information was obtained directly from the Attocube AFM system and translated into standard velocity with the unit of µm·s^{-1}. The loading rates span over two orders of magnitude with the lowest velocity representing quasi-static test while the highest velocity coming close to the physiological loading rate for arthropod exoskeleton (8). All the curves indicate a relatively linear deformation up to the maximum shear stress with catastrophic failure through shear as observed from SEM. The shear behaviour showed no clear transition from elastic deformation to plastic deformation at this nanoscale interfacial level, which is similar to the nanoscale interfacial shear behaviour of nacre as detailed in Chapter 5. This linear elastic-like behaviour in

micron-sized exocuticle beams with no further plastic deformation stage is expected to be due to the nanoscale lacking extrinsic crack deflection mechanisms available macroscopically. The nanoscale interfacial shear test is therefore evaluating the intrinsic shear response at the interface between adjacent exocuticle layers.

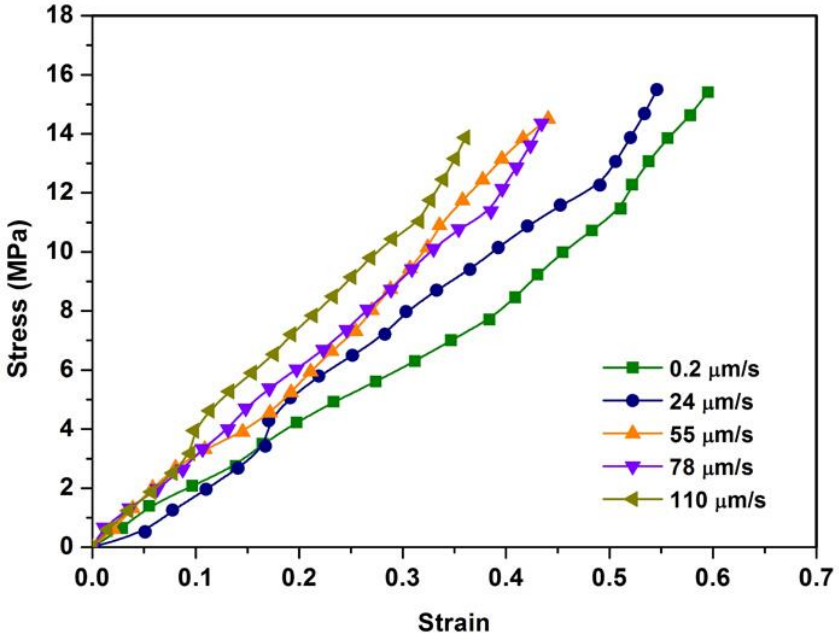

Figure 6.5 Stress-strain curves of the nanoscale interfacial shear test on hydrated exocuticle layers under five different loading rates (0.2 μm·s^{-1}, 24 μm·s^{-1}, 55 μm·s^{-1}, 78 μm·s^{-1} and 110 μm·s^{-1}).

The loading rate-dependent properties of the interface in exoskeleton are expected to be important in defining the functional toughness of exoskeleton and were thus explored further. Figure 6.6a shows the variation of shear strength, taken as the maximum stress applied from Figure 6.5 across a range of loading rates, in order to explore the dynamic response of the nanoscale interfaces. The error bar results from varying shear strength obtained from different shear tests under the same loading rate. The interfacial shear strength is defined by the interface between two

exocuticle layers and is observed to decrease as the loading rate increases as shown in Figure 6.6a. A loading rate increase of approximately two orders of magnitude caused a shear strength decrease of 11%. The corresponding interfacial toughness calculated from the area under the stress-strain curves as shown in Figure 6.6b also exhibits a degradation of mechanical behaviour as the loading rate increases. The values of the interfacial shear strength and toughness under different loading rates are presented in Table 6.2. The variation in interfacial mechanical properties of exoskeleton under different loading rates shows a similar trend as that of nacre and provides evidence for design strategies that potentially enhance energy absorption with higher rate impact.

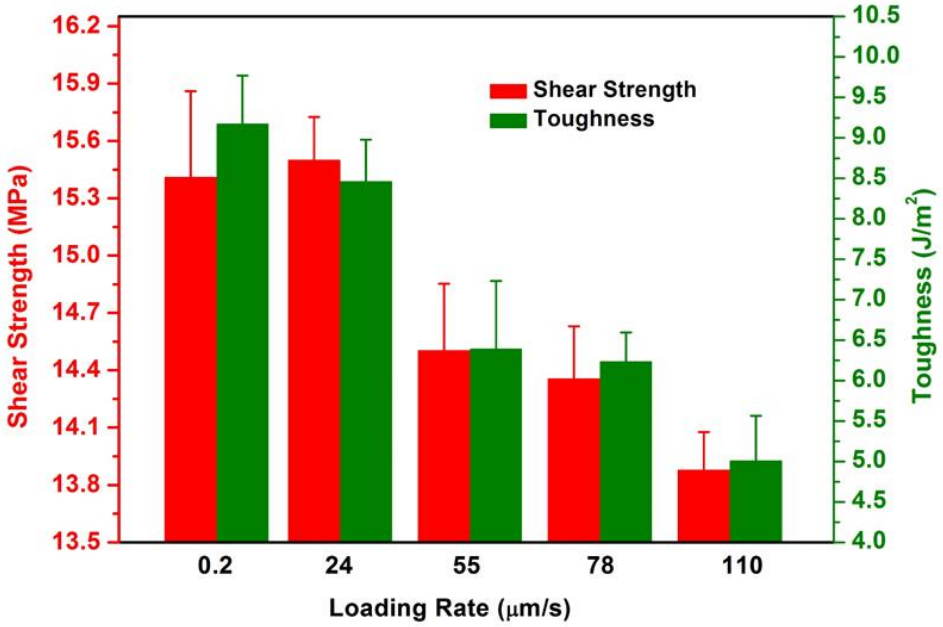

Figure 6.6 Plot of the nanoscale interfacial shear strength and work of fracture between exoskeleton layers under five different loading rates. (0.2 μm·s^{-1}, 24 μm·s^{-1}, 55 μm·s^{-1}, 78 μm·s^{-1} and 110 μm·s^{-1}).

Table 6.2 Average shear strength and interfacial toughness with standard deviation obtained from the interfacial shear test on exoskeleton under different loading rates. Loading rates are arranged from lowest to highest.

Loading rate ($\mu m \cdot s^{-1}$)	**Shear strength (MPa)**	**Standard deviation**	**Interfacial toughness ($J \cdot m^{-2}$)**	**Standard deviation**
0.2	15.401	0.456	9.1723	0.603
24	15.499	0.225	8.4583	0.521
55	14.503	0.357	6.3902	0.845
78	14.355	0.275	6.2344	0.364
110	13.878	0.201	5.0051	0.567

6.4 Discussion

The rate-dependent nanomechanical properties of the interfaces in nacre and arthropod exoskeleton have been AFM mechanically studied in Chapter 5 and previous sections in Chapter 6. A further comparison of the rate-dependent mechanical properties of different biological composites, while generally difficult due to the lack of data, can be made by considering the nanoscale interfacial shear test between non-collagenous proteins (NCPs) and mineralized collagen fibrils (MCFs) from the work of Hang et al. (175). Antler bone displays considerable toughness through the use of a complex nanofibrous structure of MCFs bound together by NCPs. While the NCP regions represent a small volume fraction relative to the MCFs, significant surface area is evolved upon failure of the nanoscale

interfaces formed at the NCP-MCF boundaries. The mechanical properties of the nanoscale interfaces between the MCFs were investigated using the same AFM mechanical testing technique as has been applied to nacre and arthropod exoskeleton here but by pulling out individual MCF from NCPs to give interfacial shear, as shown in Figure 6.7.

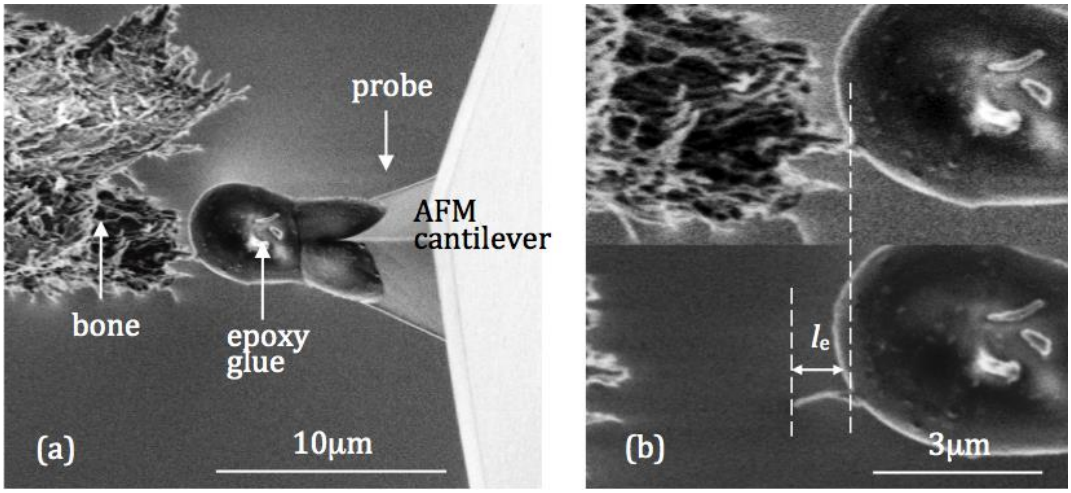

Figure 6.7 SEM micrographs showing (a) an AFM probe containing glue at its apex attached to an individual MCF partially embedded in a fibril bundle at the fracture surface of antler bone and (b) higher magnification image showing the pulled out fibril of embedded length l_e (175).

Pullout of individual MCFs using the Attocube AFM within the SEM chamber shown in Figure 6.7 produced resultant mechanical information during progression of the pullout test as shown in Figure 6.8. The mechanical properties of the NCP interfacial region around the MCF can be calculated by recording the force applied to the MCF by the AFM system. As shown in Figure 6.7, a force F is applied at the free end of MCF protruding from the bone material. The pullout force increased linearly with progression time of the experiment until a maximum force, F_p, was reached, which

caused failure of the MCF-NCP interface and a rapid drop in the force *F* exerted by the AFM until the MCF was separated from the bone sample.

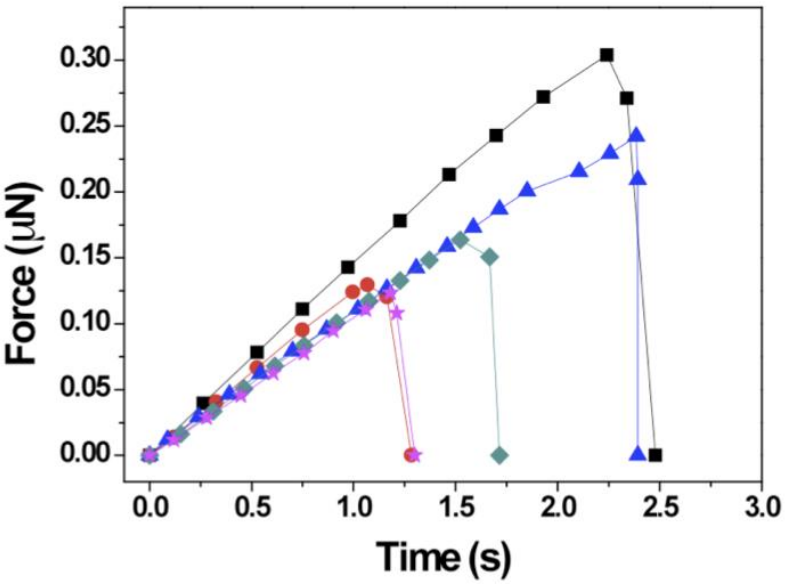

Figure 6.8 Plot showing the force applied to the partially exposed MCF during pullout against progression time for the pullout experiment. The force increases linearly with progression time until a maximum force F_p is reached, which causes failure of the interface and rapid separation of the MCF from the bulk bone sample. Curves correspond to pullout velocities of 2.30 μm·s^{-1} (■), 1.47 μm·s^{-1} (▲), 1.18 μm·s^{-1} (◆), 1.03 μm·s^{-1} (●) and 0.61 μm·s^{-1} (★) (175).

The strength of the interface between the MCF and surrounding NCP is characterized by the interfacial shear strength (τ) and is calculated from the maximum force applied to the exposed MCF to cause pull-out from the surrounding NCP using the force balance:

$$\tau = \frac{F_p}{\pi D l_e} \qquad \text{Equation 6.1}$$

where D is the fibril diameter and l_e is the length of fibril embedded within the bone. Solving Equation 6.1 using the maximum pull-out force results shown in Figure 6.8 gives a calculated MCF-NCP interfacial shear strength $\tau = 0.65 \pm 0.15$ MPa. To further explore the rate-dependent interfacial failure mechanism, various loading rates were examined to understand the dynamic behaviour of antler bone. The rate-dependent failure of the MCF-NCP interface can be evaluated by controlling the displacement velocity of the pullout experiment. Figure 6.9 shows the variation in the interfacial shear strength over a range of pullout velocities. The physiological loading rate for antler bone is approximately 1 $\mu m \cdot s^{-1}$ derived from strain rate of $\sim 1.6\ s^{-1}$ reported in previous literature (7) and is within the range of pullout velocities examined in Figure 6.9. The rate-dependent mechanical behaviour at the MCF-NCP interface highlights a clear increase in the interfacial shear strength with decreasing pullout velocity as shown in Figure 6.9, with detailed experimental results displayed in Table 6.3. Thus, the MCF-NCP interface is shown to be both relatively weak but exhibiting rate-dependent mechanical behaviour. This rate-dependent interfacial shear behaviour has a similar trend to those of nacre and arthropod exoskeleton, showing a weakened interface with increasing loading rate. The interfacial structures of these biological composites and their physiological loading conditions affect their interfacial shear behavior, but the relationships among them are still unclear and need further discussion.

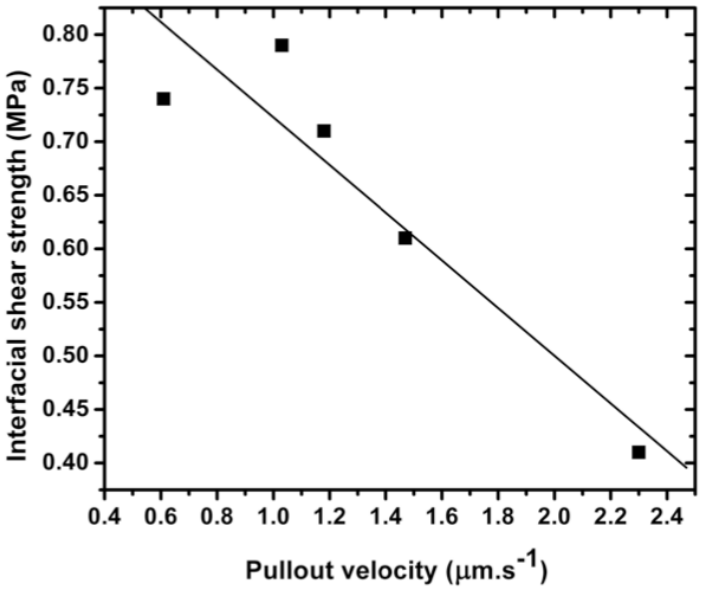

Figure 6.9 Plot of the variation in the MCF-NCP interfacial shear strength, calculated using Equation 6.3, with pullout velocity. A simple linear trend line highlights the increase in interfacial shear strength with decreasing pullout velocity (175).

Table 6.3 Data showing the fibril geometry, the resultant pullout behaviour including the work done and interfacial shear strength (τ), as well as interfacial fracture energy (γ) when pulling MCF from NCPs at various velocities (175).

l_e (nm)	Diameter (nm)	Work ($\times 10^{-14}$ J)	τ (MPa)	γ (J·m^{-2})	Pullout velocity (μm·s^{-1})
700 ± 35	168 ± 4	7.89 ± 0.12	0.61 ± 0.06	0.21 ± 0.02	1.47
510 ± 26	102 ± 3	2.96 ± 0.04	0.71 ± 0.07	0.18 ± 0.02	1.18
740 ± 37	110 ± 3	7.00 ± 0.10	0.74 ± 0.07	0.27 ± 0.03	0.61
880 ± 44	121 ± 3	6.03 ± 0.11	0.41 ± 0.04	0.18 ± 0.02	2.30
540 ± 27	81 ± 3	2.93 ± 0.07	0.79 ± 0.08	0.21 ± 0.03	1.03

To have a general overview of the interfacial structures and rate-dependent mechanics of nacre, arthropod exoskeleton and antler bone as we have studied,

Table 6.4 summarizes their rate-dependent interfacial mechanical structures and properties obtained from experimental results for further comparison and discussion. The width values (w) of the interface in nacre, arthropod exoskeleton and antler bone are derived from direct SEM sample imaging and previous literature (6, 36, 46, 92, 99, 106, 112, 175). The width of the inorganic-organic interface between adjacent mineral tablets in nacre is around 20 – 30 nm (36, 92). The width of the interface between fibre bundles at adjacent exocuticle layers is ~3 nm (99, 106, 112) while the width of the small space between MCFs in antler bone is ~1 – 2 nm (6, 46, 175). The average interfacial strength (τ_A) of the three biological composites are obtained from the nanoscale interfacial shear test detailed in Chapter 5 (nacre), Chapter 6 (arthropod exoskeleton) and the work performed by Hang et al. (175) (antler bone) respectively. The detailed values for each interface are presented in Table 6.4. We also find out that there is a potential relationship about the ratio of w and τ_A (w/τ_A) and is also shown in Table 6.4. The unit of the w/τ_A value is defined $m^3 \cdot N^{-1}$. This value will be further discussed in the following paragraph. Considering the varied interfacial strength at different loading rates for all the three biological composites, here we define a shear strength decrease rate (SSDR) as the change in the interfacial shear strength divided by the increase of loading rate that caused this shear decrease. The unit of SSDR is defined $N \cdot s \cdot m^{-3}$. Finally, the physiological loading rates (PLR) (s^{-1}) are obtained from literature for nacre (81), arthropod exoskeleton (8, 109) and antler bone (7) to establish a potential relationship among the rate-dependent interfacial mechanics of these biological systems and their physiological loading conditions.

Table 6.4 Structural and rate-dependent mechanical properties of the interface in nacre, arthropod exoskeleton and antler bone, with their physiological loading rates indicated.

Sample	**Exoskeleton**	**Nacre**	**Antler**
w **(nm)**	3	20 - 30	1 - 2
τ_A **(MPa)**	14.7 ± 0.78	36.5 ± 1.45	0.65 ± 0.15
w/τ_A **(×10^{-15} m^3·N^{-1})**	~0.2	~0.68	~2.3
SSDR (×10^{10} N·s·m^{-3})	1.7	4.2	18.5
PLR (s^{-1})	~10^6	10^2 - 10^3	~10^0

The width of the interface (w) controls the mobility of the organic phase in the interface. A wider interface provides more space for organic mobility and less confinement of interfacial polymers, while a narrower interface applies greater confinement of interfacial polymers. Furthermore, the shear strength of the interface (τ_A) adjusts the confinement that the interface could apply to the interfacial organic phase. A higher interfacial shear strength indicates an interfacial phase with greater confinement (less mobility) while a lower shear strength indicates the interfacial phase with less confinement (more mobility). Therefore, the w/τ_A value indicated in Table 6.4 represents the confinement of the interface in these biological systems. Higher w/τ_A value provides less confinement of the interface while lower w/τ_A value provides greater confinement. The w/τ_A value and the shear strength decrease rate (SSDR) as shown in Table 6.4 indicate a positive relationship, also plotted in Figure 6.10. This positive relationship proves that when the biological interface is more confined with lower w/τ_A value, the polymers within the interface must be more rigid, less mobile and less sensitive to varying loading rates, therefore

resulting in lower SSDR under this circumstance. Conversely, less confined interface with higher w/τ_A value is more flexible and rate dependent, with higher SSDR observed. The mobility of confined organic polymers within the interfacial region is therefore more instructive in determining rate-dependent mechanical properties than conventional approaches based on classical static theories such as shear-lag (1).

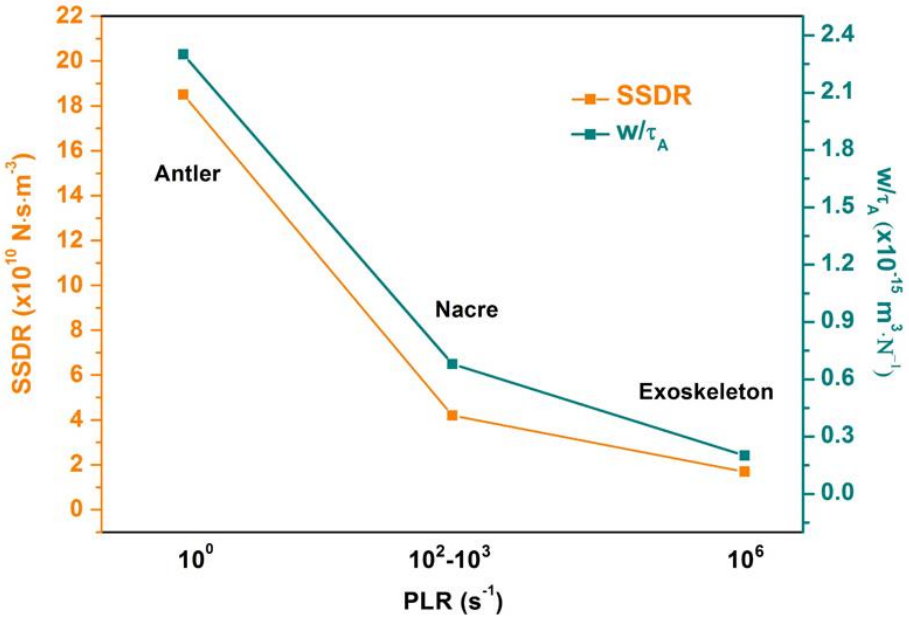

Figure 6.10 Plot showing the inverse relationship between the physiological loading rate (PLR) and the shear strength decrease rate (SSDR) and w/τ_A value among the biological systems of antler bone, nacre and arthropod exoskeleton. The left y-axis indicates the shear strength decrease rate of the three biological composites while the right y-axis indicates the w/τ_A value of the three biological composites.

Considering the physiological loading rates these biological composites experience in their real life as shown in Table 6.4, we find out that biological composites that adapt to relatively high dynamic stresses appear to have lower w/τ_A value whereas the opposite is true for lower loads and rates. A relatively fast loading rate, as occurs

during impact, is expected to rapidly develop shear or other stresses at the interface. A potential explanation is that a biological interface with lower w/τ_A value would have more confinement along the interface and stronger mechanical connection between two reinforcements. In this circumstance, the applied stress would be transferred to reinforcements through shear along the interface more effectively in a short time than an interface with higher w/τ_A value, dissipating a relatively large amount of mechanical energy in this process. The results showing the inverse relationship between physiological loading rate and w/τ_A (inverse relationship with interfacial confinement) as shown in Figure 6.10 supports this point of view. Molecular mobility in the interface may thus be tuned to a specific external time-scale of loading through interfacial width and polymer confinement.

6.5 Summary

In this chapter, the interfacial shear behaviour of the arthropod exoskeleton under a range of loading rates was investigated using the same experimental methodology as applied on nacre in Chapter 5. Results indicated a decrease in arthropod interfacial strength with increasing loading rates, highlighting a potential damage volume enhancement as observed in nacre with such interfacial weakening. General interfacial mechanical behaviour within biological composites was explored by comparing interfacial behaviour from nacre and arthropod exoskeleton to the interfacial shear behaviour of the NCP-MCF interface in antler bone from literature (175). All the three biological composites exhibited a weakened interface with increasing loading rates, but the biological interface with less confinement

(characterized with a larger w/τ_A value) showed a shear strength more sensitive to varying loading rates and appeared to adapt to less dynamic physiological loading conditions. The results and discussion in this chapter highlight the potential relationship between biological structural designs and the physiological loading conditions these biological systems experience.

Chapter 7 - Mechanical Properties of Graded Tendon-to-Bone Attachment Interfaces

7.1 Introduction

Connecting dissimilar materials is a fundamental challenge because of stress concentrations that can arise at their interfaces (208). Interfacial stress concentrations can contribute to material failures at levels of mechanical loads that are too small to cause failure in either material individually (209). 'Functionally graded' material systems that interpolate spatially between properties of two materials are often considered to reduce stress concentrations in engineering and medical applications, ranging from semiconductor thin films to prosthetic joints and limbs (210-212).

In nature, a graded material exists between the unmineralized 'soft' and mineralized 'hard' tissues (138, 213, 214), for example, at the shoulder's rotator cuff tendon-to-bone attachment, as shown in Figure 7.1. Here, tendon attaches to bone through a

fibrocartilaginous transition zone, known as the 'insertion site', that presents a continuous spatial grading in mineralization and organization of the underlying collagen fibres (143). Previous work suggest that this attachment mechanism might exist in other tensile connections such as ligaments (215) and menisci (216). Whereas engineering practice would be to interpolate between the mechanical properties of tendon and bone, experimental evidence indicates that grading at the rotator cuff insertion site produces a soft tissue region that is more compliant than either tendon or bone (217).

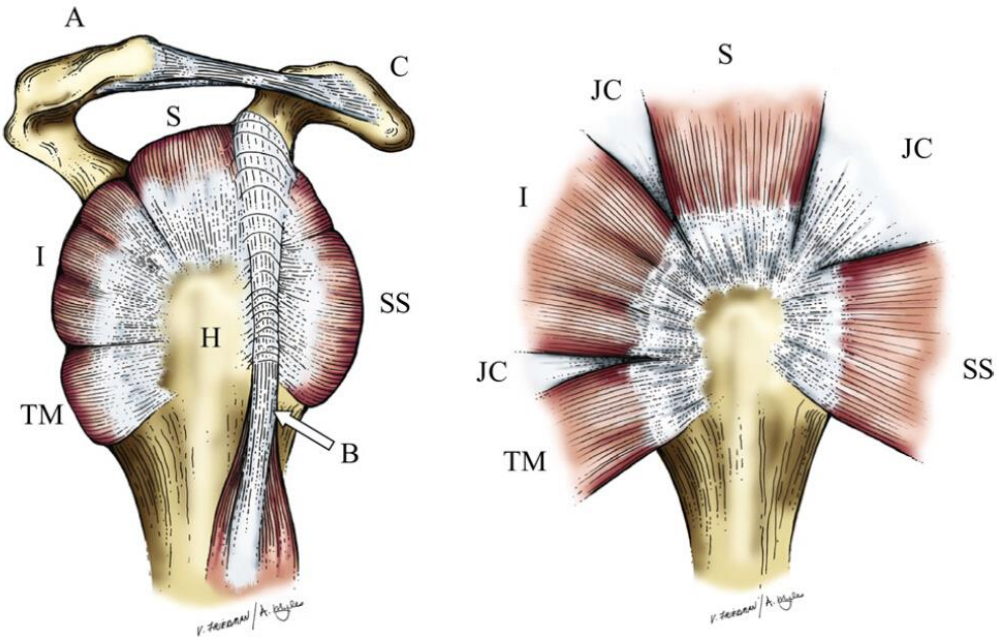

A: acromion, C: coracoid process, H: humeral head, B: biceps tendon, JC: joint capsule
TM: teres minor tendon, I: infraspinatus tendon, S: supraspinatus tendon, SS: subscapularis tendon

Figure 7.1 The rotator cuff as viewed from the side (i.e., the lateral view). Tendons are shown in white, muscles in red, and bones in tan. The rotator cuff tendons (TM, I, S, and SS) wrap around the spherical humeral head (H) (left panel). Removing the overlying structures (A, B, C) and unwrapping the rotator cuff tendons reveals the axisymmetric geometry of the tendons and their bony insertions (right panel) (218).

Tendons and ligaments attach to bone across transitional tissue interfaces that are several micrometres to millimetres in thickness. The interface, termed the 'enthesis', is classified as either fibrous (e.g., medial collateral ligament to tibia enthesis) or fibrocartilaginous (e.g., supraspinatus tendon to humeral head enthesis) (135, 219, 220). The fibrocartilaginous enthesis contains a functionally graded transitional tissue, with variations in extracellular matrix structure and composition giving rise to variations in mechanical properties across the interface (138, 215, 221-223). Tendon consists primarily of type I collagen with small amounts of decorin and biglycan. Bone consists of heavily mineralized type I collagen. Collagen fibres are well aligned in tendon. However, the collagen fibres become less organized as they insert into the bone (145). At the tendon enthesis, a fibrocartilaginous transitional zone is present that is rich in type II collagen and aggrecan produced by fibrochondrocytes, which have a rounder morphology compared to spindle-shaped tendon fibroblast cells and are phenotypically similar to chondrocytes. Within the transitional zone of the rat supraspinatus tendon enthesis, an increase in mineral relative to collagen has been observed through the transition from tendon to bone (143). These variations in structural and compositional properties result in graded mechanical behaviour that contributes to an efficient transfer of muscle load from tendon to bone (147, 218, 224). The gradient in mineral content is believed to be particularly important for limiting stress concentrations at the mineralized interface.

In an injury-and-repair scenario, the original graded transitional tissue of the fibrocartilaginous insertion is not recreated after the tendon is surgically reattached to bone. Surgical reattachment leads to a more abrupt interface of mechanically

inferior and disorganized scar tissue (124, 130, 225). The loss of a gradual mineral transition likely contributes to the decreased mechanical performance of the load-bearing interface and results in frequent re-ruptures. For example, surgical repair of massive rotator cuff tears, which relies on tendon-to-bone healing for success, has a re-tear rate of up to 94% (126, 127). Therefore, understanding the counterintuitive biophysics of the natural attachment is important for medical practice and for biomimetic design.

The micrometre length scale provides an opportunity to study the tendon-to-bone attachments as a composite and, thus, explore the synergies between material components that define resultant mechanical function. Although millimetre length scale mechanical testing has elucidated some of the mechanisms of load transfer described above (226, 227), few efforts have attempted to examine the microscale mechanics. Previous work has loaded tendon-to-bone specimens in uniaxial tension and attempts have been made to measure local deformations (226). This technique has described tissue-level mechanics, but interpretation of results has been limited by the complex attachment geometry, interference from other tissues (e.g., the tendon sheath), and difficulty in identifying the exact location of failure.

In this chapter, we employed atomic force microscopy (AFM) in conjunction with scanning electron microscopy (SEM) to perform tensile tests on microscale beams of tendon-to-bone attachments fabricated using focused ion beam (FIB). The approach of preparing microscale beams of biological sample and subsequent mechanical testing using in situ AFM as described in Chapter 3 is therefore applied

to an interfacial region with graded mechanics, as opposed to the discrete interfaces examined in Chapter 5 and 6. This combined SEM-FIB-AFM technique allows for the first-ever visualization and mechanical testing of the micrometre-long transitional tissue between tendon and bone.

7.2 Materials and Methods

7.2.1 Animals

The use of animals and our procedures for this study were approved by the animal studies committee at Washington University (Protocol Number: 20100091) and all efforts were made to minimize suffering. The baseline animals were female CD-1 wild type (WT) mice (Charles River lab. Int., Inc.) aged 14 - 18 weeks. For the conditional Indian hedgehog (Ihh) signaling knockout (KO) experiments, ScxCre mice (228) were crossed with $Smo^{fl/fl}$ mice and aged to P56 (229). Indian hedgehog homolog signaling has been shown to play a role in enthesis development and maturation (230). The ScxCre/$Smo^{fl/fl}$ mice exhibit conditional knock out of Smoothened, a molecule required for Ihh responsiveness, at the tendon-to-bone attachment. These mice exhibit inhibited fibrocartilage mineralization and compromised tissue level biomechanics (230). Three WT mice and three KO mice were studied in this work.

7.2.2 Sample Preparation Using LCM

The sample preparation described in this section was performed in Washington University in St. Louis. The supraspinatus-humerus complex was dissected from the mouse sample detailed in Section 7.2.1 after immediate sacrifice. Care was taken to maintain the integrity of the supraspinatus tendon-to-humeral head interface. The dissected complex was cut down using a sharp scalpel blade to keep just the humeral head and part of the supraspinatus tendon. The sides of the anterior and posterior edges of the humeral head were also cut in order to provide a flat surface. This complex which includes the tendon-to-bone interface was then placed in the Optimal Cutting Temperature (OCT) compound and frozen at -80°C before further preparation. The OCT-embedded sample was cut into sections using a Cryostat. The sections were 20 - 30 μm in thickness and deposited onto a special Laser Capture Microscopy (LCM) tape which was stretched across a 1 cm diameter hole in the LCM plastic slides, as shown in Figure 7.2. Once sectioned, the slides were maintained at -80°C for further preparation.

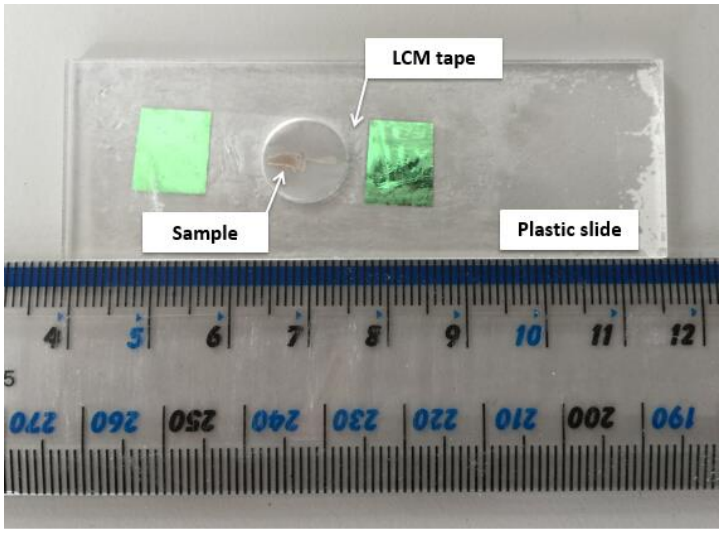

Figure 7.2 Optical photograph showing the tendon-to-bone attachment section deposited on the LCM tape stretched across the LCM plastic slide.

The frozen sections were thawed and imaged in the LCM. The tendon-to-bone attachment was identified and beams were cut spanning the tendon-to-bone interface. The beams were cut using the LCM laser, making sure that these beams were parallel to the collagen fibrils and spanned the mineralized and unmineralized fibrocartilage. This LCM laser cut resulted in beams with dimensions of 150 - 200 μm long and ~30 μm in width, as shown in Figure 7.3. In order to facilitate access to the beams for subsequent FIB fabrication, a relatively large hole (>1.5 mm) was cut around the beams so that the tendon-to-bone attachment section could be easily manipulated using scalpel blades and tweezers. Two to four beams spanning the mineralized and unmineralized fibrocartilage for each tendon-to-bone attachment section were cut depending on the dimension and quality of the section. Once the beams were successfully cut, the samples were refrozen at -80°C and shipped to Queen Mary, University of London (QMUL) on dry ice. Once received at QMUL, the samples were placed in the freezer at -80°C until further preparation.

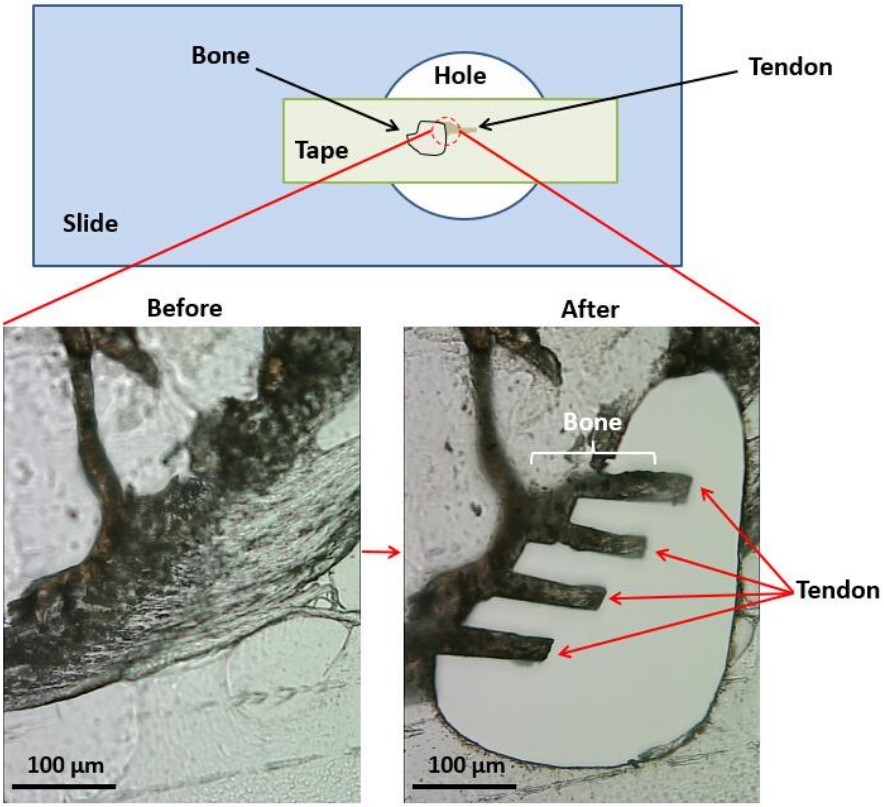

Figure 7.3 Optical images showing the section before LCM dissection and the tendon-to-bone attachment beam after the dissection, with schematic showing the tendon and bone part on the section.

7.2.3 Sample Preparation Using Cryo-FIB

FIB fabrication of the tendon-to-bone attachment beam sample was performed under cryo condition using the SEM-FIB dual-beam system as detailed in Chapter 3. The sample slide was removed from the freezer before FIB fabrication. The tendon-to-bone attachment beams with some of the surrounding tissue attached to the bone part were cut away from the rest of the slide using a sharp scalpel blade under an optical microscope in order to work with the beams exclusively. A 60° pre-tilt stage was attached to the cryo-stage using the OCT solution. A small piece of aluminum foil was then attached to the pre-tilt stage, also via the OCT solution. Finally the beam

sample was attached to the aluminum foil via the OCT solution. The beam sample was placed such that the beams extend beyond the edge of the pre-tilt stage and perpendicular to the direction of the tilt. Until this step, the sample was still attached with the LCM tape facing down. The cryo-stage with sample was then brought to cryo-temperatures by dipping into liquid nitrogen slush. The cryo-stage was continuously rotated in the slush for 2 minutes in order to guarantee that the stage was -130°C, which is the temperature of the pre-chamber and main cryo-chamber. The sample was then inserted into the pre-chamber of the SEM-FIB dual-beam system, as shown in Figure 7.4. In the pre-chamber, the sample was first brought to -90°C to sublime ice off the surface of the sample. Argon was subsequently pumped into the chamber and a thin layer of platinum/gold deposited on the sample through plasma sputtering. Once coated, the sample was further inserted into the main cryo-chamber for FIB fabrication.

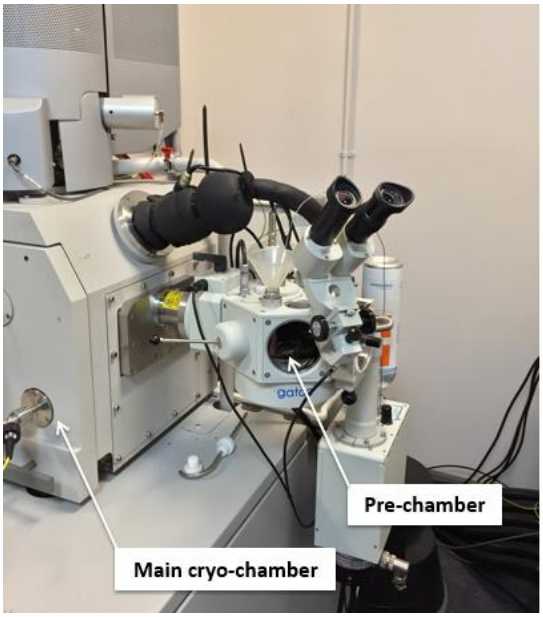

Figure 7.4 Optical photograph showing the pre-chamber and the main cryo-chamber of the SEM-FIB dual-beam system.

The sample was then cut using FIB by first positioning such that the top surface of the beams lies perpendicular to the direction of the ion beam. In this orientation the left and right sides of the beam could be removed with the ion beam at the voltage of 16 kV and 3 nA for initial milling. A lower voltage (16 kV) was applied here compared with the voltage (30 kV) applied for nacre and exoskeleton in order to minimize the damage FIB microscopy might cause on this soft tissue sample. Due to the potential drift caused from ion charging, similar protocol as described in Section 3.3 was carried out by multiple ion currents down to 0.5 nA for fine polishing. The width of the beam was reduced to a final dimension of ~3 μm. Once the left and right sides of the beam were removed, the sample was removed from the cryo-chamber and the stage was rotated 90°. The sample was then reinserted into the cryo-chamber and solid water sublimated as previously described. The side surface of the beam was positioned perpendicular to the direction of FIB so as to remove the top and bottom parts of the beam. During this process the LCM tape (attached to the bottom of the beam) and the platinum/gold coating were removed. The resultant beam had a final square cross-section of ~3 × 3 μm^2. Progression of sample preparation as observed with SEM from the initial irregular shaped laser trap sectioned sample to the final regular sample form after FIB is shown in Figure 7.5. The samples were then removed from the SEM chamber for subsequent AFM mechanical testing.

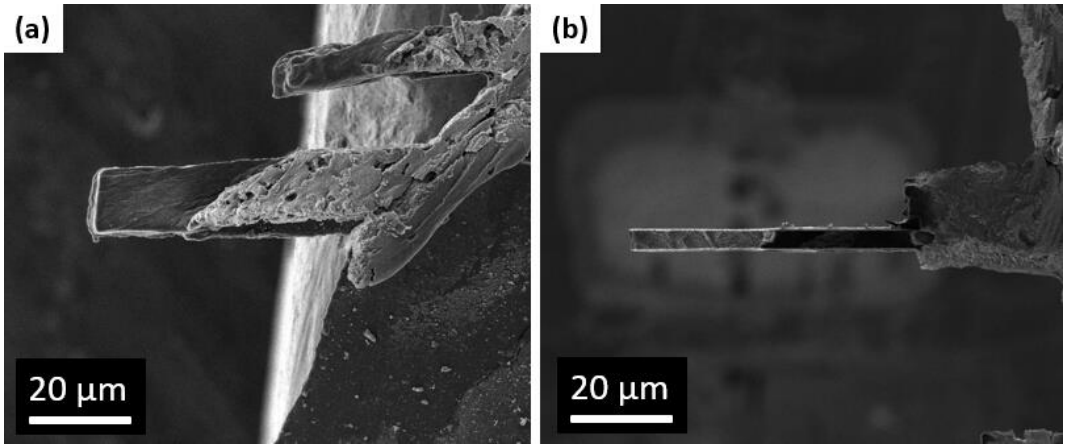

Figure 7.5 SEM imaging showing the tendon-to-bone attachment beam (a) before and (b) after FIB fabrication.

7.2.4 Compositional Study Using EDS

X-ray energy dispersive spectroscopy (EDS) microanalysis within the SEM (Inspect SEM, FEI Company, EU/USA) was used to investigate the proportion of the mineralized and unmineralized fibrocartilage on FIB-fabricated tendon-to-bone attachment beam. The proportion of the mineralized and unmineralized fibrocartilage in each beam is related to the mechanical properties of these beams and used as a maker for mechanical performance. Ten points with identical interval along the FIB-fabricated beam were EDS tested in order to determine the calcium contents along the beam.

7.2.5 AFM Tensile Testing

AFM tensile testing was performed on rehydrated samples using the same methodology applied to nacre and arthropod exoskeleton. Each tendon-to-bone

sample was fixed to a piece of aluminum foil with carbon tape since the OCT lacks adhesion at room temperature. Once attached, the aluminum foil and the sample were placed in a water vapour environment for rehydration as described in Section 4.2.1.

After hydration, the sample complex (sample + aluminum foil) was attached to the AFM sample stage via a piece of carbon tape. The sample was attached such that the FIB-fabricated beams extend beyond the edge of the sample stage in order to perform tensile test on the beams. A high-vacuum compatible adhesive (SEMGLU, Kleindiek Nanotechnik GmbH, Germany) was used in this experiment to attach the free end of the beam to the AFM tip in order to perform the tensile test. The SEMGLU hardens under electron beam irradiation using a high current electron beam on a small area whereas under relatively low imaging electron currents, the glue remains uncured and deformable. A small bead of SEMGLU was mounted on the tip of a thin wire placed besides and parallel to each individual tendon-to-bone beam to be mechanically tested. A FIB-flattened AFM tip with spring constant of 40 $N \cdot m^{-1}$ was mounted on the AFM system and positioned 30 μm ahead of the default position by the AFM software so that the AFM tip could retract backwards for tensile testing when attached firmly to the sample. The sample stage was then moved towards the AFM tip, which allowed contact of the tip to the SEMGLU as shown in Figure 7.6, followed by stage retraction so that a small amount of glue was retained at the apex of the FM tip.

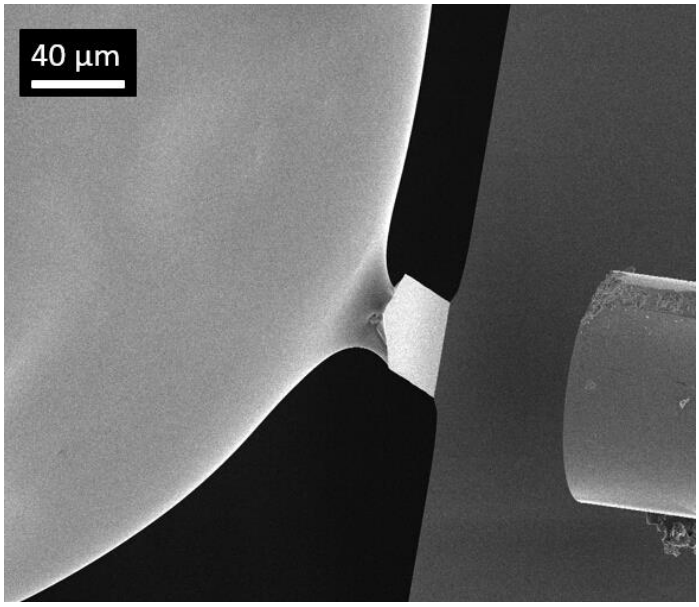

Figure 7.6 SEM imaging showing the AFM tip contact the SEMGLU bead.

The sample stage was then moved to contact the free end of the FIB-fabricated beam with the SEMGLU at the AFM tip apex. All steps were performed under the electron current of 93 pA to prevent the glue from hardening. Curing of the SEMGLU at the AFM tip-sample contact was achieved by focusing the electron beam onto the SEMGLU drop under a high electron current of 1.5 nA for approximately 10 minutes to ensure a strong bond between the tip and the beam. In this way, the FIB-fabricated tendon-to-bone attachment beam was firmly attached to the AFM tip prior to mechanical tensile testing. The AFM uniaxial tensile test to failure was then performed by retracting the AFM tip in a quasi-static manner at a loading rate of 0.1 $\mu m \cdot s^{-1}$, as shown in Figure 7.7. Tensile testing was the preferred mechanical testing configuration as this provided a similar stress condition to the native tissue state.

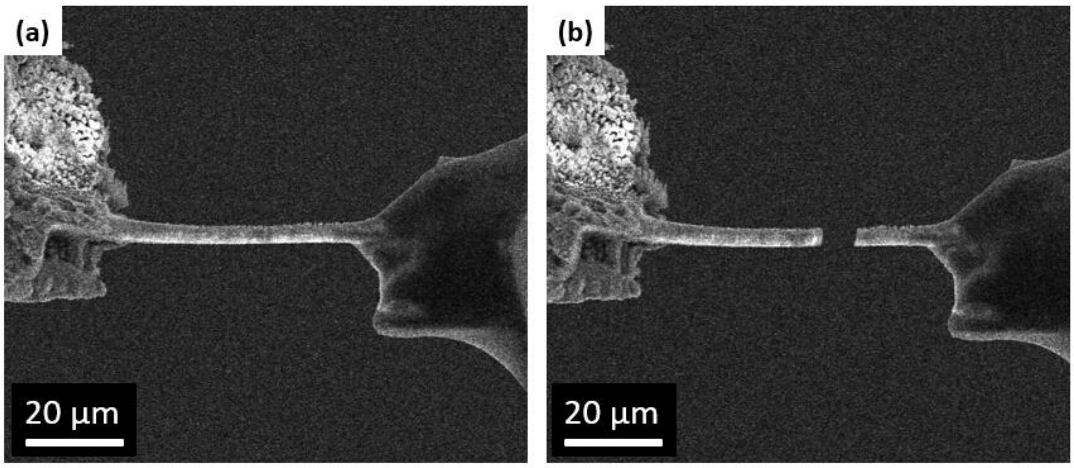

Figure 7.7 SEM images showing the AFM tensile test on tendon-to-bone attachment beam (a) before and (b) after failure.

7.3 Results

Figure 7.8 shows the stress-strain curves for nine successful tensile tests on five KO samples and four WT samples. Five KO samples were successfully tested on KO mouse No.1 (sample KO1-1 and KO1-2), KO mouse No.2 (KO2-1 and KO2-2) and KO mouse No.3 (KO3). Four WT samples were successfully tested on WT mouse No.2 (sample WT2-1, WT2-2 and WT2-3) and WT mouse No.3 (WT3). There was no successful tests achieved on WT mouse No.1. Sample KO3 and WT3 showed large plastic deformation stages with high strains of ~8.5% while the other samples showed a relatively linear deformation until ultimate failure at relatively small strains. The Young's moduli of the tensile tests were calculated from the linear region of the curves and detailed in Table 7.1 along with the failure stress and failure strain values. As shown in Table 7.1, the elastic modulus of the samples span a wide range from 1 GPa to 4.2 GPa while the failure strength of the samples span a relatively smaller range from 20 MPa to 60 MPa. The mechanical properties shown in Table

7.1 also indicate little significant difference in any of the mechanical properties between KO and WT samples, including failure strength, failure strain and the Young's modulus, which suggests that the Ihh KO did not affect the mechanical properties of the tendon-to-bone attachment at this tissue level. The average stiffness (Young's modulus) of the nine samples was ~2.6 GPa which is nearly 50 times higher than the values measured by tissue level testing (226). This difference in stiffness is likely due to scaling effects, particularly the small length scale samples being continuum whereas larger samples contain voids that are not considered when calculating mechanical properties based on forces acting on sample cross-sectional areas.

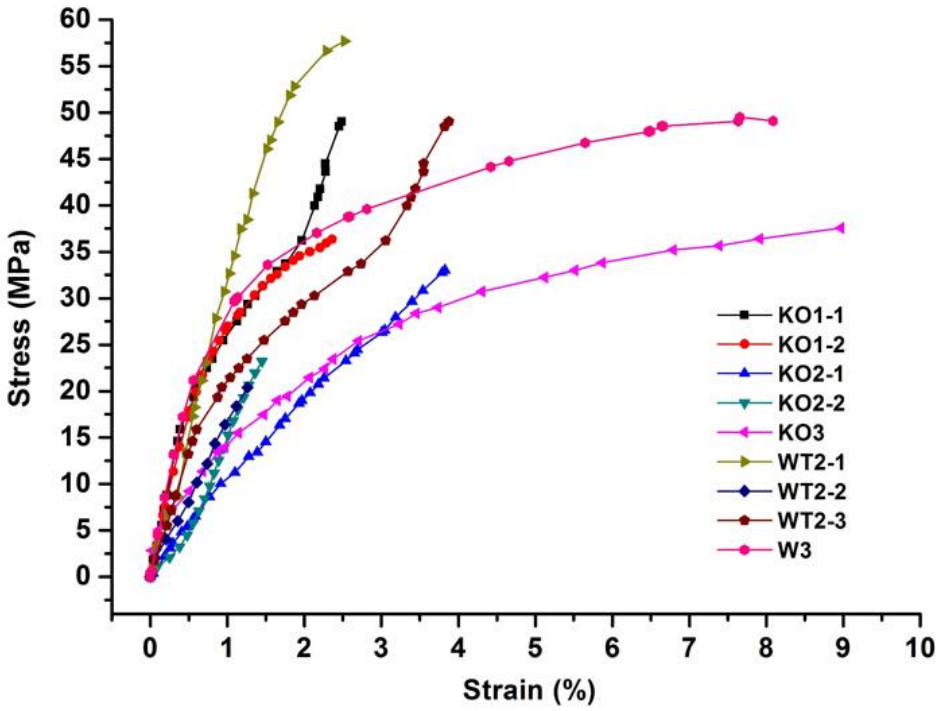

Figure 7.8 Tensile stress-strain curves for all nine successful tensile tests on five KO and four WT tendon-to-bone beam samples.

Table 7.1 Stress, strain and elastic modulus values for all the successful tensile tests.

Sample	Stress (MPa)	Strain (%)	Modulus (GPa)
KO1-1	49.03	2.48	4.13
KO1-2	36.34	2.36	3.32
KO2-1	33.01	3.83	1.05
KO2-2	23.21	1.45	2.25
KO3	37.56	8.97	1.08
WT2-1	57.70	2.52	3.21
WT2-2	20.39	1.26	1.58
WT2-3	49.03	3.88	2.65
WT3	49.08	8.09	4.16

The stiffness values varied between samples due to the variations in beam length and due to the ratios of mineralized to unmineralized tissue in each beam. The Calcium EDS signal was used to determine the amount of mineralized, unmineralized, and graded tissue in each beam, which is shown in Figure 7.9.

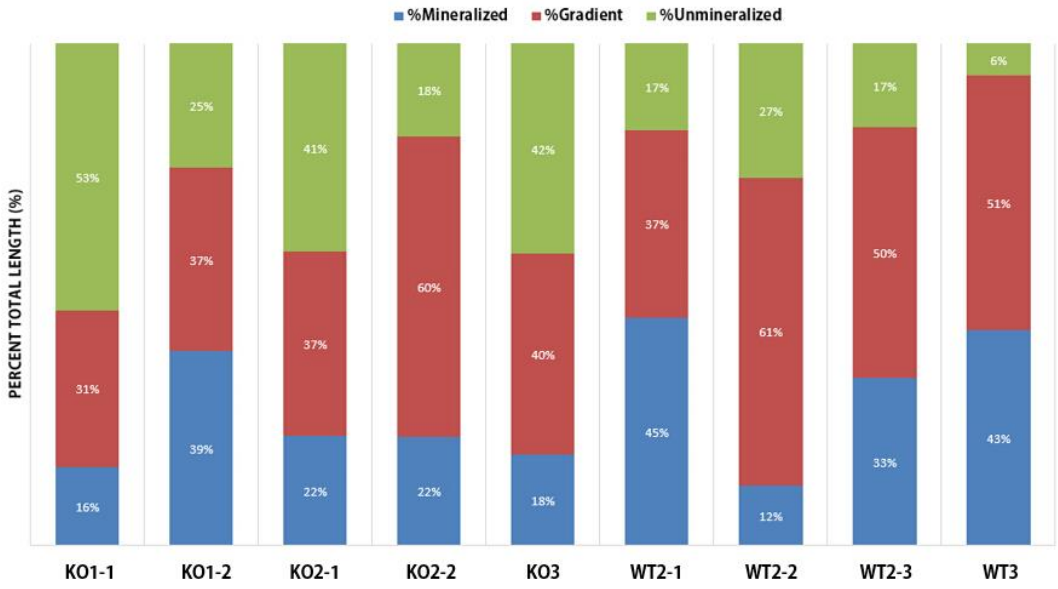

Figure 7.9 Plot of the relative percentage of mineralized, unmineralized and gradient regions for all of the beams tested. Values are determined from the EDS results.

7.4 Discussion

The variations in mineral content had significant effects on the measured modulus of the beams during tensile testing. The simplest test for determining the effects of the composition on the modulus of the beams is to use a simple law of mixtures. All of the beams have been FIB fabricated such that the beam length lies perpendicular to the direction of the gradient in mineralization and parallel to the preferential orientation of the collagen fibrils. Therefore, the three regions of mineralized, unmineralized and graded tissue can be considered as components set in series and modelled via the Reuss model:

$$E_{tot} = \left(\frac{V_M}{E_M} + \frac{V_U}{E_U} + \frac{V_G}{E_G}\right)^{-1} \qquad \text{Equation 7.1}$$

where V_M, V_U, and V_G are the fractions of mineralized, unmineralized, and graded tissue, and E_M, E_U, and E_G are the Young's moduli of each tissue. E_M was assigned 20 GPa and E_U was assigned 0.5 GPa respectively based on previous literature results (136, 218). The graded region was assumed to be linear and treated as a sum of small regions with linearly increasing Young's moduli. Using the Reuss model, the calculated modulus values of the beams matched the experimental results reasonably well as shown in Figure 7.10.

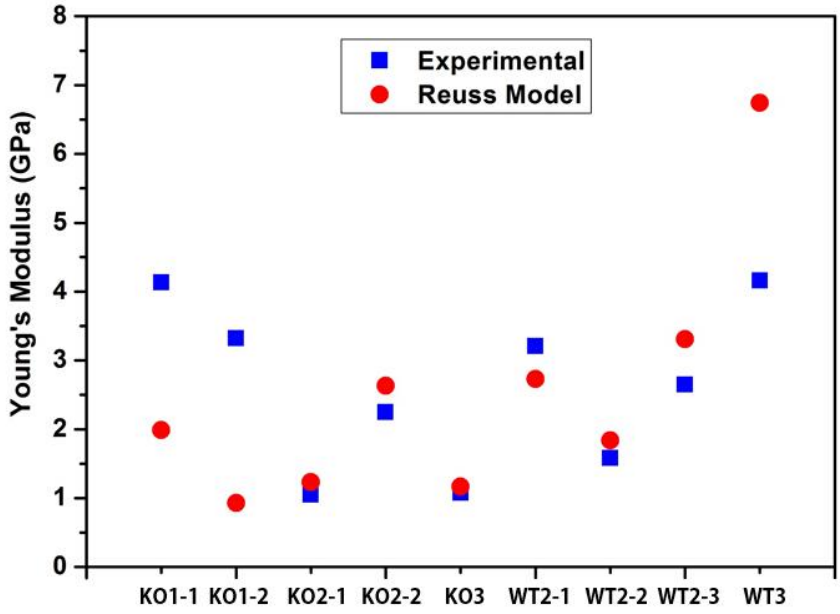

Figure 7.10 Plot of the experimental moduli in blue vs. modelled moduli in red of all of the samples using the Reuss model. Note that the Reuss model matches the experimental results reasonably well except for a few exceptions: both KO1 samples and WT3.

Detailed analysis of the recorded videos of the tensile tests revealed that the three beams exhibiting the largest errors in comparison to the modelling results appeared to undergo bending as well as tensile forces during loading. In order to account for

these bending changes, a more complex bending model that included a force acting non-parallel to the long access of the beam was developed. The bending model assumes a rule of mixtures (Reuss model); that the three tissue types are in series and that the graded region exhibits a linear change in modulus between the other two tissues. However, instead of stopping there, the bending model assumes that the force is not necessarily applied directly parallel to the long axis of the beam but may be at a small angle (<15°), as shown schematically in Figure 7.11. With a non-parallel applied force, there are now both a horizontal displacement parallel to the length of the beam and a vertical one perpendicular. Both of these values must be calculated to determine the Young's modulus of the beam. The details of how the horizontal (v_1) and vertical (v_2) displacement are measured is detailed in the appendix.

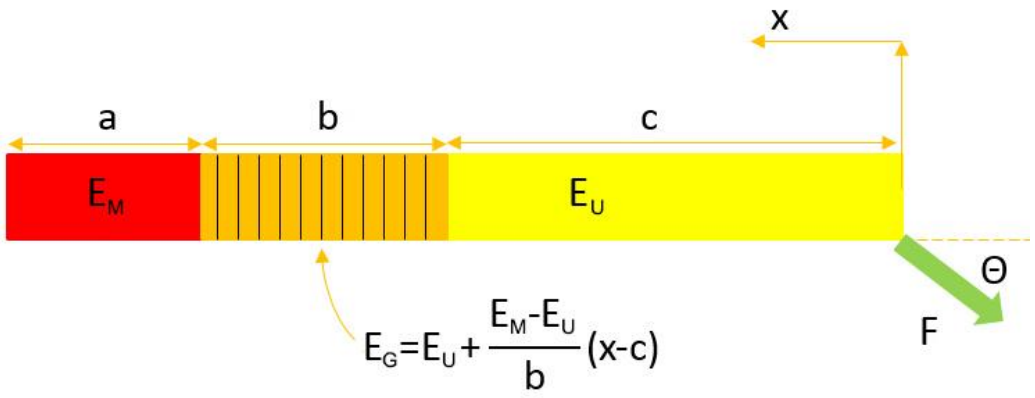

Figure 7.11 Schematic of the bending model. The beam is still composed of three regions: mineralized, unmineralized and graded regions of lengths a, c and b. The modulus of the graded region (E_G) is a linear extrapolation between the moduli for the mineralized (E_M) and unmineralized (E_U) regions. This bending model can be used for both parallel loading ($\theta = 0$) and off-axis loading ($\theta \neq 0$).

The calculation of the horizontal displacement, v_1, was calculated from the following equation:

$$v_1 = \frac{Fcos(\theta)}{A}\left(\frac{c}{E_U} + \frac{a}{E_M} + \frac{b}{E_M - E_U}\right)(ln\ E_M - ln\ E_U) \qquad \text{Equation 7.2}$$

Where F is the force applied on the beam calculated from the AFM system and A is the cross-sectional area of the beam. The length and cross-sectional area of the beam was measured from direct SEM imaging. Mineral content from EDS analysis was input into the model to determine the amount of mineralized (a), unmineralized (c) and graded (b) regions in the beams. The angle θ at which the beams were loaded was determined and measured from the video recorded for each tensile test. Most of the beams were loaded at an angle of 0^o but a few were loaded at angles up to 10^o. The vertical displacement, v_2, was calculated using the composite beam bending theory by solving the boundary equations at the interfaces between the three tissue types. With known v_1 and v_2 we can calculate the total displacement of the beam according to the equation:

$$\Delta = \sqrt{v_1 + v_2} \qquad \text{Equation 7.3}$$

The total Young's modulus of the beam can then be determine from the equation:

$$E = \frac{FL}{\Delta}\left(\frac{\cos^2\theta}{A^2} + \frac{\sin^2\theta L^4}{9I^2}\right)^{\frac{1}{2}} \qquad \text{Equation 7.4}$$

Where I is the moment of inertia and L is the total length of the beam. All the other parameters have been illustrated after Equation 7.2. With this bending model the error was decreased in the fitting between the model and the experiments, as shown in Figure 7.12.

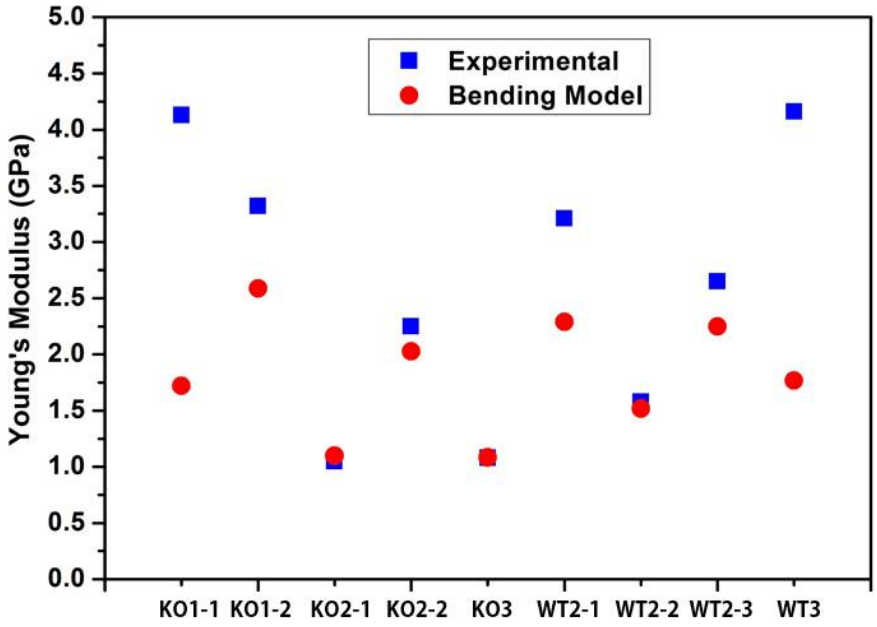

Figure 7.12 Plot of the experimental moduli in blue vs. modelled moduli in red of all of the samples using the bending model. By accounting for the difference in the orientation of the load, the errors are decreased in the fitting between the model and the experiments.

In addition, the E_M and E_U values were varied within reasonable ranges and found that the value of E_M = 25 GPa and E_U = 0.5 GPa optimized the system to minimize error. This fact was true both for the WT and KO samples. The error was decreased from 32% to 22% even though sample KO1-2 and WT3 still have high errors (~50%). Upon further inspection of the recorded videos of the tensile tests, it was found that both sample KO1-2 and WT3 exhibited clear bends in their structures before loading. These bends and deviations in the beam made it impossible to accurately analyse the beam with this bending model. This is evident, that in most cases, this model can be successfully used to model the mechanics of a beam under simple loading conditions. In cases where the beams are no longer "beam-like", the model falls apart.

If we eliminate the errors for the two oddly shaped beams (KO1-2 and WT3), the average error with the bending model drops to 13 ± 10%.

Our work used a simple beam bending and rule of mixtures based model to predict the modulus of the tendon-to-bone beams. What our results show is that the experimentally measured modulus of the beams do not change with the Ihh KO as compared to the WT samples. In addition, the model can be used to account for changes in composition across the beam and to predict the beam modulus and in return the tissue Young's modulus. This suggests that the significant change in the amount of mineralized fibrocartilage in cases of Ihh KO causes a structural defect, but not a tissue level one. It appears that the modulus is unchanged in the collagen and mineral at the nanoscale and the microscale although it causes structural differences that affect the organ level mechanics. This is important in situations where Ihh may be impaired and the enthesis cannot mineralized correctly. Changes in mineralization due to Ihh KO may cause increased fracture risk compared to the WT samples and this should be treated at the organ level and not the tissue level.

Our results also show that the gradient region can simply be modelled as a series of three different tissues: mineralized, unmineralized and graded regions. The ease of application of this simple model suggests that the complex structure of the attachment site may easily be described as three tissues in series. This is extremely important in tissue engineering of interfacial scaffold. Scaffolds can be created according to this basic model, varying the collagen content and mineralization to fit these natural biological structures.

7.5 Summary

In summary, the microscale beams of the tendon-to-bone attachments fabricated using FIB were successfully tensile tested using the custom built AFM system in the SEM-FIB dual-beam system. Then we applied a beam bending and rule of mixtures based model to successfully model and predict the moduli of the tendon-to-bone beams. The mechanical properties of KO and WT samples showed no evident difference between each other, indicating that the knockout of Ihh didn't changed the collagen and mineral properties at the microscale and nanoscale although it caused structural differences that affect the organ level mechanics.

Chapter 8 - Conclusions and Future Work

8.1 Summary of the Thesis

The importance of interfaces in biological systems with mechanical functions operating under dynamic loading conditions is identified in this work. An approach of considering biological structures as composites required definition of composite materials established using typical engineering concepts described in Chapter 2, with the importance interfaces in defining overall composite behaviour highlighted. The most notable deviation exhibited by biological composite structures over engineering composites is the use of hierarchical architectures formed across multiple length scales. The formation of structural biological composites was therefore reviewed and applied to describe the resultant structures-mechanical function of the three diverse biological composites studied in this thesis: nacre of abalone shell, arthropod exoskeleton of mantis shrimp and tendon-to-bone attachment in humeral head of mouse. Toughness was seen to be a critical mechanical properties that was of principle importance in the function of these biological structures. However, the intrinsic toughness of interfaces in these

biological composite and their behaviour under dynamic loading conditions, which is generally ignored in composite mechanicals, was found to be lacking. The literature review in Chapter 2 was of particular importance for justifying the experimental work of exploring toughness of these structural biological composites at the sub-micron length scale.

Chapter 3 reported on an overview of the experimental methodologies applied throughout the thesis for investigating interfacial toughness of biological samples at small length scales, including sample preparation processes and the nanomechanical testing setup as well as data collection and analysis. The approach taken was to exploit preparation methods that isolate a specific structural feature in a complex biological material so that further mechanical testing could be used to evaluate toughness, and thus the importance of the feature, with respect to the larger scale biological structure. Therefore, novel techniques combining focused ion beam (FIB) for small length scale biological sample preparation, scanning electron microscopy (SEM) for in situ imaging and an custom built in situ atomic force microscopy (AFM) for mechanical testing were extensively employed, with these techniques described in detail in this chapter before applications in subsequent experimental chapters.

The SEM-FIB-AFM technique introduced in Chapter 3 was applied in Chapter 4 to perform small-deflection AFM bending test on both dry and hydrated nacre samples in a variety of environments to study the effect of potential sample dehydration, and thus modification of the mechanical properties of the biological structures, due to

SEM vacuum. A lack of environmental influence on the mechanical properties of the micron-sized nacre beams was observed, which indicated that the water content is constant in all mechanical testing cases. Biological samples exposed to high vacuum would be expected to provide the largest removal of water but similar elastic modulus of both dry and hydrated nacre beams in three different environments showed that the vacuum driving force was not sufficient to remove the water within the tested nacre volumes. The discrete volumes tested in this work must therefore contain bound water, which is not removed in any of the environmental conditions. We can conclude that the environmental conditions used for mechanical testing of micron-sized nacre beams are not evasive within the timescales examined in this chapter.

Chapter 5 employed a nanoscale interfacial shear test to evaluate the inorganic-organic interfacial properties in nacre using the in situ AFM system within SEM. Decreasing interfacial shear strength and work of fracture was found with increasing loading rates. Entangled long molecules and electrostatic attractions along the inorganic-organic interfaces are regarded as two potential mechanisms explaining this interface weakness under high loading rates.

Understanding of interfaces in biological structures was extended to arthropod exoskeleton, selected due to a similar layered structure to nacre but a required toughness operating at high loading rates. Chapter 6 showed a weakening of interfaces with increasing loading rates in arthropod exoskeleton, thus displaying a comparable behaviour to nacreous structures. The interfacial mechanics in nacre

and arthropod exoskeleton were additionally compared to interfacial shear behavior in antler bone from literature (175) to propose a general rate-dependent interfacial mechanical behaviour for these biological structures. All the three biological composites showed a weakened interface with increasing loading rates, but the biological interface with less confinement (characterized with w/τ_A values) displayed a shear strength more sensitive to varying loading rates. Biological composites with weak interfacial shear strengths and relatively wide interfaces are thus expected to show significant loss in shear strength with increasing loading rates. Biological structures that experience relatively high loading rates or, perhaps more importantly, a variation in loading conditions potentially confine their interfaces to restrict significant resultant interfacial weakening at higher loading rates while maximizing damage zones for toughness. Resultant biological structural designs are expected to be optimized somewhat towards the physiological loading rates experienced by the organism, with the experimental observations here providing evidence of such structure-function relationships.

Finally, Chapter 7 evaluated mechanically graded tendon-to-bone interfaces, highlighting the flexibility of the experimental approach used. Microscale beams of tendon-to-bone attachment fabricated using FIB were successfully tensile tested using in situ AFM. An analytical model based on a simple rule of mixtures was used to predict the elastic moduli of the tendon-to-bone beams by consideration the spatial compositional variations within the larger interfacial regions, again providing a more complex-structure function relationship in a biological composite.

8.2 Future Work

The work presented in the thesis is pioneering in direct mechanical study on the interfaces of a wide range of structural biological composites at small length scales and provides a number of future opportunities. Specifically, mechanical testing usually requires a large number of samples tested but a larger statistical data set is difficult to achieve in this study due to the difficulty in nanoscale manipulation and performing AFM mechanical testing. Although every experiment in this thesis was performed on at least 3 to 6 samples, which meets minimum statistics requirement, larger data sets would provide information on the material variation in these studied structural biological composites.

Furthermore, due to the limitation of time consumption and sample preparation, the mechanical properties of the tendon-to-bone attachment were not studied under varying loading rates, but the dynamic mechanical information of the tendon-to-bone attachment would be obviously desirable considering the complex loading conditions the tendon-to-bone attachment experiences in real life. The microscale tendon-to-bone attachment would be tensile tested at varying loading rates in the future. Achieving the dynamic mechanics of the tendon-to-bone attachment would provide a more comprehensive understanding of the tendon-to-bone mechanics and a better guidance for medical practice and biomimetic design.

Finally, Finite element modelling could be potentially applied to the nanoscale interfacial shear tests on these biological composite structures. The combination of the nanoscale behaviour obtained from experimental results and larger scale modelling would therefore provide a complete understanding of the dynamic mechanical properties of these biological composites, which is still a barrier in the understanding of composite materials incorporating nanoscale constituents as commonly found in natural design.

8.3 Major Findings of the Thesis

- A custom built in situ AFM nanomechanical testing method established in this thesis was proven to be suitable for mechanically testing a wide range of structural biological composites under a variety of loading configurations.

- Dehydration of nacre by exposing to vacuum in the SEM chamber was found to be minimum within the time frame used in all the in situ mechanical experiments, indicating the applicability of this mechanical testing technique on hydrated biological samples.

- Nacre was found to exhibit a weakened interface between mineral tablets with increasing loading rates. Two potential mechanisms relating to entangled long molecules along the organic interfaces and electrostatic attractions between the mineral tablets are proposed to explain this interfacial weakening behaviour.

- Among the three biological composites (nacre, arthropod exoskeleton and antler bone) studied in this thesis, the biological interface with more confinement (smaller w/τ_A value) displayed less shear strength sensitivity to varying loading rates but appeared to adapt to more dynamic physiological loading conditions.

- The mechanical properties of a graded tendon-to-bone attachment region was directly related to compositional variations, resulting in a predictive model.

References

1. Hull D, Clyne T. An introduction to composite materials: Cambridge university press; 1996.
2. Liu L, Barber AH, Nuriel S, Wagner HD. Mechanical Properties of Functionalized Single‐Walled Carbon‐Nanotube/Poly (vinyl alcohol) Nanocomposites. Advanced Functional Materials. 2005;15(6):975-80.
3. Tang Z, Kotov NA, Magonov S, Ozturk B. Nanostructured artificial nacre. Nature Materials. 2003;2(6):413-8.
4. Podsiadlo P, Kaushik AK, Arruda EM, Waas AM, Shim BS, Xu J, et al. Ultrastrong and Stiff Layered Polymer Nanocomposites. Science. 2007;318(5847):80-3.
5. Bonderer LJ, Studart AR, Gauckler LJ. Bioinspired Design and Assembly of Platelet Reinforced Polymer Films. Science. 2008;319(5866):1069-73.
6. Currey JD, Landete-Castillejos T, Estevez J, Ceacero F, Olguin A, Garcia A, et al. The mechanical properties of red deer antler bone when used in fighting. The Journal of experimental biology. 2009;212(24):3985-93.
7. Currey J. Strain rate dependence of the mechanical properties of reindeer antler and the cumulative damage model of bone fracture. Journal of biomechanics. 1989;22(5):469-75.
8. Patek S, Korff W, Caldwell R. Biomechanics: deadly strike mechanism of a mantis shrimp. Nature. 2004;428(6985):819-20.
9. Chen P, Lin A, Lin Y, Seki Y, Stokes A, Peyras J, et al. Structure and mechanical properties of selected biological materials. Journal of the Mechanical Behavior of Biomedical Materials. 2008;1(3):208-26.
10. Meyers MA, Lin AY, Seki Y, Chen P-Y, Kad BK, Bodde S. Structural biological composites: an overview. Jom. 2006;58(7):35-41.
11. Chan YL, Ngan AHW, King NM. Use of focused ion beam milling for investigating the mechanical properties of biological tissues: A study of human primary molars. Journal of the Mechanical Behavior of Biomedical Materials. 2009;2(4):375-83.
12. Bruet B, Qi H, Boyce M, Panas R, Tai K, Frick L, et al. Nanoscale morphology and indentation of individual nacre tablets from the gastropod mollusc Trochus niloticus. Journal of Materials Research. 2005;20(09):2400-19.
13. Smith BL, Schäffer TE, Viani M, Thompson JB, Frederick NA, Kindt J, et al. Molecular mechanistic origin of the toughness of natural adhesives, fibres and composites. Nature. 1999;399(6738):761-3.
14. Dunlop JWC, Fratzl P. Biological Composites. Annual Review of Materials Research. 2010;40(1):1-24.

15. Ashby MF, Gibson LJ, Wegst U, Olive R. The Mechanical Properties of Natural Materials. I. Material Property Charts. Proceedings of the Royal Society A: Mathematical, Physical and Engineering Sciences. 1995;450(1938):123-40.
16. Wegst U, Ashby M. The mechanical efficiency of natural materials. Philosophical Magazine. 2004;84(21):2167-86.
17. Chen P-Y, Lin A-M, Stokes A, Seki Y, Bodde S, McKittrick J, et al. Structural biological materials: overview of current research. Jom. 2008;60(6):23-32.
18. Ji B, Gao H. Mechanical properties of nanostructure of biological materials. Journal of the Mechanics and Physics of Solids. 2004;52(9):1963-90.
19. Gao H, Ji B, Jager IL, Arzt E, Fratzl P. Materials become insensitive to flaws at nanoscale: Lessons from nature. Proceedings of the National Academy of Sciences. 2003;100(10):5597-600.
20. Meyers MA, Chen P-Y, Lin AY-M, Seki Y. Biological materials: Structure and mechanical properties. Progress in Materials Science. 2008;53(1):1-206.
21. Van der Laag N, Van Dijk A, Dortmans L. Fracture toughness of calcium hydroxyapatite and spinel at different humidities and loading rates. Key Engineering Materials. 2001;206:1599-602.
22. Weiner S, Addadi L. At the cutting edge. Science. 2002;298(5592):375-6.
23. Lowenstam HA, Weiner S. On biomineralization: Oxford University Press New York; 1989.
24. Weissbuch I, Addadi L, Leiserowitz L. Molecular recognition at crystal interfaces. Science. 1991;253(5020):637-45.
25. Mann S. Biomineralization: principles and concepts in bioinorganic materials chemistry: Oxford University Press; 2001.
26. Mann S, Archibald DD, Didymus JM, Douglas T, Heywood BR, Meldrum FC, et al. Crystallization at inorganic-organic interfaces: biominerals and biomimetic synthesis. Science. 1993;261(5126):1286-92.
27. Addadi L, Weiner S. Interactions between acidic proteins and crystals: stereochemical requirements in biomineralization. Proceedings of the National Academy of Sciences. 1985;82(12):4110-4.
28. Addadi L, Moradian J, Shay E, Maroudas N, Weiner S. A chemical model for the cooperation of sulfates and carboxylates in calcite crystal nucleation: relevance to biomineralization. Proceedings of the National Academy of Sciences. 1987;84(9):2732-6.
29. Addadi L, Raz S, Weiner S. Taking advantage of disorder: amorphous calcium carbonate and its roles in biomineralization. Advanced Materials. 2003;15(12):959-70.
30. Nelson DL, Lehninger AL, Cox MM. Lehninger principles of biochemistry: Macmillan; 2008.
31. Lodish H, Zipursky SL. Molecular cell biology. Biochemistry and Molecular Biology Education. 2001;29:126-33.
32. Vander A, Sherman J, Luciano D. Human physiology 8th edition. McGraw Hill.
33. Launey ME, Buehler MJ, Ritchie RO. On the mechanistic origins of toughness in bone. Annual Review of Materials Research. 2010;40:25-53.
34. Bechtle S, Ang SF, Schneider GA. On the mechanical properties of hierarchically structured biological materials. Biomaterials. 2010;31(25):6378-85.

35. Mayer G. Rigid biological systems as models for synthetic composites. Science. 2005;310(5751):1144-7.
36. Barthelat F, Li C-M, Comi C, Espinosa HD. Mechanical properties of nacre constituents and their impact on mechanical performance. Journal of Materials Research. 2011;21(08):1977-86.
37. Bäuerlein E, Behrens P, Epple M. Handbook of biomineralization: Wiley-VCH; 2007.
38. Boyle A. The structure and development of mammalian enamel; 1964.
39. Miserez A, Weaver JC, Thurner PJ, Aizenberg J, Dauphin Y, Fratzl P, et al. Effects of laminate architecture on fracture resistance of sponge biosilica: lessons from nature. Advanced Functional Materials. 2008;18(8):1241-8.
40. Mayer G, Sarikaya M. Rigid biological composite materials: structural examples for biomimetic design. Experimental Mechanics. 2002;42(4):395-403.
41. Woesz A, Weaver JC, Kazanci M, Dauphin Y, Aizenberg J, Morse DE, et al. Micromechanical properties of biological silica in skeletons of deep-sea sponges. Journal of Materials Research. 2006;21(08):2068-78.
42. Aizenberg J, Sundar VC, Yablon AD, Weaver JC, Chen G. Biological glass fibers: correlation between optical and structural properties. Proceedings of the National Academy of Sciences of the United States of America. 2004;101(10):3358-63.
43. Pashley DH, Ciucchi B, Sano H, Horner JA. Permeability of dentin to adhesive agents. Quintessence international (Berlin, Germany: 1985). 1993;24(9):618-31.
44. Menig R, Meyers M, Meyers M, Vecchio K. Quasi-static and dynamic mechanical response of Strombus gigas (conch) shells. Materials Science and Engineering: A. 2001;297(1):203-11.
45. Kamat S, Kessler H, Ballarini R, Nassirou M, Heuer AH. Fracture mechanisms of the Strombus gigas conch shell: II-micromechanics analyses of multiple cracking and large-scale crack bridging. Acta Materialia. 2004;52(8):2395-406.
46. Chen P-Y, Stokes A, McKittrick J. Comparison of the structure and mechanical properties of bovine femur bone and antler of the North American elk (Cervus elaphus canadensis). Acta biomaterialia. 2009;5(2):693-706.
47. Launey ME, Chen P-Y, McKittrick J, Ritchie RO. Mechanistic aspects of the fracture toughness of elk antler bone. Acta biomaterialia. 2010;6(4):1505-14.
48. Villarreal JE. Mapping of elastic modulus and hardness in Trochus niloticus seashell nacre by nanoindentation: Massachusetts Institute of Technology; 2006.
49. Sun J-y, Tong J. Fracture toughness properties of three different biomaterials measured by nanoindentation. Journal of Bionic Engineering. 2007;4(1):11-7.
50. Ang SF, Bortel EL, Swain MV, Klocke A, Schneider GA. Size-dependent elastic/inelastic behavior of enamel over millimeter and nanometer length scales. Biomaterials. 2010;31(7):1955-63.
51. He LH, Swain MV. Understanding the mechanical behaviour of human enamel from its structural and compositional characteristics. Journal of the Mechanical Behavior of Biomedical Materials. 2008;1(1):18-29.
52. Marshall SJ, Balooch M, Habelitz S, Balooch G, Gallagher R, Marshall GW. The dentin–enamel junction—a natural, multilevel interface. Journal of the European Ceramic Society. 2003;23(15):2897-904.
53. Kamat S, Su X, Ballarini R, Heuer A. Structural basis for the fracture toughness of the shell of the conch Strombus gigas. Nature. 2000;405(6790):1036-40.

54. Kinney J, Balooch M, Marshall S, Marshall G, Weihs T. Hardness and Young's modulus of human peritubular and intertubular dentine. Archives of Oral Biology. 1996;41(1):9-13.
55. Imbeni V, Kruzic J, Marshall G, Marshall S, Ritchie R. The dentin–enamel junction and the fracture of human teeth. Nature Materials. 2005;4(3):229-32.
56. Lai LYZJW. The structure and micromechanical properties of mollusk shell. Chinese Journal of Materials Research. 2007;5:022.
57. Laraia VJ, Heuer AH. Novel composite microstructure and mechanical behavior of mollusk shell. Journal of the American Ceramic Society. 1989;72(11):2177-9.
58. Rho J-Y, Tsui TY, Pharr GM. Elastic properties of human cortical and trabecular lamellar bone measured by nanoindentation. Biomaterials. 1997;18(20):1325-30.
59. Hoffler C, Moore K, Kozloff K, Zysset P, Brown M, Goldstein S. Heterogeneity of bone lamellar-level elastic moduli. Bone. 2000;26(6):603-9.
60. Mullins L, Bruzzi M, McHugh P. Measurement of the microstructural fracture toughness of cortical bone using indentation fracture. Journal of biomechanics. 2007;40(14):3285-8.
61. Evans G, Behiri J, Currey J, Bonfield W. Microhardness and Young's modulus in cortical bone exhibiting a wide range of mineral volume fractions, and in a bone analogue. Journal of Materials Science: Materials in Medicine. 1990;1(1):38-43.
62. Gao H. Application of fracture mechanics concepts to hierarchical biomechanics of bone and bone-like materials. International Journal of Fracture. 2006;138(1-4):101-37.
63. Gao H, Ji B. Modeling fracture in nanomaterials via a virtual internal bond method. Engineering Fracture Mechanics. 2003;70(14):1777-91.
64. Gao H, Ji B, Buehler MJ, Yao H. Flaw tolerant bulk and surface nanostructures of biological systems. Mech Chem Biosyst. 2004;1(1):37-52.
65. Vaia RA, Giannelis EP. Polymer nanocomposites: status and opportunities. MRS bulletin. 2001;26(05):394-401.
66. Scherge M, Gorb S, Gorb SN. Biological micro-and nanotribology: Springer Science & Business Media; 2001.
67. Sikes C, Wheeler A, Wierzbicki A, Dillaman R, De Luca L. Oyster shell protein and atomic force microscopy of oyster shell folia. The Biological Bulletin. 1998;194(3):304-16.
68. Wallwork ML, Kirkham J, Zhang J, Smith DA, Brookes SJ, Shore RC, et al. Binding of matrix proteins to developing enamel crystals: an atomic force microscopy study. Langmuir. 2001;17(8):2508-13.
69. Wierzbicki A, Sikes C, Madura J, Drake B. Atomic force microscopy and molecular modeling of protein and peptide binding to calcite. Calcified tissue international. 1994;54(2):133-41.
70. Jäger I, Fratzl P. Mineralized collagen fibrils: a mechanical model with a staggered arrangement of mineral particles. Biophysical journal. 2000;79(4):1737-46.
71. Gao H, Klein P. Numerical simulation of crack growth in an isotropic solid with randomized internal cohesive bonds. Journal of the Mechanics and Physics of Solids. 1998;46(2):187-218.

72. Orowan E. Energy criteria of fracture: DTIC Document; 1954 Contract No.: Document Number|.
73. Meyers MA, Lin AY-M, Chen P-Y, Muyco J. Mechanical strength of abalone nacre: Role of the soft organic layer. Journal of the Mechanical Behavior of Biomedical Materials. 2008;1(1):76-85.
74. Li X, Chang W-C, Chao YJ, Wang R, Chang M. Nanoscale structural and mechanical characterization of a natural nanocomposite material: the shell of red abalone. Nano letters. 2004;4(4):613-7.
75. Barthelat F, Tang H, Zavattieri P, Li C-M, Espinosa H. On the mechanics of mother-of-pearl: a key feature in the material hierarchical structure. Journal of the Mechanics and Physics of Solids. 2007;55(2):306-37.
76. Wang R, Suo Z, Evans A, Yao N, Aksay I. Deformation mechanisms in nacre. J Mater Res. 2001;16(9):2485-93.
77. Menig R, Meyers M, Meyers M, Vecchio K. Quasi-static and dynamic mechanical response of< i> Haliotis rufescens</i>(abalone) shells. Acta Materialia. 2000;48(9):2383-98.
78. Barthelat F, Espinosa H. An experimental investigation of deformation and fracture of nacre–mother of pearl. Experimental Mechanics. 2007;47(3):311-24.
79. Sarikaya M, Gunnison K, Yasrebi M, Aksay I, editors. Mechanical property-microstructural relationships in abalone shell. MRS Proceedings; 1989: Cambridge Univ Press.
80. Weiner S, Addadi L. Design strategies in mineralized biological materials. J Mater Chem. 1997;7(5):689-702.
81. Sun J, Bhushan B. Hierarchical structure and mechanical properties of nacre: a review. RSC Advances. 2012;2(20):7617.
82. Barthelat F. Nacre from mollusk shells: a model for high-performance structural materials. Bioinspiration & Biomimetics. 2010;5(3):035001.
83. Lin A, Meyers MA. Growth and structure in abalone shell. Materials Science and Engineering: A. 2005;390(1):27-41.
84. Cartwright JH, Checa AG. The dynamics of nacre self-assembly. Journal of The Royal Society Interface. 2007;4(14):491-504.
85. Jackson AP, Vincent JFV, Turner RM. The Mechanical Design of Nacre. Proceedings of the Royal Society B: Biological Sciences. 1988;234(1277):415-40.
86. Song F, Zhang X, Bai Y. Microstructure and characteristics in the organic matrix layers of nacre. Journal of Materials Research. 2002;17(07):1567-70.
87. Schäffer TE, Ionescu-Zanetti C, Proksch R, Fritz M, Walters DA, Almqvist N, et al. Does abalone nacre form by heteroepitaxial nucleation or by growth through mineral bridges? Chemistry of Materials. 1997;9(8):1731-40.
88. Song F, Bai Y. Effects of nanostructures on the fracture strength of the interfaces in nacre. Journal of Materials Research. 2003;18(08):1741-4.
89. Currey JD. Mechanical Properties of Mother of Pearl in Tension. Proceedings of the Royal Society B: Biological Sciences. 1977;196(1125):443-63.
90. Sarikaya M. An introduction to biomimetics: a structural viewpoint. Microscopy research and technique. 1994;27(5):360-75.
91. Meyers M, Chawla K. Mechanical Behavior of Materials, 1999. Prentice-Hall, Upper Saddle River.

92. Barthelat F, Tang H, Zavattieri P, Li C, Espinosa H. On the mechanics of mother-of-pearl: A key feature in the material hierarchical structure. Journal of the Mechanics and Physics of Solids. 2007;55(2):306-37.
93. Lin AY-M, Meyers MA. Interfacial shear strength in abalone nacre. Journal of the Mechanical Behavior of Biomedical Materials. 2009;2(6):607-12.
94. Barthelat F, Zhu D. A novel biomimetic material duplicating the structure and mechanics of natural nacre. Journal of Materials Research. 2011;26(10):1203-15.
95. Vincent J. Structural biomaterials: Princeton University Press; 2012.
96. Neville AC. Biology of the arthropod cuticle. 1975.
97. Vincent JF. Arthropod cuticle: a natural composite shell system. Composites Part A: Applied Science and Manufacturing. 2002;33(10):1311-5.
98. Vincent JF, Wegst UG. Design and mechanical properties of insect cuticle. Arthropod Structure & Development. 2004;33(3):187-99.
99. Joffe I, Hepburn H, Nelson K, Green N. Mechanical properties of a crustacean exoskeleton. Comparative Biochemistry and Physiology Part A: Physiology. 1975;50(3):545-9.
100. Bouligand Y. Twisted fibrous arrangements in biological materials and cholesteric mesophases. Tissue and Cell. 1972;4(2):189-217.
101. Giraud-Guille M-M. Fine structure of the chitin-protein system in the crab cuticle. Tissue and Cell. 1984;16(1):75-92.
102. Giraud-Guille M-M, Chanzy H, Vuong R. Chitin crystals in arthropod cuticles revealed by diffraction contrast transmission electron microscopy. Journal of structural biology. 1990;103(3):232-40.
103. Giraud-Guille M-M. Plywood structures in nature. Current Opinion in Solid State and Materials Science. 1998;3(3):221-7.
104. Lowenstam HA. Minerals formed by organisms. Science. 1981;211(4487):1126-31.
105. Giraud-Guille M, Bouligand Y. Crystal growth in a chitin matrix: the study of calcite development in the crab cuticle. Chitin World, Wirtschaftsverlag NW Bremerhaven. 1995:136-44.
106. Chen P-Y, Lin AY-M, McKittrick J, Meyers MA. Structure and mechanical properties of crab exoskeletons. Acta biomaterialia. 2008;4(3):587-96.
107. Hepburn H, Joffe I, Green N, Nelson K. Mechanical properties of a crab shell. Comparative Biochemistry and Physiology Part A: Physiology. 1975;50(3):551-IN13.
108. Joffe I, Hepburn H, Andersen S. On the mechanical properties ofLimulus solid cuticle. Journal of comparative physiology. 1975;101(2):147-60.
109. Raabe D, Al-Sawalmih A, Romano P, Sachs C, Brokmeier HG, Yi SB, et al., editors. Structure and crystallographic texture of arthropod bio-composites. Materials Science Forum; 2005: Trans Tech Publ.
110. Raabe D, Romano P, Sachs C, Al-Sawalmih A, Brokmeier H-G, Yi S-B, et al. Discovery of a honeycomb structure in the twisted plywood patterns of fibrous biological nanocomposite tissue. Journal of Crystal Growth. 2005;283(1):1-7.
111. Raabe D, Romano P, Sachs C, Fabritius H, Al-Sawalmih A, Yi S-B, et al. Microstructure and crystallographic texture of the chitin–protein network in the biological composite material of the exoskeleton of the lobster Homarus americanus. Materials Science and Engineering: A. 2006;421(1):143-53.

112. Raabe D, Sachs C, Romano P. The crustacean exoskeleton as an example of a structurally and mechanically graded biological nanocomposite material. Acta Materialia. 2005;53(15):4281-92.
113. Romano P, Fabritius H, Raabe D. The exoskeleton of the lobster Homarus americanus as an example of a smart anisotropic biological material☆. Acta Biomaterialia. 2007;3(3):301-9.
114. Sachs C, Fabritius H, Raabe D. Hardness and elastic properties of dehydrated cuticle from the lobster Homarus americanus obtained by nanoindentation. Journal of Materials Research. 2006;21(08):1987-95.
115. Melnick C, Chen Z, Mecholsky J. Hardness and toughness of exoskeleton material in the stone crab, Menippe mercenaria. Journal of Materials Research. 1996;11(11):2903-7.
116. Kaplan F, Hayes W, Keaveny T, Boskey A, Einhorn T, Iannotti J. Form and function of bone. Orthopaedic basic science. 1994:127-85.
117. Woo S, An K, Frank C, Livesay G, Ma C, Zeminski J, et al. Anatomy, biology, and biomechanics of tendon and ligament. Orthopaedic basic science. 2000;2:581-616.
118. Thomopoulos S, Kim HM, Rothermich SY, Biederstadt C, Das R, Galatz LM. Decreased muscle loading delays maturation of the tendon enthesis during postnatal development. Journal of Orthopaedic Research. 2007;25(9):1154-63.
119. Jones RM. Mechanics of composite materials: CRC press; 1998.
120. Aoki M, Oguma H, Fukushima S, Ishii S, Ohtani S, Murakami G. Fibrous connection to bone after immediate repair of the canine infraspinatus: the most effective bony surface for tendon attachment. Journal of Shoulder and Elbow Surgery. 2001;10(2):123-8.
121. Fujioka H, Thakur R, Wang G-J, Mizuno K, Balian G, Hurwitz SR. Comparison of surgically attached and non-attached repair of the rat Achilles tendon-bone interface. Cellular organization and type X collagen expression. Connective tissue research. 1998;37(3-4):205-18.
122. Liu SH, Panossian V, Al-Shaikh R, Tomin E, Shepherd E, Finerman GA, et al. Morphology and matrix composition during early tendon to bone healing. Clinical orthopaedics and related research. 1997;339:253-60.
123. St Pierre P, Olson EJ, Elliott JJ, O'Hair KC, McKinney LA, Ryan J. Tendon-healing to cortical bone compared with healing to a cancellous trough. A biomechanical and histological evaluation in goats. The Journal of Bone & Joint Surgery. 1995;77(12):1858-66.
124. Thomopoulos S, Williams G, Soslowsky L. Tendon to bone healing: differences in biomechanical, structural, and compositional properties due to a range of activity levels. Journal of biomechanical engineering. 2003;125(1):106-13.
125. Mirowitz S. Normal rotator cuff: MR imaging with conventional and fat-suppression techniques. Radiology. 1991;180(3):735-40.
126. Harryman Dn, Mack L, Wang K, Jackins S, Richardson M, Matsen Fr. Repairs of the rotator cuff. Correlation of functional results with integrity of the cuff. The Journal of Bone & Joint Surgery. 1991;73(7):982-9.
127. Galatz LM, Ball CM, Teefey SA, Middleton WD, Yamaguchi K. The outcome and repair integrity of completely arthroscopically repaired large and massive rotator cuff tears. The Journal of Bone & Joint Surgery. 2004;86(2):219-24.

128. Fu FH, Bennett CH, Lattermann C, Ma CB. Current trends in anterior cruciate ligament reconstruction part 1: biology and biomechanics of reconstruction. The American journal of sports medicine. 1999;27(6):821-30.
129. Fu FH, Bennett CH, Ma CB, Menetrey J, Lattermann C. Current trends in anterior cruciate ligament reconstruction part II. Operative procedures and clinical correlations. The American journal of sports medicine. 2000;28(1):124-30.
130. Thomopoulos S, Hattersley G, Rosen V, Mertens M, Galatz L, Williams G, et al. The localized expression of extracellular matrix components in healing tendon insertion sites: an in situ hybridization study. Journal of Orthopaedic Research. 2002;20(3):454-63.
131. Galatz LM, Sandell LJ, Rothermich SY, Das R, Mastny A, Havlioglu N, et al. Characteristics of the rat supraspinatus tendon during tendon‐to‐bone healing after acute injury. Journal of Orthopaedic Research. 2006;24(3):541-50.
132. Wong MWN, Qin L, Lee KM, Leung KS. Articular cartilage increases transition zone regeneration in bone-tendon junction healing. Clinical orthopaedics and related research. 2009;467(4):1092-100.
133. Wong M, Tai K, Lee K, Qin L, Leung K, editors. Bone formation and fibrocartilage regeneration at bone tendon junction with allogeneic cultured chondrocyte pellet interposition. Journal of Bone and Mineral Research; 2007: AMER SOC BONE & MINERAL RES 2025 M ST, NW, STE 800, WASHINGTON, DC 20036-3309 USA.
134. Rodeo SA, Arnoczky SP, Torzilli PA, Hidaka C, Warren RF. Tendon-healing in a bone tunnel. A biomechanical and histological study in the dog. The Journal of Bone & Joint Surgery. 1993;75(12):1795-803.
135. Benjamin M, Kumai T, Milz S, Boszczyk B, Boszczyk A, Ralphs J. The skeletal attachment of tendons—tendon 'entheses'. Comparative Biochemistry and Physiology Part A: Molecular & Integrative Physiology. 2002;133(4):931-45.
136. Benjamin M, Toumi H, Ralphs J, Bydder G, Best T, Milz S. Where tendons and ligaments meet bone: attachment sites ('entheses') in relation to exercise and/or mechanical load. Journal of Anatomy. 2006;208(4):471-90.
137. Waggett AD, Ralphs JR, Kwan AP, Woodnutt D, Benjamin M. Characterization of collagens and proteoglycans at the insertion of the human Achilles tendon. Matrix Biology. 1998;16(8):457-70.
138. Thomopoulos S, Williams GR, Gimbel JA, Favata M, Soslowsky LJ. Variation of biomechanical, structural, and compositional properties along the tendon to bone insertion site. Journal of Orthopaedic Research. 2003;21(3):413-9.
139. Kumagai J, Sarkar K, Uhthoff HK, Okawara Y, Ooshima A. Immunohistochemical distribution of type I, II and III collagens in the rabbit supraspinatus tendon insertion. Journal of Anatomy. 1994;185(Pt 2):279.
140. Fukuta S, Oyama M, Kavalkovich K, Fu FH, Niyibizi C. Identification of types II, IX and X collagens at the insertion site of the bovine achilles tendon. Matrix Biology. 1998;17(1):65-73.
141. Visconti CS, Kavalkovich K, Wu J-J, Niyibizi C. Biochemical analysis of collagens at the ligament–bone interface reveals presence of cartilage-specific collagens. Archives of biochemistry and biophysics. 1996;328(1):135-42.

142. Ralphs J, Benjamin M, Waggett A, Russell D, Messner K, Gao J. Regional differences in cell shape and gap junction expression in rat Achilles tendon: relation to fibrocartilage differentiation. Journal of Anatomy. 1998;193(2):215-22.
143. Wopenka B, Kent A, Pasteris JD, Yoon Y, Thomopoulos S. The tendon-to-bone transition of the rotator cuff: a preliminary Raman spectroscopic study documenting the gradual mineralization across the insertion in rat tissue samples. Applied spectroscopy. 2008;62(12):1285-94.
144. Thomopoulos S, Genin GM, Galatz LM. The development and morphogenesis of the tendon-to-bone insertion What development can teach us about healing. Journal of musculoskeletal & neuronal interactions. 2010;10(1):35.
145. Thomopoulos S, Marquez JP, Weinberger B, Birman V, Genin GM. Collagen fiber orientation at the tendon to bone insertion and its influence on stress concentrations. Journal of biomechanics. 2006;39(10):1842-51.
146. Kostrominova TY, Dow DE, Dennis RG, Miller RA, Faulkner JA. Comparison of gene expression of 2-mo denervated, 2-mo stimulated-denervated, and control rat skeletal muscles. Physiological genomics. 2005;22(2):227-43.
147. Genin GM, Kent A, Birman V, Wopenka B, Pasteris JD, Marquez PJ, et al. Functional grading of mineral and collagen in the attachment of tendon to bone. Biophysical journal. 2009;97(4):976-85.
148. Goodhew PJ, Humphreys J, Beanland R. Electron microscopy and analysis: CRC Press; 2000.
149. Keppel G. Design and analysis: A researcher's handbook: Prentice-Hall, Inc; 1991.
150. Schwoeble A, Dalley A, Henderson B, Casuccio G. Computer-controlled SEM and microimaging of fine particles. Jom. 1988;40(8):11-4.
151. Pawley JB, Norton JT. A chamber attached to the SEM for fracturing and coating frozen biological samples. Journal of microscopy. 1978;112(2):169-82.
152. Flegler SL, Heckman JW, Klomparens KL. Scanning and transmission electron microscopy: an introduction: WH Freeman New York; 1993.
153. LEŠER V, DROBNE D, PIPAN Ž, Milani M, TATTI F. Comparison of different preparation methods of biological samples for FIB milling and SEM investigation. Journal of microscopy. 2009;233(2):309-19.
154. Hang F, Lu D, Bailey RJ, Jimenez-Palomar I, Stachewicz U, Cortes-Ballesteros B, et al. In situtensile testing of nanofibers by combining atomic force microscopy and scanning electron microscopy. Nanotechnology. 2011;22(36):365708.
155. Jimenez-Palomar I, Shipov A, Shahar R, Barber AH. Influence of SEM vacuum on bone micromechanics using in situ AFM. Journal of the Mechanical Behavior of Biomedical Materials. 2012;5(1):149-55.
156. Bogner A, Thollet G, Basset D, Jouneau P-H, Gauthier C. Wet STEM: A new development in environmental SEM for imaging nano-objects included in a liquid phase. Ultramicroscopy. 2005;104(3):290-301.
157. McCarthy J, Pei Z, Becker M, Atteridge D. FIB micromachined submicron thickness cantilevers for the study of thin film properties. Thin Solid Films. 2000;358(1):146-51.
158. Di Maio D, Roberts S. Measuring fracture toughness of coatings using focused-ion-beam-machined microbeams. Journal of Materials Research. 2005;20(02):299-302.

159. Ishitani T, Tsuboi H, Yaguchi T, Koike H. Transmission electron microscope sample preparation using a focused ion beam. Journal of Electron Microscopy. 1994;43(5):322-6.
160. Abrahams M, Buiocchi C. Cross‐sectional specimens for transmission electron microscopy. Journal of Applied Physics. 1974;45(8):3315-6.
161. Seliger R, Ward J, Wang V, Kubena R. A high‐intensity scanning ion probe with submicrometer spot size. Applied Physics Letters. 1979;34(5):310-2.
162. Lu D, Barber AH. Optimized nanoscale composite behaviour in limpet teeth. Journal of The Royal Society Interface. 2011;9(71):1318-24.
163. Giannuzzi L, Stevie F. A review of focused ion beam milling techniques for TEM specimen preparation. Micron. 1999;30(3):197-204.
164. Giannuzzi LA, Stevie FA. Introduction to focused ion beams: instrumentation, theory, techniques and practice: Springer Science & Business Media; 2005.
165. Eaton P, West P. Atomic force microscopy: Oxford Univ. Press; 2010.
166. Bowen WR, Hilal N. Atomic Force Microscopy in Process Engineering: An Introduction to AFM for Improved Processes and Products: Butterworth-Heinemann; 2009.
167. Binnig G, Rohrer H, Gerber C, Weibel E. Surface studies by scanning tunneling microscopy. Physical review letters. 1982;49(1):57.
168. Albrecht TR, Quate C. Atomic resolution imaging of a nonconductor by atomic force microscopy. Journal of Applied Physics. 1987;62(7):2599-602.
169. Butt H-J, Cappella B, Kappl M. Force measurements with the atomic force microscope: Technique, interpretation and applications. Surface science reports. 2005;59(1):1-152.
170. Lennard-Jones J. On the forces between atoms and ions. Proceedings of the Royal Society of London Series A, Containing Papers of a Mathematical and Physical Character. 1925:584-97.
171. Korngold L, Lipari R. Multiple‐myeloma proteins. III. The antigenic relationship of Bence Jones proteins to normal gamma‐globulin and multiple‐myeloma serum proteins. Cancer. 1956;9(2):262-72.
172. Sader JE, Larson I, Mulvaney P, White LR. Method for the calibration of atomic force microscope cantilevers. Review of Scientific Instruments. 1995;66(7):3789-98.
173. Ohler B. Practical advice on the determination of cantilever spring constants. Veeco Instruments Inc. 2007.
174. Hang F, Barber AH. Nano-mechanical properties of individual mineralized collagen fibrils from bone tissue. Journal of The Royal Society Interface. 2010;8(57):500-5.
175. Hang F, Gupta HS, Barber AH. Nanointerfacial strength between non-collagenous protein and collagen fibrils in antler bone. Journal of The Royal Society Interface. 2013;11(92):20130993-.
176. Wang C, Frogley MD, Cinque G, Liu L-Q, Barber AH. Deformation and failure mechanisms in graphene oxide paper using in situ nanomechanical tensile testing. Carbon. 2013;63:471-7.
177. Luz GM, Mano JF. Biomimetic design of materials and biomaterials inspired by the structure of nacre. Philosophical Transactions of the Royal Society of London A: Mathematical, Physical and Engineering Sciences. 2009;367(1893):1587-605.

178. Sumitomo T, Kakisawa H, Owaki Y, Kagawa Y. In situ transmission electron microscopy observation of reversible deformation in nacre organic matrix. Journal of Materials Research. 2008;23(05):1466-71.
179. Verma D, Katti K, Katti D. Photoacoustic FTIR spectroscopic study of undisturbed nacre from red abalone. Spectrochimica Acta Part A: Molecular and Biomolecular Spectroscopy. 2006;64(4):1051-7.
180. Verma D, Katti K, Katti D. Nature of water in nacre: a 2D Fourier transform infrared spectroscopic study. Spectrochimica Acta Part A: Molecular and Biomolecular Spectroscopy. 2007;67(3):784-8.
181. Bailey RJ, Geurts R, Stokes DJ, de Jong F, Barber AH. Evaluating focused ion beam induced damage in soft materials. Micron. 2013;50:51-6.
182. Drobne D, Milani M, Lešer V, Tatti F. Surface damage induced by FIB milling and imaging of biological samples is controllable. Microscopy research and technique. 2007;70(10):895-903.
183. Barthelat F, Rim JE, Espinosa HD. A Review on the Structure and Mechanical Properties of Mollusk Shells–Perspectives on Synthetic Biomimetic Materials. Applied Scanning Probe Methods XIII: Springer; 2009. p. 17-44.
184. Leung HM, Sinha SK. Scratch and indentation tests on seashells. Tribology International. 2009;42(1):40-9.
185. Stempflé P, Brendlé M. Tribological behaviour of nacre—influence of the environment on the elementary wear processes. Tribology International. 2006;39(12):1485-96.
186. Stempflé P, Djilali T, Njiwa RK, Rousseau M, Lopez E, Bourrat X. Thermal-induced wear mechanisms of sheet nacre in dry friction. Tribology letters. 2009;35(2):97-104.
187. Chen G, Krantz S, Ma D, Wayne C, West H. The Euler-Bernoulli beam equation with boundary energy dissipation. Operator methods for optimal control problems. 1987;108:67-96.
188. Wang C. Timoshenko beam-bending solutions in terms of Euler-Bernoulli solutions. Journal of engineering mechanics. 1995;121(6):763-5.
189. Currey JD. The design of mineralised hard tissues for their mechanical functions. Journal of Experimental Biology. 1999;202(23):3285-94.
190. Huang Z, Li H, Pan Z, Wei Q, Chao YJ, Li X. Uncovering high-strain rate protection mechanism in nacre. Scientific reports. 2011;1.
191. Mohanty B, Katti KS, Katti DR, Verma D. Dynamic nanomechanical response of nacre. Journal of Materials Research. 2006;21(08):2045-51.
192. Munch E, Launey ME, Alsem DH, Saiz E, Tomsia AP, Ritchie RO. Tough, bio-inspired hybrid materials. Science. 2008;322(5907):1516-20.
193. Evans A, Suo Z, Wang R, Aksay I, He M, Hutchinson J. Model for the robust mechanical behavior of nacre. J Mater Res. 2001;16(9):2476.
194. Xu Z-H, Li X. Deformation Strengthening of Biopolymer in Nacre. Advanced Functional Materials. 2011;21(20):3883-8.
195. Di Maio D, Roberts SG. Measuring fracture toughness of coatings using focused-ion-beam-machined microbeams. Journal of Materials Research. 2011;20(02):299-302.

196. Reyntjens S, Puers R. A review of focused ion beam applications in microsystem technology. Journal of Micromechanics and Microengineering. 2001;11(4):287.
197. Stokes DJ, Vystavel T, Morrissey F. Focused ion beam (FIB) milling of electrically insulating specimens using simultaneous primary electron and ion beam irradiation. Journal of Physics D: Applied Physics. 2007;40(3):874-7.
198. Koester KJ, Ager JW, Ritchie RO. The true toughness of human cortical bone measured with realistically short cracks. Nature Materials. 2008;7(8):672-7.
199. Dutta A, Tekalur SA, Miklavcic M. Optimal overlap length in staggered architecture composites under dynamic loading conditions. Journal of the Mechanics and Physics of Solids. 2013;61(1):145-60.
200. Clegg W, Kendall K, Alford NM, Button T, Birchall J. A simple way to make tough ceramics. 1990.
201. Compston P, Jar PYB, Burchill PJ, Takahashi K. The effect of matrix toughness and loading rate on the mode-II interlaminar fracture toughness of glass-fibre/vinyl-ester composites. Composites Science and Technology. 2001;61(2):321-33.
202. Currey J. Biomaterials: sacrificial bonds heal bone. Nature. 2001;414(6865):699-.
203. Thompson JB, Kindt JH, Drake B, Hansma HG, Morse DE, Hansma PK. Bone indentation recovery time correlates with bond reforming time. Nature. 2001;414(6865):773-6.
204. Fantner GE, Hassenkam T, Kindt JH, Weaver JC, Birkedal H, Pechenik L, et al. Sacrificial bonds and hidden length dissipate energy as mineralized fibrils separate during bone fracture. Nature Materials. 2005;4(8):612-6.
205. Hartmann MA, Fratzl P. Sacrificial ionic bonds need to be randomly distributed to provide shear deformability. Nano letters. 2009;9(10):3603-7.
206. Roer R, Dillaman R. The structure and calcification of the crustacean cuticle. American Zoologist. 1984;24(4):893-909.
207. Drach P. Mue et cycle d'intermue chez les crustacés décapodes: Institut Océanographique; 1939.
208. Williams M. Stress singularities resulting from various boundary conditions. Journal of Applied Mechanics. 1952;19(4):526-8.
209. Hutchinson JW, Suo Z. Mixed mode cracking in layered materials. Advances in applied mechanics. 1991;29:63-191.
210. Birman V, Byrd LW. Modeling and analysis of functionally graded materials and structures. Applied Mechanics Reviews. 2007;60(5):195-216.
211. Mortensen A, Suresh S. Fundamentals of Functionally Graded Materials: Processing and Thermomechanical Behaviour of Graded Metals and Metal-ceramic Composites [M]. London: IOM Communications Ltd. 1998:1-70.
212. Tersoff J, LeGoues F. Competing relaxation mechanisms in strained layers. Physical review letters. 1994;72(22):3570.
213. Stouffer D, Butler D, Hosny D. The relationship between crimp pattern and mechanical response of human patellar tendon-bone units. Journal of biomechanical engineering. 1985;107(2):158-65.
214. Cotton R, Rideout D. Tears of the humeral rotator cuff. J Bone Joint Surg Br. 1964;46:314-28.

215. Moffat KL, Sun W-HS, Pena PE, Chahine NO, Doty SB, Ateshian GA, et al. Characterization of the structure–function relationship at the ligament-to-bone interface. Proceedings of the National Academy of Sciences. 2008;105(23):7947-52.
216. Villegas DF, Maes JA, Magee SD, Donahue TLH. Failure properties and strain distribution analysis of meniscal attachments. Journal of biomechanics. 2007;40(12):2655-62.
217. Genin GM, Birman V. Micromechanics and structural response of functionally graded, particulate-matrix, fiber-reinforced composites. International journal of solids and structures. 2009;46(10):2136-50.
218. Liu YX, Thomopoulos S, Birman V, Li JS, Genin GM. Bi-material attachment through a compliant interfacial system at the tendon-to-bone insertion site. Mech Mater. 2012;44(10):005.
219. Claudepierre P, Voisin M-C. The entheses: histology, pathology, and pathophysiology. Joint Bone Spine. 2005;72(1):32-7.
220. Doschak M, Zernicke R. Structure, function and adaptation of bone-tendon and bone-ligament complexes. J Musculoskelet Neuronal Interact. 2005;5(1):35-40.
221. Benjamin M, McGonagle D. The anatomical basis for disease localisation in seronegative spondyloarthropathy at entheses and related sites. Journal of Anatomy. 2001;199(5):503-26.
222. Benjamin M, Ralphs J. Fibrocartilage in tendons and ligaments—an adaptation to compressive load. Journal of Anatomy. 1998;193(04):481-94.
223. COOPER RR, MISOL S, Stimmel P. Tendon and ligament insertion. The Journal of Bone & Joint Surgery. 1970;52(1):1-170.
224. Liu Y, Birman V, Chen C, Thomopoulos S, Genin GM. Mechanisms of Bimaterial Attachment at the Interface of Tendon to Bone. J Eng Mater Technol. 2011;133(1):011006.
225. Liu SH, Baker CL. Arthroscopically assisted rotator cuff repair: correlation of functional results with integrity of the cuff. Arthroscopy: The Journal of Arthroscopic & Related Surgery. 1994;10(1):54-60.
226. Schwartz AG, Lipner JH, Pasteris JD, Genin GM, Thomopoulos S. Muscle loading is necessary for the formation of a functional tendon enthesis. Bone. 2013;55(1):44-51.
227. Schwartz AG, Pasteris JD, Genin GM, Daulton TL, Thomopoulos S. Mineral distributions at the developing tendon enthesis. PLoS One. 2012;7(11):9.
228. Blitz E, Viukov S, Sharir A, Shwartz Y, Galloway JL, Pryce BA, et al. Bone ridge patterning during musculoskeletal assembly is mediated through SCX regulation of Bmp4 at the tendon-skeleton junction. Developmental cell. 2009;17(6):861-73. PMCID: Pmc3164485.
229. Long F, Zhang XM, Karp S, Yang Y, McMahon AP. Genetic manipulation of hedgehog signaling in the endochondral skeleton reveals a direct role in the regulation of chondrocyte proliferation. Development (Cambridge, England). 2001;128(24):5099-108.
230. Schwartz AG, Long F, Thomopoulos S. Enthesis fibrocartilage cells originate from a population of Hedgehog-responsive cells modulated by the loading environment. Development. 2015;142(1):196-206.

Appendix - Bending Model of the Tendon-to-Bone Attachment

In order to account for the variability in the composition of the beams, it was necessary to develop a model that would describe the average modulus of a beam with varying amounts of mineralized, graded and unmineralized tissue.

A force F is applied to the beam of length L and cross-sectional area A at an angle θ. The axis x lies along the length of the beam with a value of 0 at the free end. The vertical and horizontal components of the force are:

$$F_V = Fsin(\theta) \qquad \text{Equation A1}$$

$$F_H = Fcos(\theta) \qquad \text{Equation A2}$$

This force will cause a displacement v_1 in the horizontal direction and v_2 in the vertical direction. The total displacement, Δ, is equal to:

$$\Delta = \sqrt{v_1 + v_2} \qquad \text{Equation A3}$$

The beam is composed of three sections: mineralized, graded, and unmineralized with lengths of a, b, and c where $a + b + c = L$. Their moduli are E_M, E_G, and E_U respectively. The value of E_G is a linear interpolation between the mineralized and unmineralized moduli:

$$E_G = E_U + \frac{E_M - E_U}{b}(x - c) \qquad \text{Equation A4}$$

The displacement in the horizontal direction v_1, is the sum of the displacements in the unmineralized, v_U, graded, v_G, and mineralized, v_M, sections of the beam:

$$v_1 = v_U + v_G + v_M \qquad \text{Equation A5}$$

The displacements in the unmineralized and mineralized sections can be calculated from basic mechanics:

$$v_U = \frac{F_H}{A}\frac{c}{E_u} = \frac{\sigma c}{E_U} \qquad \text{Equation A6}$$

$$v_M = \frac{\sigma a}{E_M} \qquad \text{Equation A7}$$

The displacement in the graded region can be found from the following:

$$v_G = \int_c^{b+c} \sigma / (E_U + \frac{E_M - E_U}{b}(x - c))\, dx \qquad \text{Equation A8}$$

$$v_G = \frac{\sigma b}{E_M - E_U}(ln\, E_M - \ln E_U) \qquad \text{Equation A9}$$

With all three displacements the horizontal displacement can be found from Equation A5.

$$v_1 = \frac{\sigma c}{E_U} + \frac{\sigma b}{E_M - E_U}(ln\, E_M - \ln E_U) + \frac{\sigma a}{E_M} \qquad \text{Equation A10}$$

$$v_1 = \frac{F cos(\theta)}{A}[\frac{c}{E_U} + \frac{a}{E_M} + \frac{b}{E_M - E_U}(\ln E_M - \ln E_U)] \qquad \text{Equation A11}$$

In order to calculate the vertical displacement of the beam, we need to solve the boundary conditions between the three regions of the beam. As the beam bends, the vertical displacement varies along the length of the beam. Let us define the displacement within the unmineralized region as y_1, displacement in the graded region as y_2, and displacement in the mineralized region as y_3. The total vertical displacement of the beam will be the displacement at the free end of the beam where $x = 0$:

$$v_2 = y_1(x = 0) \qquad \text{Equation A12}$$

In order to find y_1 at x = 0 it is necessary to solve for the following boundary and continuity conditions:

$$y_1(x = c) = y_2(x = c) \qquad \text{Equation A13}$$

$$y_1'(x = c) = y_2'(x = c) \qquad \text{Equation A14}$$

$$y_2(x = b + c) = y_3(x = b + c) \qquad \text{Equation A15}$$

$$y_2'(x = b + c) = y_3'(b + c) \qquad \text{Equation A16}$$

$$y_3(x = L) = 0 \qquad \text{Equation A17}$$

$$y_3'(x = L) = 0 \qquad \text{Equation A18}$$

We can start to solve for these conditions by finding the values of y. For the unmineralized and mineralized sections:

$$E_U I y_1'' = F_V x \qquad \text{Equation A19}$$

$$y_1 = \frac{F_V x^3}{6E_U I} + k_1 x + k_2 \qquad \text{Equation A20}$$

$$y_3 = \frac{F_V x^3}{6E_M I} + k_5 x + k_6 \qquad \text{Equation A21}$$

For the graded tissue:

$$\left[E_U + \frac{E_M - E_U}{b}(x - c)\right] I\, y_2'' = F_V x \qquad \text{Equation A22}$$

$$y_2'' = \frac{F_v}{IE_U} \frac{xdx}{\left(\frac{E_M}{E_U} - 1\right)\left(\frac{x}{b}\right) + \left[1 - \frac{\frac{E_M}{E_U} - 1}{B} c\right]} \qquad \text{Equation A23}$$

Let $p = \frac{\left(\frac{E_M}{E_U} - 1\right)}{B}$ and $t = 1 - \frac{\frac{E_M}{E_U} - 1}{B} c$ such that:

$$y_2'' = \frac{F_v}{IE_U} \int \frac{xdx}{px + t} \qquad \text{Equation A24}$$

$$y_2' = \frac{F_V}{E_U I}\left(\frac{1}{p^2}\right)[px + t - tln(px + t)] + k_3 \qquad \text{Equation A25}$$

$$y_2 = \frac{F_V}{E_U I}\left(\frac{1}{p^2}\right)\left[\frac{px^2}{2} + tx - \frac{t}{p}\ln(px+t)\right] + k_3 x + k_4 \mathrm{S} \qquad \text{Equation A26}$$

The vertical displacement can be calculated by solving for k_2:

$$v_2 = y_1(x=0) = k_2 \qquad \text{Equation A27}$$

The total displacement can then be calculated by inserting Equation A27 and Equation A11 into Equation A3.

In order to calculate the average modulus of the beam, E, we assume the beam is homogenous. In this case the total horizontal and vertical displacements can be described by:

$$v_1 = \frac{Fcos(\theta)L}{EA} \qquad \text{Equation A28}$$

$$v_2 = \frac{Fsin(\theta)L^3}{3EI} \qquad \text{Equation A29}$$

The total displacement is therefore:

$$\Delta = \sqrt{\frac{F^2\cos^2\theta L^2}{E^2A^2} + \frac{F^2\sin^2\theta L^6}{9E^2I^2}} \qquad \text{Equation A30}$$

Solving for the average modulus:

$$E = \frac{FL}{\Delta}\sqrt{\frac{\cos^2\theta}{A^2} + \frac{\sin^2\theta L^4}{I^2}} \qquad \text{Equation A31}$$

By inputting equation the total displacement calculated in Equation A1 - A27 into Equation A31 we can determine the average modulus of each beam.